Technische Universität München
Physik Department T70

Three topics in primordial scalar fluctuations during inflation

Yi Zhu

Vollständiger Abdruck der von der Fakultät für **Physik** der Technischen Universität München zur Erlangung des akademischen Grades eines

Doktors der Naturwissenschaften (Dr. rer. nat.)

genehmigten Dissertation.

Vorsitzender:	Univ.-Prof. Dr. L. Oberauer
Prüfer der Dissertation:	
	1. Univ.-Prof. Dr. B. Garbrecht
	2. Hon.-Prof. E. Komatsu, Ph.D Ludwig-Maximilians-Universität München

Die Dissertation wurde am 26.01.2015 bei der Technischen Universität München eingereicht und durch die Fakultät für **Physik** am 20.02.2015 angenommen.

Abstract:
Within the past three decades, inflation—an expansion phase prior to the hot big bang—has become an important part of standard cosmology. Scalar fluctuations that exit the horizon during inflation and re-enter at later times may seed the formation of galaxies and clusters and generate anisotropies of the cosmic microwave background (CMB) that have been observed experimentally. In this thesis, we discuss three topics on scalar fluctuations during inflation: In the first part, we evaluate the level of non-Gaussianity and the power spectrum of curvature perturbations for hybrid inflation models with a mild waterfall phase. We perform a combined analysis of the original and supersymmetric F-term and D-term models parametrized by a unified potential. We find that for models with a mild waterfall phase that last more than 60 e-folds, the level of non-Gaussianity and the power spectrum amplitude cannot simultaneously satisfy the constraints from CMB angular observations, due to the dominant contribution from entropic modes. In the second part, we analyze inflation models and curvaton scenarios in the light of future measurements of the CMB spectrum distortions, which are generated by energy injection from acoustic waves in the primeval plasma. We show that only very few models can induce CMB distortions at a level that is detectable by the PIXIE experiment. For a PRISM-class experiment, there are more models can be detected. Finally, we investigate quantum fluctuations of a light scalar field in the late-time limit on de Sitter background. To the leading infrared order, we show the equivalence between stochastic and field theoretic approaches. Moreover, the infrared divergence of a massless scalar field is proved to be regulated by its self-interaction.

The bulk of this manuscript is based on the articles which were written during this PhD thesis, a list of which is shown below:

- ⋆ Björn Garbrecht, Florian Gautier, Gerasimos Rigopoulos and Yi Zhu, "Feynman Diagrams for Stochastic Inflation and Quantum Field Theory in de Sitter Space", arXiv:1412.4893[hep-th].

- ⋆ Sébastien Clesse, Björn Garbrecht, and Yi Zhu, "Testing Inflation and Curvaton Scenarios with CMB Distortions", JCAP **10**, 046 (2014) [arXiv:1402.2257[astro-ph.CO]].

- ⋆ Björn Garbrecht, Gerasimos Rigopoulos, and Yi Zhu, "Infrared Correlations in de Sitter Space: Field Theoretic vs. Stochastic Approach", Phys. Rev. D **89**, 063506 (2014) [arXiv:1310.0367[hep-th]].

- ⋆ Sébastien Clesse, Björn Garbrecht, and Yi Zhu, "Non-Gaussianities and Curvature Perturbations from Hybrid Inflation", Phys. Rev. D **89**, 063519 (2014) [arXiv:1304.7042[astro-ph.CO]].

Contents

Chapter 1

General introduction

The big bang cosmology [1, 2] has achieved great success by predicting the existence of the cosmic microwave background (CMB) radiation, which was first detected in 1964 [3]. It also illustrates the evolution of all components of cosmic fluid. However, the pure big bang theory has three important problems concerning the naturalness of the universe: the flatness problem, the horizon problem, and the primordial monopole problem. In 1981, A. Guth [4] suggested that these problems could be resolved by introducing an accelerated expansion phase before the hot big bang, which is so called cosmic inflation [5, 6, 7, 8]. In Guth's model, inflation is driven by a scalar field which is suffering a delayed first order transition from a false vacuum to the true vacuum. During the phase transition, the latent heat concentrates in the wall of true vacuum bubbles. Radiation is generated in collisions of bubble walls. Unfortunately, the bubble wall collisions rarely occur due to the exponential expansion of false vacuum background [9, 10]. Hence, this model cannot reheat enough. To avoid the reheating problem, the new inflation (or slow-roll inflation) scenario is proposed [11, 12]. In the slow-roll inflation scenario, inflation is driven by a scalar field which is rolling down a potential hill very slowly. When the scalar field rolls down fast, inflation ends and reheating will occur. It was soon realized that the inflation mechanism can be also used to explain the origin of perturbations in the universe [13, 14, 15, 16, 17, 18]. During inflation, scalar and tensor fluctuations are frozen out at super-horizon scale while all other perturbations are diluted. When these super-horizon scalar and tensor fluctuations re-enter the horizon in the later radiation- dominated or matter-dominated era, they seed the formation of galaxies and clusters and generate anisotropies of the CMB, which have been observed by many experiments [19, 20, 21].

In section 1.1, we briefly review the three problems in pure big bang cosmology, and how inflation can resolve them. Then, the slow-roll inflation scenario and the concomitant primordial scalar fluctuations will be described in section 1.2. In addition, we introduce a more generic method for calculating primordial fluctuations beyond slow-roll approximation, *i.e.* the δN formalism, in section 1.3. The details for present issues can be found in many standard textbooks for cosmology (*e.g.* [22, 23, 24, 25, 26]) and some review papers (e.g. [27, 28]).

1.1 Three puzzles for pure big bang theory

1.1.1 Flatness problem

According to the cosmological principle, the universe is homogeneous and isotropic in everywhere when viewed in a smoothed cosmological scale. Therefore, the spacetime of

the universe is characterized by the maximally symmetric Robertson-Walker (RW) metric

$$ds^2 = g_{\mu\nu}dx^\mu dx^\nu = dt^2 - a(t)^2\left[\frac{dr^2}{1-Kr^2} + r^2 d\Omega^2\right], \tag{1.1}$$

where $a(t)$ is the scale factor and K is a constant that represents the spatial curvature. For $K = 0$, the spacetime is flat and infinite, whereas $K > 0$ ($K < 0$) corresponds to a spherical (hyperbolic) model. By substituting the RW metric into Einstein equations, one obtain the Friedmann equations

$$\frac{\dot{a}^2}{a^2} = \frac{8\pi G\rho}{3} - \frac{K}{a^2}, \tag{1.2}$$

$$\frac{3\ddot{a}}{a} = -4\pi G(3p+\rho), \tag{1.3}$$

where $\rho(t)$ and $p(t)$ are the proper energy density and pressure, G is the Newton constant and the dot $\cdot$ denotes the time derivative $\frac{d}{dt}$. The evolution of the scale factor $a(t)$ is governed by these equations. The Hubble parameter is defined as

$$H(t) = \frac{\dot{a}(t)}{a(t)}. \tag{1.4}$$

The first Friedmann equation (1.2) can be rewritten as

$$\Omega_K = -\frac{K}{a^2H^2} = 1 - \frac{\rho}{\rho_c} = 1 - \Omega, \tag{1.5}$$

where $\rho_c = \frac{3H^2}{8\pi G}$ is the critical energy density. The quantity Ω denotes the ratio of the total energy density (including matter, radiation and vacuum energy) to the critical energy density, while Ω_K is the counterpart for curvature. The analysis of recent CMB data [29] suggests that today's $|\Omega_K| < 0.01$ at 95% confidence level. This result is consistent with the type Ia supernova observations [30, 31, 32]. From the Friedmann equations (1.2) and (1.3), we can know that, $|\Omega_K| \propto t^{2/3}$ in the matter-dominated ($p = 0$) era, whereas $|\Omega_K| \propto t$ in the early radiation-dominated ($p = \rho/3$) era. Therefore, the value of $|\Omega_K|$ is even much smaller in the early stage of universe. It seems that the value of $|\Omega_K|$ is fine tuned. This is the flatness problem.

This problem is solved by inflation because the Hubble parameter $H(t)$ is nearly constant during inflation. Thus, $|\Omega_K| = \frac{|K|}{a^2H^2}$ decreases rapidly when the universe is expanding exponentially. In order to describe the dynamics of inflation, it is convenient to introduce the number of e-folds defined by

$$N = \log\left[\frac{a(t_f)}{a(t_i)}\right] = \int_{t_i}^{t_f} H(t)dt, \tag{1.6}$$

where t_i and t_f are the time of the start and end of inflation. If the value of $|\Omega_K|$ is nearly unity at the beginning of inflation, then today we will have

$$|\Omega_K|_0 = \frac{|K|}{a_0^2H_0^2} = e^{-2N}\left(\frac{a_{end}H_{end}}{a_0H_0}\right)^2, \tag{1.7}$$

where the subscript "end" denotes the end of inflation and "0" corresponds to the present epoch. Thus, in order to avoid the flatness problem, the expansion during inflation has the lower bound

$$e^N > \frac{a_{end}H_{end}}{a_0H_0} = \frac{a_{end}H_{end}}{a_{reh}H_{reh}}\frac{\dot{a}_{reh}}{\dot{a}_0}, \tag{1.8}$$

where "reh" is the reheat epoch. We roughly set the first fraction to be unity by assuming that not much happens to the scale factor and Hubble parameter from the end of inflation to the reheat epoch. Furthermore, the scale factor grows as some power of time in the later radiation and matter-dominated eras, we are able to use an estimate $\dot{a} \sim a/t$ and rewrite the second fraction of Eq. (1.8) as

$$\frac{\dot{a}_{reh}}{\dot{a}_0} = \frac{a_{reh}}{a_0}\frac{t_0}{t_{reh}} \approx \frac{T_{reh}}{T_0}\frac{t_0}{t_{reh}}. \tag{1.9}$$

If the energy scale of reheating is $10^9 GeV$, *i.e.* $T_{reh} \sim 10^{22}K$ and $t_{reh} \sim 10^{-33}$, we have

$$e^N > \frac{\dot{a}_{reh}}{\dot{a}_0} \sim 10^{28}, \tag{1.10}$$

that indicates inflation ought to last more than 60 e-folds. A similar result is obtained by a more precisely estimation in Ref [26]. In general, the duration of inflation may be greater than the exact number of e-folds to solve the flatness problem. Hence, inflation scenarios suggest that $|\Omega_K| \ll 1$.

1.1.2 Horizon problem

First of all, we have to introduce the concept of particle horizon [33]. The particle horizon is the maximal causal contact region for an observer at a fixed time t. Therefore, the radius of horizon can be defined by the maximal distance that center emitted lights could have traveled. In a RW spacetime, if the big bang started at a time $t = 0$, the radius of comoving horizon at time t is given by

$$d_h = \int_0^{r_{max}(t)} \frac{dr}{\sqrt{1-Kr^2}} = \int_0^t \frac{dt'}{a(t')} \sim \frac{1}{a(t)H(t)}. \tag{1.11}$$

To obtain this relation, we used the knowledge that the proper distance for a light ray is $d\tau^2 = 0$. There is no causal contact between two events that are separated by a distance larger than $2d_h$. From equation (1.11), we note that the particle horizon scale is proportional to the square root of $|\Omega_K|$ if $|K|$ is a non-zero constant. Thus, it is straightforward to reach the conclusion that the horizon size is growing during the evolution of the universe after the hot big bang. During the expansion of horizon, one would expect to observe strong signals of anisotropies and inhomogeneities at large scale between points which were not causal contacted before horizon entry. However, from the recent CMB anisotropic data [19, 29], there is no such signal. The universe is nearly isotropic and homogeneous at large scales. This is the so-called horizon problem.

In inflation scenarios, the scale factor $a(t)$ grows as e^{Ht} and the Hubble parameter H is nearly a constant. Hence, the comoving horizon scale (1.11) decreases as a factor e^N where N is the number of e-folds during inflation. The evolution of the comoving horizon

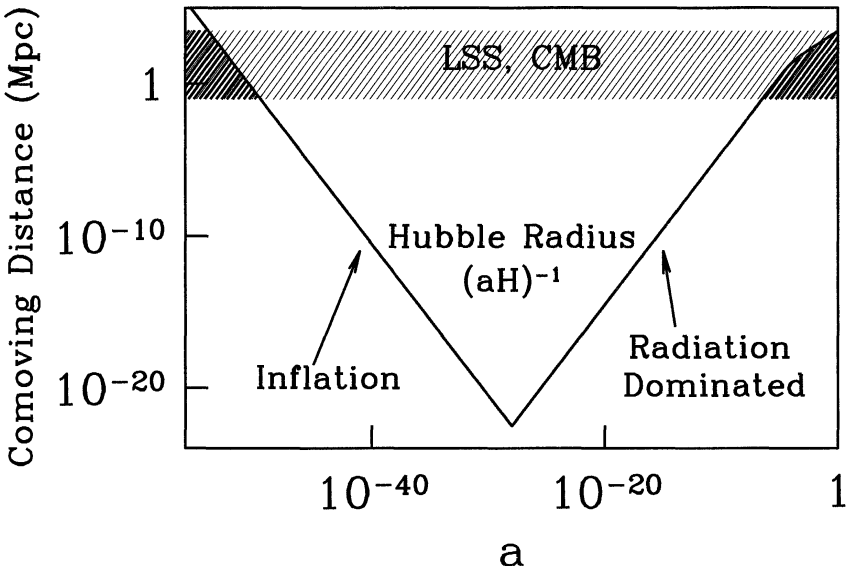

Figure 1.1: The evolution of the comoving Hubble radius (horizon) during inflation and the late evolution of the universe. The shaded band corresponds to the scale of observations at present. The points that are outside the horizon in the late time can be causal contacted before inflation. Figure from [23].

is shown in FIG. 1.1. Thus, all the observable universe can be inside the particle horizon and causally connected in the early stage, provides

$$e^N \geq \frac{a_{end}H_{end}}{a_0 H_0}. \tag{1.12}$$

This condition is the same as (1.8) for solving the flatness problem. Therefore, we know that the horizon problem can be solved if inflation lasts more then 60 e-folds.

1.1.3 Monopole problem

Many physicists believe that the electro-weak and strong interactions are grand unified with local symmetry under some simple symmetry group at a very high energy scale. (*cf.* Ref. [34] for an overview.) At an energy $M_G \approx 10^{16}GeV$, the grand unified symmetry is spontaneously broken, and finally into the gauge symmetry of the standard model. Due to the expansion history of the universe, this process can happen in the early time. However, many unwanted relics are produced in the process of spontaneous symmetry breaking. The most notorious one is the magnetic monopole. According to grant unified theories (GUT), the abundance of magnetic monopoles should be of the same order as that of nucleons, if monopoles do not annihilate by themselves. However, the ratio of monopoles to nucleons is experimentally found to be less than 10^{-30} [35]. This discrepancy can be also resolved by inflation, provided that the reheating temperature is lower than the GUT scale.During inflation, monopoles were produced after GUT symmetry breaking and were diluted rapidly by the expansion. Whereas, nucleons and photons which were generated after the epoch of reheating were not diluted by inflation. To solve the discrepancy of

order 10^{-30}, the scale factor should be increased by a factor of 10^{10} during inflation, which requires the number of e-folds to be greater than $\log 10^{10} = 23$.

For the above three problems, the most serious one is the horizon problem. There are some alternative solutions for other two problems. For example, the flatness problem can be solved by assuming the space is always flat. Moreover, if there is no GUT symmetry breaking, the monopole problem is not exist anymore. However, the horizon problem can be only solved naturally by inflation scenarios. Perhaps, cyclic universe theory could be an alternative solution for all these three problems [36]. But there is no evidence for it at present.

1.2 Slow-roll inflation

1.2.1 Slow-roll approximation

The evolution of the universe is governed by the Friedmann equations (1.2) and (1.3). We assume that there is an epoch when the universe is dominated by a nearly homogeneous scalar field ϕ before the radiation-dominated era. In this epoch, the energy-momentum tensor is

$$T^{\alpha}{}_{\beta} = -g^{\alpha\mu}\frac{\partial\phi}{\partial x^{\mu}}\frac{\partial\phi}{\partial x^{\beta}} + g^{\alpha}{}_{\beta}\left[\frac{1}{2}g^{\mu\nu}\frac{\partial\phi}{\partial x^{\mu}}\frac{\partial\phi}{\partial x^{\nu}} + V(\phi)\right], \tag{1.13}$$

where $V(\phi)$ is the potential for the scalar field. The scalar field can be divided into a homogeneous zeroth-order term $\phi^{(0)}(t)$ and a first-order perturbation $\delta\phi(t,\mathbf{x})$, *i.e.*

$$\phi(t,\mathbf{x}) = \phi^{(0)}(t) + \delta\phi(t,\mathbf{x}). \tag{1.14}$$

For the unperturbed field $\phi^{(0)}(t)$, the energy-momentum tensor can be rewritten as

$$T^{(0)\alpha}{}_{\beta} = g^{\alpha}{}_{0}g^{0}{}_{\beta}\left(\dot{\phi}^{(0)}\right)^{2} - g^{\alpha}{}_{\beta}\left[\frac{1}{2}\left(\dot{\phi}^{(0)}\right)^{2} - V(\phi^{(0)})\right], \tag{1.15}$$

due to its homogeneity. The energy density of $\phi^{(0)}$ is the time-time component of the energy momentum tensor

$$\rho = \frac{1}{2}\left(\dot{\phi}^{(0)}\right)^{2} + V(\phi^{(0)}), \tag{1.16}$$

and the pressure $p = T^{(0)i}{}_{i}$ is

$$p = \frac{1}{2}\left(\dot{\phi}^{(0)}\right)^{2} - V(\phi^{(0)}). \tag{1.17}$$

By substituting Eqs. (1.16) and (1.17) into the Friedmann equations (1.2) and (1.3), one obtains the equations

$$H^{2} = \frac{1}{3M_{pl}^{2}}\left[\frac{1}{2}\left(\dot{\phi}^{(0)}\right)^{2} + V(\phi^{(0)})\right], \tag{1.18}$$

$$\frac{\ddot{a}}{a} = \frac{1}{3M_{pl}^{2}}\left[-\left(\dot{\phi}^{(0)}\right)^{2} + V(\phi^{(0)})\right], \tag{1.19}$$

where the reduced Planck mass $M_{pl}^{-2} = 8\pi G$ with $\hbar = c = 1$ in the natural units system. Let us consider the case that the scalar field is dominated by its potential energy, *i.e.*

$V(\phi^{(0)}) \gg \frac{1}{2}\left(\dot{\phi}^{(0)}\right)^2$. In this case, the scalar field rolls down the potential very slowly, and the higher order terms of $\dot{\phi}^{(0)}$ are negligible. This is the so called *slow-roll approximation*. From Eq. (1.19), we have $\ddot{a} > 0$, that indicates an accelerating expansion of the unperturbed background. From Eq. (1.18), the Hubble parameter is approximately

$$H^2 \approx \frac{V(\phi^{(0)})}{3M_{pl}^2}. \tag{1.20}$$

By combining both equations, one obtains $a(t) = a(t_0)e^{Ht}$. Space expand exponentially during inflation. In order to describe the background evolution, cosmologists introduce the slow-roll parameters which can be defined in different manners [37]. In this thesis, we adopt the definition of Hubble flow functions [27]

$$\epsilon_{n+1} \equiv \frac{d\log|\epsilon_n|}{dN}, \quad n \geq 0, \tag{1.21}$$

where $\epsilon_0 \equiv H_{ini}/H$. During the epoch of inflation, the first slow-roll parameter ϵ_1 must be less than 1. When $\epsilon_1 = 1$, inflation ends and the slow-roll condition is violated. In the context of slow-roll inflation, the parameters ϵ_n can be expressed as

$$\epsilon_1 = \frac{M_{pl}^2}{2}\left(\frac{V_\phi}{V}\right)^2, \tag{1.22}$$

$$\epsilon_2 = 2M_{pl}^2\left[\left(\frac{V_\phi}{V}\right)^2 - \frac{V_{\phi\phi}}{V}\right], \tag{1.23}$$

$$\epsilon_2\epsilon_3 = 2M_{pl}^4\left[\frac{V_{\phi\phi\phi}V_\phi}{V^2} - 3\frac{V_{\phi\phi}}{V}\left(\frac{V_\phi}{V}\right)^2 + 2\left(\frac{V_\phi}{V}\right)^4\right], \tag{1.24}$$

where the subscript ϕ denotes the derivative $\frac{d}{d\phi}$. Thus, the shape of the inflationary potential is also presented by the values of slow-roll parameters.

1.2.2 Scalar field perturbations

There are primordial scalar and tensor fluctuations generated in the epoch of inflation. In this thesis, we focus on the scalar fluctuations which are detected in CMB experiments [19, 20]. Although the BICEP2 collaboration [21] stated that they discovered primordial B-mode polarization at 7σ confidence level and the tensor-to-scalar ratio $r = 0.2$, the recent Planck data analysis [38] shows that the BICEP2 signal is in the some order of dust radiations. Thus, the tensor fluctuation is not confirmed yet.

During inflation, the evolution of the scalar field is governed by the Klein-Gordon equation

$$\ddot{\phi} + 3H\dot{\phi} + V_\phi = 0. \tag{1.25}$$

We apply the homogeneous decomposition (1.14) in the Fourier components $\phi_{\mathbf{k}}$ of the field. Then, the Klein-Gordon equation for the first-order perturbation can be written as

$$\ddot{\delta\phi}_{\mathbf{k}} + 3H\dot{\delta\phi}_{\mathbf{k}} + \left(\frac{k}{a}\right)^2\delta\phi_{\mathbf{k}} + V_{\phi\phi}\delta\phi_{\mathbf{k}} = 0. \tag{1.26}$$

In a slow-roll inflation, $V_{\phi\phi}$ is proportional to the second slow-roll parameter (1.23). Hence, the last term in above equation can be neglected. The first-order perturbation can be treated as a massless free field. By transforming from coordinate time t to conformal time $\eta = -1/aH$, and rescaling $\psi \equiv a\delta\phi$, Eq. (1.26) becomes

$$\frac{d^2\psi_{\mathbf{k}}(\eta)}{d\eta^2} + (k^2 - 2(aH)^2)\psi_{\mathbf{k}}(\eta) = 0. \tag{1.27}$$

Due to the quantum nature of $\delta\phi$, the field ψ can be decomposed into its k-modes

$$(2\pi)^3\hat{\psi}_{\mathbf{k}}(\eta) = \psi_k(\eta)\hat{a}(\mathbf{k}) + \psi_k^*(\eta)\hat{a}^\dagger(-\mathbf{k}). \tag{1.28}$$

Here ψ_k is the mode function that satisfies Eq. (1.27) with the initial condition in Bunch-Davies vacuum [39]

$$\psi_k(\eta) = \frac{1}{\sqrt{2k}}e^{-ik\eta}. \tag{1.29}$$

Thus, the solution is given by

$$\psi_k(\eta) = \frac{e^{-ik\eta}}{\sqrt{2k}}\frac{(k\eta - i)}{k\eta}. \tag{1.30}$$

In order to study on the statistical behaviour of field fluctuation, we introduce the definition of the power spectrum as a dimensionless pre-factor of the correlation function that reads

$$\langle\psi_{\mathbf{k}}\psi_{\mathbf{k}'}\rangle = \frac{2\pi^2}{k^3}\mathcal{P}_\psi(k)\delta^3(\mathbf{k} + \mathbf{k}'). \tag{1.31}$$

At the time well after horizon exit of the k-mode, the term $k\eta \ll 1$ that can be negligible. Then, one obtain the power spectrum of ψ

$$\mathcal{P}_\psi(k,\eta) = \frac{k^3}{2\pi^2}|\psi_k(\eta)|^2 = \left(\frac{1}{2\pi\eta}\right)^2. \tag{1.32}$$

Recalling $\psi = a\delta\phi$, the power spectrum of first order perturbations $\delta\phi$ is giving by

$$\mathcal{P}_{\delta\phi}(k) = \frac{\mathcal{P}_\psi(k,\eta)}{a^2} = \left(\frac{H}{2\pi}\right)^2. \tag{1.33}$$

In inflation scenarios, the Hubble parameter H is nearly a constant. Hence, we say that the scalar field perturbation is frozen at super-horizon scale.

1.2.3 Curvature perturbation

Besides field fluctuations, the background spacetime is perturbed as well. In general, spacetime perturbations can be decomposed into scalar, vector and tensor modes. There is a decomposition theorem tell us that the three different perturbation modes are not coupling to each other up to the first order. We focus on the scalar perturbations in this thesis. In the conformal Newtonian gauge, the first-order perturbed metric can be written as

$$ds^2 = a^2[(1 + 2\Psi)d\eta^2 - (1 - 2\Phi)\delta_{ij}dx^i dx^j], \tag{1.34}$$

where Ψ and Φ are gravitational potentials (also named as Bardeen potentials). The curvature perturbation on uniform-density hypersurfaces is given by [16, 40]

$$\zeta = -\Psi - H\frac{\delta\rho}{\dot{\rho}}, \tag{1.35}$$

where $\delta\rho$ is the density perturbation. Note that ζ is gauge invariant and becomes time independent after horizon exit, it corresponds to observations of CMB anisotropies. Around the time of horizon-crossing, Ψ is negligible. Hence, to the first order, curvature perturbation ζ is given by

$$\zeta = -H\frac{\delta\phi}{\dot{\phi}^{(0)}}. \tag{1.36}$$

A few Hubble times after horizon exit, the power spectrum of ζ reads

$$\mathcal{P}_\zeta(k) = \left(\frac{H}{\dot{\phi}^{(0)}}\right)^2 \mathcal{P}_{\delta\phi}\Big|_k = \frac{1}{4\pi^2}\left(\frac{H^2}{\dot{\phi}^{(0)}}\right)^2\Big|_k. \tag{1.37}$$

In slow-roll scenarios, the second order derivative in the Klein-Gordon equation (1.25) is negligible. Thus, we have

$$\dot{\phi} = -\frac{V_\phi}{3H}. \tag{1.38}$$

By using Eqs (1.20) and (1.38), one obtains the $\mathcal{P}_\zeta(k)$ under slow-roll approximation, it reads

$$\mathcal{P}_\zeta(k) = \frac{V}{24\pi^2 M_{pl}^4 \epsilon_1}\Big|_k \tag{1.39}$$

In order to study on the scale-dependence of $\mathcal{P}_\zeta(k)$, we define the spectral index n_s as

$$n_s - 1 \equiv \frac{d\log\mathcal{P}_\zeta(k)}{d\log k}\Big|_{k_*} = -2\epsilon_1 - \epsilon_2, \tag{1.40}$$

where k_* is the pivot scale. Since $\epsilon_1 \ll 1$ and $\epsilon_2 \ll 1$ during slow-roll inflations, the power spectrum of primordial curvature perturbation is nearly scale invariant. From recent CMB observations [19, 20], we know that $\mathcal{P}_\zeta(k_*) \approx 2.2 \times 10^{-9}$ and $n_s \approx 0.96$ at the pivot scale $k_* = 0.002\text{Mpc}^{-1}$.

1.3 The generic δN formalism

There are two types of primordial perturbations can be generated during inflation. They are adiabatic and isocurvature perturbations. The slow-roll approximation is applicable for the adiabatic phase and problematic for the isocurvature phase. Therefore, a more generic method is needed. Hence, we would like to introduce the δN formalism [13, 41, 42, 43, 44].

The δN formalism is based on the separate universe assumption, which is usually regarded as a pair of assumptions. The first one is that the spatial gradients are negligible at a scale larger than smoothed scale. Given this assumption, one can deal the evolution of the universe as if it were homogeneous. The second assumption is that the universe is locally isotropic at each position. With both assumptions, the smoothed universe can be regarded as unperturbed and separated.

In order to investigate the scalar curvature perturbation, we consider uniform-energy density slices with which threads are comoving. Then, the spatial metric can be written as

$$g_{ij} = a^2(\mathbf{x}, t)\gamma_{ij}(\mathbf{x}), \tag{1.41}$$

where $a(\mathbf{x}, t) \equiv a(t)e^{\zeta(\mathbf{x},t)}$ and γ_{ij} is the unit matrix as we do not consider tensor perturbations. For two uniform-energy density slices at t_1 and t_2, the e-fold time between them is given by

$$N_{12}(\mathbf{x}) = \int_{t_1}^{t_2} \frac{\dot{a}}{a} dt = \zeta(\mathbf{x}, t_2) - \zeta(\mathbf{x}, t_1). \tag{1.42}$$

If one start from a flat slice (with $\zeta = 0$ which is a particular type of uniform-energy density slices) and end at time t with a uniform-energy density slices, then the curvature perturbation is

$$\zeta(\mathbf{x}, t) = \delta N(\mathbf{x}, t) = N(\mathbf{x}, t) - N(\mathbf{x}, 0). \tag{1.43}$$

This is the so-called δN formula. Note that the expansion N is a function of the energy density and scalar fields. In the single scalar field case, it can be rewritten as

$$\delta N = N(\rho(t), \phi(\mathbf{x})) - N(\rho(t), \phi^{(0)}) = N_\phi \delta\phi(\mathbf{x}) + \mathcal{O}(\delta\phi)^2. \tag{1.44}$$

Thus, we obtain the power spectrum of ζ in the first order

$$\mathcal{P}_\zeta = N_\phi^2 \mathcal{P}_{\delta\phi} = N_\phi^2 \left(\frac{H}{2\pi}\right)^2. \tag{1.45}$$

By rewriting

$$N_\phi = \frac{dN}{d\phi} = -\frac{H}{\dot{\phi}}, \tag{1.46}$$

one obtains

$$N_\phi = \frac{V}{M_{pl} V_\phi}, \tag{1.47}$$

with slow-roll approximation. Therefore, the power spectrum reads

$$\mathcal{P}_\zeta = \frac{V}{24\pi^2 M_{pl}^4 \epsilon_1}, \tag{1.48}$$

that returns to the result (1.39) in the previous section.

We note that the δN formalism is a powerful tool for calculating primordial curvature perturbations. It can be applied to the cases beyond slow-roll approximation.

1.4 Topics of this thesis

In this thesis, we discuss on a few peculiar problems about primordial scalar fluctuations during inflation. This manuscript is divided into three independent parts.

In the first part, we investigate curvature perturbations and non-Gaussianities from hybrid inflation models (original [45], supersymmetric F-term [46, 47] and D-term [48, 49]) with a mild waterfall phase [50, 51, 52], taking into account the contribution of entropy

(isocurvature) modes. By using δN formalism, non-Gaussianities and curvature perturbations are calculated both analytically and numerically. We study on the regime of the mild waterfall inflation that last more than about 60 e-folds time. We find that the non-Gaussianity parameter f_{NL} and the spectral index n_s can fit well with CMB anisotropies observations [19, 20]. However, at the same time, the spectrum amplitude increase by serval orders of magnitude due to the contribution of entropy modes. Therefore, all considered hybrid models are ruled out by CMB observations.

The second part is devoted to testing inflation and curvaton scenarios with CMB distortions. CMB spectral distortions are caused by energy injection processes for the monopole, and can be detected by future experiments such as the Primordial Inflation Explorer (PIXIE) [53] and the Polarized Radiation Imaging and Spectroscopy (PRISM) [54, 55]. We focus on the spectral distortions caused by Silk damping that can give information for the primordial scalar power spectrum on small scales. In this manuscript, a model-oriented approach is adopted. All 49 single field inflation models listed in Ref. [27] are examined, and only the original hybrid model can be detected by PIXIE in a tuned parameter regime. After that, we investigate on three effective multi-field scenarios (with softly and suddenly turning trajectories, and with a mild waterfall trajectory) and curvaton scenarios. We find that softly trajectories and curvaton scenarios cannot induce distortions at detectable level, whereas a sudden turn in field space or a mild waterfall trajectory can lead to an observable amount of CMB distortion.

Finally, the third part is dedicated to self-regulatory mechanism for leading infrared (IR) behaviour of scalar correlation functions. For a scalar field on de Sitter background, the quantum fluctuations which behave as classic perturbations are proportional to the term $\frac{H^2}{m^2}$, where m is the mass of the field. When the scalar field is light, *i.e.* $m^2 \ll H^2$, the soft modes will be accumulated at horizon-crossing that leads to IR divergence in correlation functions. In this part, we develop a field theoretical method from first principles based on the closed time path formalism. This method can be employed to study the time evolution of scalar perturbations during inflation since it is time-dependent. In the late time limit, we find agreement with the leading IR correlations found using stochastic methods [56] up to all loop orders.

Part I

Non-Gaussianities and curvature perturbations from hybrid inflation

Contents

Introduction

Hybrid models are well motivated because they can be embedded in various high energy frameworks such as supersymmetry (SUSY) [46, 47, 49, 57, 58, 59], supergravity (SUGRA) [48, 60], and GUT [61, 62, 63]. In the usual description of those models, inflation is driven by an inflaton field which rolls slowly along a nearly flat valley. It ends nearly instantaneously when another field (the waterfall field) gains a nonzero value and triggers a waterfall phase. In this standard regime of a fast waterfall, the original hybrid model induces a slightly blue tilted power spectrum which is strongly disfavored by CMB observations [19, 20]. Moreover, at the end of inflation, the Z_2 symmetry breaking of the potential leads to the formation of domain walls that will induce catastrophic consequence for cosmology.

Recent development have shown that these problems can be resolved with a sufficiently mild waterfall phase [50, 51]. After a 60 e-folds expansion in the waterfall phase, topological defects are conveniently stretched outside the observable universe. Furthermore, the observable perturbation modes exit the horizon during the waterfall with a red power spectrum of perturbation. For the most well-known supersymmetric realization of the hybrid inflation, the so-called F-term and D-term models, similar conclusions have been obtained [52].

Moreover, for symmetric both F-term and D-term models, which are the most well know supersymmetric realization of the hybrid inflation, the contribution of cosmic strings formed at the critical point must be considered. The F-term model can satisfy the constraints of the WMAP observation, while the D-term model was strongly disfavored [64, 65]. However, with the Planck data, the degeneracy between the spectral index and the string tension is strongly reduced, and both models appear to be ruled out in the standard regime [66]. As shown in Ref. [52], these problems can be also resolved with a mild waterfall phase last more than 60 e-folds time.

In this part, we evaluate the power spectrum of curvature perturbations and the level of non-Gaussianities produced in the mild waterfall regime both analytically and numerically. The first chapter is devoted to introducing the considered hybrid models and a unified parametrization of the potential. In order to include the contribution of entropic modes in our evaluation, the dynamics and methods for multifield cases are introduced in the second chapter. In chapter 4 and 5, the level of non-Gaussianities and the power spectrum of curvature perturbations are computed respectively. In the last chapter of this part, we have a short discussion on our results as a conclusion.

Chapter 2

Hybrid models

2.1 Original Hybrid model

In 1993, Linde [45] proposed the original hybrid inflation model as a new way to stop inflation by a spontaneous symmetry breaking. It is a two-field model with an inflaton field ϕ and a waterfall field ψ. It's potential reads,

$$V(\phi,\psi) = \Lambda\left[\left(1-\frac{\psi^2}{M^2}\right)^2 + \frac{\phi^2}{\mu^2} + \frac{2\phi^2\psi^2}{\phi_c^2 M^2}\right], \tag{2.1}$$

where M, μ and ϕ_c are three parameters of mass dimension. FIG. 2.1 is a plot of the potential. Inflation occurs when the inflaton rolls along the valley $\langle\psi\rangle = 0$ (angle brackets denote the vacuum expectation value (vev)). Soon after the inflaton crosses the critical point ϕ_c, the waterfall field develops a Higgs-type tachyonic instability in the transverse direction, and inflation ends. After that, the inflaton evolves toward one of its true minima $\langle\phi\rangle = 0$, $\langle\psi\rangle = \pm M$, whereas the instability triggers a tachyonic preheating era [67, 68, 69, 70, 71, 72].

In common picture, the waterfall phase is nearly instantaneous, and the 2-field dynamics can be approximated to the evolution of inflaton alone the valley. The effective one-field potential is given by

$$V(\phi) = \Lambda\left(1+\frac{\phi^2}{\mu_{\rm VHI}^2}\right). \tag{2.2}$$

Inflation ends at the time when inflaton ϕ reaches the critical value ϕ_c. By defining $x \equiv \phi/\mu_{\rm VHI}$, the slow-roll parameters are written as

$$\epsilon_1 = \frac{2M_{\rm pl}^2 x^2}{\mu^2\left(1+x^2\right)^2}, \tag{2.3a}$$

$$\epsilon_2 = \frac{4M_{\rm pl}^2\left(-1+x^2\right)}{\mu^2\left(1+x^2\right)^2}. \tag{2.3b}$$

When $x = 1$, the first slow-roll parameter ϵ_1 reaches its maximum. Hence, the inflation can be divided into large field ($\phi > \mu_{\rm VHI}$) phase and small field ($\phi < \mu_{\rm VHI}$) phase. To avoid the regime where the slow-roll dynamics is violated at the transition between both phase, it requires

$$\mu_{\rm VHI} > \frac{1}{\sqrt{2}} M_{pl}. \tag{2.4}$$

In addition, in the slow-roll regime, the expansion of universe reads

$$N(x) = \frac{\mu_{\rm VHI}^2}{4M_{\rm pl}^2}\left[x^2 - x_i^2 - 2\log\left(\frac{x}{x_i}\right)\right], \tag{2.5}$$

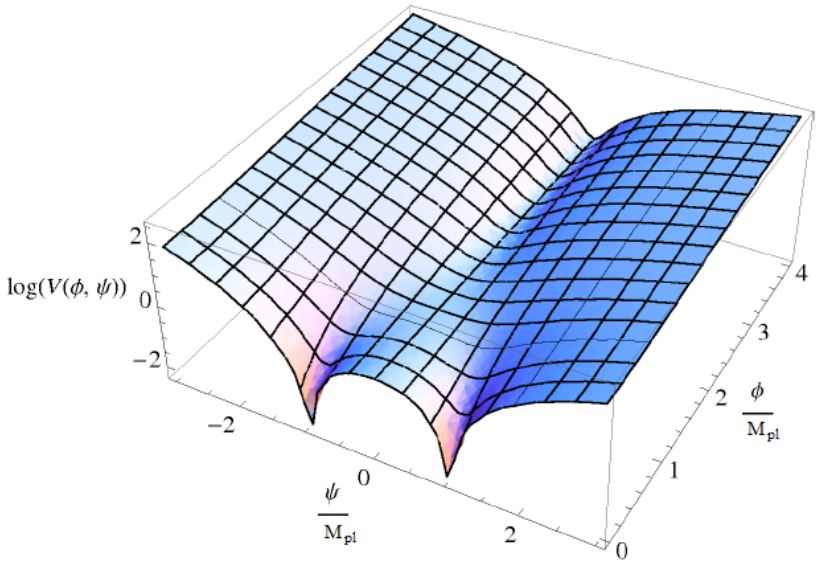

Figure 2.1: Logarithm of the original hybrid potential with $\Lambda = M = \phi_c = \mu/100 = M_{pl}$. Figure from [50].

where x_i is the initial field value. If the observable modes exit the Hubble horizon at the small field phase, the number of e-folds is typically larger than 60. However, the first slow-roll parameter ϵ_1 is very small and the second slow-roll parameter ϵ_2 is negative which leads to a blue spectral tilt $n_s = 1 - 2\epsilon_1 - \epsilon_2 > 1$ that is ruled out by CMB observations [19, 20].

2.2 Supersymmetric F-term model

The F-term inflation model [46, 47] is one of the minimal supersymmetric versions of hybrid inflation. Its superpotential is given by

$$W = \kappa \widehat{S}(\widehat{\bar{H}}\widehat{H} - m^2) \ , \tag{2.6}$$

where $\widehat{S}$ is a gauge singlet superfield and the superfields $\widehat{H}$ ($\widehat{\bar{H}}$) transform in the (anti-)fundamental representation of SU($\mathcal{N}$). The correspondence tree level potential reads

$$V_0 = \kappa^2 \left(|\bar{H}H - m^2|^2 + |S\bar{H}|^2 + |SH|^2 \right) \ , \tag{2.7}$$

where now S, H and $\bar{H}$ are complex scalar fields. When S acquires a vev and $\langle H \rangle = \langle \bar{H} \rangle = 0$, a trajectory that support hybrid inflation can be obtained. In this case, there are $\mathcal{N}$ complex scalar fields $H_+ = \frac{1}{\sqrt{2}}(H + \bar{H})$ of mass square $m_+^2 = \kappa^2(|S|^2 - M^2)$, $\mathcal{N}$ complex scalar fields $H_- = \frac{1}{\sqrt{2}}(H + \bar{H})$ of mass square $m_-^2 = \kappa^2(|S|^2 - M^2)$, and $\mathcal{N}$ Dirac fermions of mass κS. A large mass is given to H_- by the D term that implies the vev of H_- can be neglected. The inflaton can be identify as $\phi = \sqrt{2}|S|$ and the waterfall field as $\psi = \sqrt{2}H_+$. Thus, the tree-level potential can be written as

$$V_0(\phi, \psi) = \kappa^2 m^4 \left[\left(1 - \frac{\psi^2}{4m^2} \right)^2 + \frac{\phi^2 \psi^2}{4m^4} \right] = \frac{\kappa^2}{4} \phi_c^4 \left[\left(1 - \frac{\psi^2}{2\phi_c^2} \right)^2 + \frac{\phi^2 \psi^2}{\phi_c^4} \right] \ . \tag{2.8}$$

When the inflaton crosses the critical point, *i.e.* $\phi \geq \phi_{\rm c} = \sqrt{2}m$ and $\langle\psi\rangle = 0$, the potential energy $\Lambda = \kappa^2 m^4$ spontaneously breaks supersymmetry. Moreover, in terms of these degrees of freedom, the one loop correction to the potential is

$$\begin{aligned} V_1 &= \frac{\kappa^4 \mathcal{N}}{128\pi^2}\left[(\phi^2-\phi_{\rm c}^2)^2 \log\left(\kappa^2\frac{\phi^2-\phi_{\rm c}^2}{2Q^2}\right)\right. \\ &\left. +(\phi^2+\phi_{\rm c}^2)^2 \log\left(\kappa^2\frac{\phi^2+\phi_{\rm c}^2}{2Q^2}\right) - 2\phi^4\log\left(\frac{\kappa^2\phi^2}{2Q^2}\right)\right], \end{aligned} \tag{2.9}$$

where Q is a renormalization scale. SUSY F-term inflation is driven by the potential $V = V_0 + V_1$. As discussed in [52], it is a good approximation to treat the one-loop potential to linear order in the near critical point regime. Then the dynamics relate to the first derivative of the one-loop potential

$$\left.\frac{\partial V_1(\phi)}{\partial\phi}\right|_{\phi=\phi_{\rm c}} = \frac{\kappa^4\mathcal{N}}{8\pi^2}\phi_{\rm c}^3\log 2\,. \tag{2.10}$$

It requires $\kappa \ll \phi_{\rm c}^2/M_{\rm P}^2$ for realizing a substantial amount of e-folds in the waterfall phase [52]. Therefore, the second order derivatives of the one-loop potential which are of order $\frac{\kappa^4 M^2}{16\pi^2}\times\mathcal{O}$ can be neglected, because there is no phenomenologically relevant contribution to the observable power spectrum from them.

2.3 Supersymmetric D-term model

The D-term inflation model [48, 49] is another minimal supersymmetric version of hybrid inflation. The superpotential is

$$W = \kappa\widehat{S}\widehat{\bar{H}}\widehat{H}\ , \tag{2.11}$$

where $\widehat{S}$ is again a singlet and $\widehat{H}$ and $\widehat{\bar{H}}$ are superfields in the one-dimensional representation of a U(1) gauge group. The D-term is given by

$$D = \frac{g}{2}\left(|H|^2 - |\bar{H}|^2 + m_{\rm FI}^2\right)\ , \tag{2.12}$$

where $m_{\rm FI}$ is the Fayet-Iliopoulos term. The canonically normalized inflaton field is again $\phi = \sqrt{2}|S|$, whereas now the waterfall field is given by $\psi = \sqrt{2}|\bar{H}|$ of the mass square $\kappa^2\phi^2/2 - g^2 m_{\rm FI}^2/4$ for $\langle\psi\rangle = 0$. Hence, the critical point is

$$\phi_{\rm c} = \frac{1}{\sqrt{2}}\frac{g}{\kappa}m_{\rm FI}\,. \tag{2.13}$$

When the inflaton ϕ evolves blow this critical value, the waterfall field ψ becomes tachyonically unstable. Then, the tree level potential is given by

$$\begin{aligned} V_0 &= \kappa^2\left(|H\bar{H}|^2 + |SH|^2 + |S\bar{H}|^2\right) + \frac{1}{2}D^2 \\ &= \frac{g^2}{8}m_{\rm FI}^2\left[\left(1-\frac{\psi^2}{2m_{\rm FI}^2}\right)^2 + 2\frac{\kappa^2}{g^2}\frac{\phi^2\psi^2}{m_{\rm FI}^4}\right] \\ &= \frac{\kappa^4}{2g^2}\phi_{\rm c}^4\left[\left(1-\frac{g^2}{4\kappa^2\phi_{\rm c}^2}\psi^2\right)^2 + \frac{g^2}{2\kappa^2\phi_{\rm c}^4}\phi^2\psi^2\right]. \end{aligned} \tag{2.14}$$

The one-loop potential takes the same form as for the F-term case, Eq. (2.9) when setting $\mathcal{N} = 1$.

2.4 Unified parametrization

In order to study the F-term and D-term and the original hybrid models in a unified approach, it is convenient to use the parametrization

$$V(\phi,\psi) = \Lambda\left[\left(1-\frac{\psi^2}{M^2}\right)^2 + \left(\frac{\phi}{\mu}\right)^p + \frac{2\phi^2\psi^2}{M^2\phi_c^2}\right], \tag{2.15}$$

where M is the position of the global minima, and ϕ_c denotes the critical instability point along the valley. The parameter p is used to identify models. For the original hybrid model, one has $p = 2$. As $p = 1$, the potential describes the dynamics for the F-term and D-term models [52]. The corresponding relations of the model parameters for F-term and D-term models are shown in TABLE 2.1.

	F-term	D-term
Λ	$\kappa^2 m^4$	$\frac{\kappa^4}{2g^2}\phi_c^4 = \frac{g^2}{8}m_{\rm FI}^4$
ϕ_c	$\sqrt{2}m$	$\frac{g}{\sqrt{2}\kappa}m_{\rm FI}$
M	$2m$	$\sqrt{2}m_{\rm FI}$
$1/\mu$	$\frac{\sqrt{2}\mathcal{N}\kappa^2\log(2)}{4\pi^2 m}$	$\frac{\sqrt{2}\kappa g\log 2}{4\pi^2 m_{\rm FI}}$

Table 2.1: Parameters to be substituted into the potential (2.15) in order to obtain the F- and D-term models close to the critical point.

With the unified potential, it is straightforward to write down the derivatives

$$\frac{\partial V}{\partial\phi} = \frac{p\Lambda\phi^{p-1}}{\mu^p}\left(1+\frac{4\mu^p\phi^{2-p}\psi^2}{pM^2\phi_c^2}\right), \tag{2.16a}$$

$$\frac{\partial V}{\partial\psi} = \frac{4\psi\Lambda}{M^2}\left(\frac{\phi^2-\phi_c^2}{\phi_c^2}+\frac{\psi^2}{M^2}\right), \tag{2.16b}$$

$$\frac{\partial^2 V}{\partial\phi^2} = \frac{p(p-1)\Lambda\phi^{p-2}}{\mu^p}+\frac{4\Lambda\psi^2}{M^2\phi_c^2}, \tag{2.16c}$$

$$\frac{\partial^2 V}{\partial\psi^2} = \frac{4\Lambda}{M^2}\left(\frac{\phi^2-\phi_c^2}{\phi_c^2}+\frac{3\psi^2}{M^2}\right), \tag{2.16d}$$

$$\frac{\partial^2 V}{\partial\phi\partial\psi} = \frac{8\Lambda\psi\phi}{M^2\phi_c^2}. \tag{2.16e}$$

These derivatives are useful for deriving the dynamics and the phenomenological consequences of hybrid inflation in following chapters. Moreover, in following chapters of this part, we employ the standard definition for the slow-roll parameters $\eta_{XY} = M_{\rm pl}^2[\partial^2 V/(\partial X\partial Y)]/V$, where X and Y correspond to the canonically normalized fields ϕ and ψ.

Chapter 3

Dynamics and methodology

As stated in the last chapter, a mild waterfall phase is a plausible solution for the problems with hybrid inflation models. In the mild waterfall case, inflation is driven by both the inflaton and the waterfall fields. Thus, the one-field effective potential Eq. (2.2) is not available anymore, one has to treat the hybrid inflation as a multifield inflation. Therefore, in this chapter, we are going to introduce the dynamics and the δN formalism for a multifield inflation.

3.1 Multifield background dynamics

In single-field case, we know that the evolution of the spacetime and field itself are governed by Friedmann equations (1.2), (1.3) and Klein-Gordon equation (1.25). If the universe is filled with n nearly homogeneous real scalar field $\phi_{i=1,2\ldots,n}$, then the corresponding Friedmann equations and Klein-Gordon equations reads

$$H^2 = \frac{1}{3M_{\rm pl}^2}\left[\frac{1}{2}\sum_{i=1}^{n}\dot{\phi}_i^2 + V(\phi_{i=1,\ldots,n})\right] \ , \tag{3.1}$$

$$\frac{\ddot{a}}{a} = \frac{1}{3M_{\rm pl}^2}\left[-\sum_{i=1}^{n}\dot{\phi}_i^2 + V(\phi_{i=1,\ldots,n})\right] \ , \tag{3.2}$$

and

$$\ddot{\phi}_i + 3H\dot{\phi}_i + \frac{\partial V}{\partial \phi_i} = 0 \ , \tag{3.3}$$

where $V(\phi_{i=1,\ldots,n})$ is the field potential. To describes the collective evolution of all the fields along the classical trajectory, an *adiabatic field* can be defined with the velocity [73]

$$\dot{\sigma} \equiv \sqrt{\sum_{i=1}^{n}\dot{\phi}_i^2} \ . \tag{3.4}$$

Thus, the adiabatic field satisfies

$$\ddot{\sigma} + 3H\dot{\sigma} + V_\sigma = 0 \ , \tag{3.5}$$

where

$$V_\sigma \equiv \sum_{i=1}^{n} u_i \frac{\partial V}{\partial \phi_i} \ , \tag{3.6}$$

with $u_i \equiv \dot{\phi}_i/\dot{\sigma}$ are the components of a unit vector along the field trajectory.

3.2 δN formalism

In section 1.3, we know that the scalar curvature perturbation $\zeta(\mathbf{x}, t)$ equates the e-fold variation $\delta N(\mathbf{x}, t)\delta N(\mathbf{x}, t)$. In the multifield case, δN must be a function of all field values. Then, it can be written as

$$\zeta = \delta N(\rho(t), \phi_1, \phi_2, \cdots) \simeq \sum_{i=1}^{n} N_{,i}\delta\phi_i + \frac{1}{2}\sum_{i,j=1}^{n} N_{,ij}\delta\phi_i\delta\phi_j \ , \tag{3.7}$$

where the notation

$$N_{,i} \equiv \frac{\partial\delta N_{\rm i}^{\rm f}}{\partial\phi_i^{\rm i}}, N_{,ij} \equiv \frac{\partial^2\delta N_{\rm i}^{\rm f}}{\partial\phi_i^{\rm i}\partial\phi_j^{\rm i}} \ , \tag{3.8}$$

is used. Let we choose the initial hypersurface at the time t_* which is the time of observable pivot scale $k_* = 0.05$ Mpc^{-1} exit the particle horizon. Then, the power spectrum amplitude and spectral index are given by [74]

$$\mathcal{P}_\zeta(k_*) = \frac{H_*^2}{4\pi^2}\sum_i N_{,i}^2 \, , \tag{3.9}$$

$$n_{\rm s} - 1 = -2\epsilon_{1*} + \frac{2\sum_{ij}\dot{\phi}_{i*}N_{,j}N_{,ij}}{H_*\sum_i N_{,i}^2} \, , \tag{3.10}$$

where star subscripts indicate quantities evaluated at t_*. With the definition of bispectrum

$$\langle\zeta_{\mathbf{k}_1}\zeta_{\mathbf{k}_2}\zeta_{\mathbf{k}_3}\rangle \equiv (2\pi)^3 B_\zeta(k_1, k_2, k_3)\delta^3(\mathbf{k}_1 + \mathbf{k}_2 + \mathbf{k}_3), \tag{3.11}$$

the non-Gaussian properties can be specified by a parameter $f_{\rm NL}$ that is defined as [75, 76]

$$B_\zeta \equiv -\frac{6}{5}f_{\rm NL}(k_1, k_2, k_3)(P_\zeta(k_1)P_\zeta(k_2) + cyclicpermutations), \tag{3.12}$$

where $P_\zeta(k) = \frac{2\pi^2}{k^3}\mathcal{P}_\zeta(k)$. By applying the δN formalism to the multifield case, one obtains the non-Gaussianity parameter[74]

$$f_{\rm NL} = -\frac{5}{6}\frac{\sum_{i,j} N_{,i}N_{,j}N_{,ij}}{\left(\sum_i N_{,i}^2\right)^2}. \tag{3.13}$$

In the δN formalism, it requires the final surface to be of uniform energy density. However, in our calculation, we have chosen a constant field value hypersurface as the final surface. This approximation leads to accurate predictions because the e-folds differences between these two surfaces can be negligible compared to the e-fold variations between trajectory reaching them. We will check this statement later in chapter 4 both analytically and numerically. By the virtue of this approximation, one can obtain a more precise value of the inflaton when the non-perturbed trajectory breaks the slow-roll approximation.

Note that the number of e-folds N^t can be considered as a reparametrization of time, $dN^t = Hdt$. For example, we have $N^t = Ht$ for a pure de Sitter inflation, where the Hubble parameter H is constant. The function N that is employed to calculate the spectra of the curvature perturbation at a scale k is then given by

$$N = N_{\rm end}^t - N_k^t + \text{const.}. \tag{3.14}$$

The constant term is irrelevant in the calculation, because the curvature perturbation is obtained from the derivatives with respect to the fields and the fluctuations of these.

3.3 The linear theory of multi-field perturbations

3.3.1 Perturbed equations

In the case of scalar curvature perturbation, the first-order perturbed metric is given by Eq. (1.34)

$$ds^2 = a^2[(1+2\Psi)d\eta^2 - (1-2\Phi)\delta_{ij}dx^i dx^j], \tag{3.15}$$

where Ψ and Φ are Bardeen potentials. From the spatial nondiagonal linear perturbed Einstein equations in the longitudinal gauge, one obtains the relation $\Psi = \Phi$. Then, the $(0,0)$, $(0,i)$ and (i,i) equations can be written as

$$-3\mathcal{H}(\Phi' + \mathcal{H}\Phi) + \nabla^2\Phi = \frac{4\pi}{m_{\rm pl}^2}\sum_{i=1}^{n}\left(\phi_i'\delta\phi_i' - \phi_i'^2\Phi + a^2\frac{\partial V}{\partial\phi_i}\delta\phi_i\right) , \tag{3.16}$$

$$\Phi' + \mathcal{H}\Phi = \frac{4\pi}{m_{\rm pl}^2}\sum_{i=1}^{n}\phi_i'\delta\phi_i , \tag{3.17}$$

$$\Phi'' + 3\mathcal{H}\Phi' + \Phi\left(2\mathcal{H}' + \mathcal{H}^2\right) = \frac{4\pi}{m_{\rm pl}^2}\sum_{i=1}^{n}\left(\phi_i'\delta\phi_i' - \phi_i'^2\Phi - a^2\frac{\partial V}{\partial\phi_i}\delta\phi_i\right) , \tag{3.18}$$

where a prime denotes the conformal time derivative, the conformal Hubble parameter $\mathcal{H} \equiv a'/a$ and $\delta\phi_i$ is the perturbation of the scalar field ϕ_i. In addition, the linear perturbed Klein-Gordon equations read

$$\delta\phi_i'' + 2\mathcal{H}\delta\phi_i' - \nabla^2\delta\phi_i + \sum_{j=1}^{n}a^2\delta\phi_j\frac{\partial^2 V}{\partial\phi_i\partial\phi_j} = 2(\phi_i'' + 2\mathcal{H}\phi_i')\Phi + 4\phi_i'\Phi' . \tag{3.19}$$

Only if the cross derivatives of the potential and the Bardeen potential are vanishing, the field perturbations are decoupled to each other. By combining Eq. (3.16), Eq. (3.18), and Eq. (3.17), it is straightforward to derive the evolution equation for the Bardeen potential

$$\Phi'' + 6\mathcal{H}\Phi' + (2\mathcal{H}' + 4\mathcal{H}^2)\Phi - \nabla^2\Phi = -\frac{8\pi}{m_{\rm pl}^2}a^2\sum_{i=1}^{n}\frac{\partial V}{\partial\phi_i}\delta\phi_i . \tag{3.20}$$

Moreover, the curvature perturbation is defined as

$$\zeta \equiv \Phi - \frac{\mathcal{H}}{\mathcal{H}' - \mathcal{H}^2}(\Phi' + \mathcal{H}\Phi) . \tag{3.21}$$

We know that $\mathcal{H}' - \mathcal{H}^2 = -4\pi\sigma'^2/m_{\rm pl}^2$ from the background dynamics. Thus, with Eq. (3.17), the comoving curvature perturbation can be rewritten as

$$\zeta = \Phi + \frac{\mathcal{H}}{\sigma'^2}\sum_{i=1}^{n}\phi_i'\delta\phi_i . \tag{3.22}$$

Therefore, according to the background and the perturbed Einstein equations, the evolution of ζ is governed by equation [77]

$$\begin{aligned}\zeta' &= \frac{m_{\rm pl}^2}{4\pi}\frac{\mathcal{H}}{\sigma'^2}\nabla^2\Phi - \frac{2\mathcal{H}}{\sigma'^2}\left[a^2\sum_{i=1}^{n}\phi_i'\frac{\partial V}{\partial\phi_i} - \frac{a^2}{\sigma'^2}\left(\sum_{i=1}^{n}\phi_i'\frac{\partial V}{\partial\phi_i}\right)\left(\sum_{i=1}^{n}\phi_i'\delta\phi_i\right)\right] \\ &= \frac{m_{\rm pl}^2}{4\pi}\frac{\mathcal{H}}{\sigma'^2}\nabla^2\Phi - \frac{2\mathcal{H}}{\sigma'^2}\perp_{ij}a^2\frac{\partial V}{\partial\phi_i}\delta\phi_j ,\end{aligned} \tag{3.23}$$

where the orthogonal projector is defined as $\perp_{ij} \equiv \mathrm{Id} - u_i u_j$. In the last line of this equation, the second term, which is sourced by isocurvature perturbations, should vanish in a single-field model.

3.3.2 Numerical integration

In Ref. [77], an exact numerical method for inflation models had been introduced. Here, we give only the guidelines for computing the power spectrum of curvature perturbations in a multifield scenario. For convenience, we use the number of e-folds as the time variable. After expanding in Fourier modes, Eq. (3.19) reads [77]

$$\frac{\mathrm{d}^2\delta\phi_i}{\mathrm{d}N^{t2}} + (3-\epsilon_1)\frac{\mathrm{d}\delta\phi_i}{\mathrm{d}N^t} + \sum_{j=1}^{n}\frac{1}{H^2}\frac{\partial^2 V}{\partial\phi_i\partial\phi_j}\delta\phi_j + \frac{k^2}{a^2H^2}\delta\phi_i = 4\frac{\mathrm{d}\Phi}{\mathrm{d}N^t}\frac{\mathrm{d}\phi_i}{\mathrm{d}N^t} - \frac{2\Phi}{H^2}\frac{\partial V}{\partial\phi_i}\ . \quad (3.24)$$

Here, $\delta\phi_i = \delta\phi_i(k,\eta)$ and we may use $k = |\mathbf{k}|$ because of isotropy. The initial condition for the $\delta\phi_i$ is given by the quantization of the field perturbations in the limit $k \gg aH$. In a similarly way to the one field case in section 1.2.2, the field operator can be expressed as

$$\delta\phi_i(\eta,\mathbf{x}) = \int \frac{d^3k}{(2\pi)^3}\Big[a_i(\mathbf{k})\mathrm{e}^{-i\mathbf{k}\cdot\mathbf{x}}\delta\phi_i(k,\eta) + \mathrm{h.c.}\Big]\,, \quad (3.25)$$

where h.c. stands for Hermitian conjugation and the operator $a_i(\mathbf{k})$ satisfies the commutation relation $[a_i(\mathbf{k}), a_j^\dagger(\mathbf{k}')] = (2\pi)^3\delta_{ij}\delta(\mathbf{k}-\mathbf{k}')$. Moreover, the normalized quantum modes are defined by a rescaling

$$v_{i,k}(\eta) = a\delta\phi_i(k,\eta)\,. \quad (3.26)$$

They obey the equation $v_{i,k}'' + k^2 v_{i,k} = 0$ as the mass terms can be neglected. In the regime $k \gg aH$, we have

$$\lim_{k/aH\to+\infty} v_{k,i}(\eta) = k\mathrm{e}^{-ik(\eta-\eta_\mathrm{i})}\ . \quad (3.27)$$

Thus, the initial conditions for the field perturbations can be written as

$$\delta\phi_{i,\mathrm{i.c.}} = \frac{1}{\sqrt{2k}}\frac{1}{a_\mathrm{i.c.}}\ , \quad (3.28)$$

$$\left[\frac{\mathrm{d}\delta\phi_i}{\mathrm{d}N^t}\right]_\mathrm{i.c.} = -\frac{1}{a_\mathrm{i.c.}\sqrt{2k}}\left(1 + i\frac{k}{a_\mathrm{i.c.}H_\mathrm{i.c.}}\right)\ , \quad (3.29)$$

where the quantities with a subscript i.c. correspond to their initial values. If one integrates the perturbations from the onset of inflation, numerical integration of sub-horizon modes will cost a great deal of time because the total number of e-folds can be much large than N_*. In order to improve the performance, integration of the perturbations is started later when the condition

$$\frac{k}{\mathcal{H}(n_\mathrm{i.c.})} = C_k \gg 1 \quad (3.30)$$

is satisfied, where C_k is a constant characterizing the decoupling limit. In conclusion, there are four steps for the numerical integration of multi-field perturbations:

1. Integrate the background dynamics until the end of inflation, in order to gain the value of $N^t_{\rm end}$ and $N^t_{\rm end} - N^t_*$.

2. Integrate the background dynamics again, until $N^t_{\rm i.c.}$ is reached, to fix initial conditions for the perturbations.

3. Integrate the background and the perturbation dynamics simultaneously from $N^t_{\rm i.c.}$ to $N^t_{\rm end}$ for each comoving mode.

4. Determinate the scalar power spectrum, $\mathcal{P}_\zeta(k) = 1/(2\pi^2)\sum_i |\zeta_i|^2$, where $i = 1...n$ corresponds to the n independent initial conditions for the field perturbations $\delta\phi_i$ and ζ_i being the induced contributions to the curvature perturbation ζ.

3.4 Inflation along waterfall trajectories

Until now, the discussions in this chapter are valid for all multifield inflation models. In this section, we focus on the hybrid models with a mild waterfall phase which lasts for more than 60 e-folds. The mild waterfall dynamics has been investigated for the original model in Ref. [50, 51] and for the F-term and D-term models in Ref. [52]. In this section, we rederive the dynamics for the unified potential of Eq. (2.15) in the mild waterfall regime. Following the analytic description in Ref. [51], we parametrize the filed as

$$\phi \equiv \phi_{\rm c} {\rm e}^{\xi} \,, \qquad \psi \equiv \psi_0 {\rm e}^{\chi} \,, \tag{3.31}$$

where ψ_0 is the initial condition for the waterfall field at the critical point of instability. In the slow-roll waterfall scenarios, the conditions $\xi < 0$ and $|\xi| \ll 1$ must be satisfied. Furthermore, the field evolution below the critical point can be divided into three phases [51]:

- Phase 0: the second term of Eq. (2.16b) and the first term of Eq. (2.16a) are dominant.
- Phase 1: the first term of Eq. (2.16b) and the first term of Eq. (2.16a) are dominant.
- Phase 2: the first term of Eq. (2.16b) and the second term of Eq. (2.16a) are dominant.

Classically, the duration of the phase 0 is tiny [51]. Moreover, in a quantum scenario, in the vicinity of the critical point of instability, the quantum diffusion of the waterfall field dominates over the classical dynamics. Therefore, the phase 0 is not needed to be taken into account.

3.4.1 Phase 1

The field trajectories in phase 1 is determined from the slow-roll equations which can be written as

$$\xi^2 = \frac{pM^2\phi_{\rm c}^{p-2}}{4\mu^p}(\chi - \chi_i) \tag{3.32}$$

Then the connection point (ξ_2, χ_2) between phase 1 and 2 is

$$\chi_2 \equiv \ln\left(\frac{\sqrt{p}\phi_{\rm c}^{\frac{p}{2}}M}{2\mu^{p/2}\psi_{\rm i}}\right) \ . \tag{3.33}$$

The duration of phase 1 is given by integrating

$$\frac{{\rm d}\xi}{{\rm d}N^t} \simeq -\frac{p\phi_{\rm c}^{p-2}M_{\rm pl}^2}{\mu^p} \, . \tag{3.34}$$

If the e-fold time is set to be zero at the critical instability point, one obtains

$$\xi = -\frac{pM_{\rm pl}^2\phi_{\rm c}^{p-2}}{\mu^p}N^t \, . \tag{3.35}$$

However, we note that there is a temporal minimum for the potential that is an ellipse corresponding $\partial V/\partial\psi = 0$. It is located on the trajectories

$$\xi = -\frac{\psi_{\rm i}^2{\rm e}^{2\chi}}{2M^2} \ . \tag{3.36}$$

Provided

$$\chi_2 < \frac{p\phi_{\rm c}^{p+2}}{16\mu^p M^2}, \tag{3.37}$$

, the temporal minimum is reached in the phase 1. One therefore obtains

$$\xi_2 \equiv \begin{cases} -\dfrac{\sqrt{p}\phi_{\rm c}^{\frac{p}{2}-1}M}{2\mu^{p/2}}\sqrt{\chi}_2 & \text{for} \quad \chi_2 > \dfrac{p\phi_{\rm c}^{p+2}}{16\mu^p M^2} \\ -\dfrac{p\phi_{\rm c}^p}{8\mu^p} & \text{for} \quad \chi_2 < \dfrac{p\phi_{\rm c}^{p+2}}{16\mu^p M^2} \end{cases} \ . \tag{3.38}$$

The number of e-folds N_1 realized in phase 1 then is given by

$$N_1 = \begin{cases} \dfrac{\sqrt{\chi_2}\mu^{p/2}M}{2\sqrt{p}\phi_{\rm c}^{\frac{p}{2}-1}M_{\rm pl}^2} & \text{for} \quad \chi_2 > \dfrac{p\phi_{\rm c}^{p+2}}{16\mu^p M^2} \\ \dfrac{\phi_{\rm c}^2}{8M_{\rm pl}^2} & \text{for} \quad \chi_2 < \dfrac{p\phi_{\rm c}^{p+2}}{16\mu^p M^2} \end{cases} \ . \tag{3.39}$$

3.4.2 Phase 2

Solving the slow-roll equations, we find that the field trajectories in phase 2 follow the relation

$$\xi^2 = \xi_2^2 + \frac{pM^2\phi_{\rm c}^{p-2}}{8\mu^p}\left[{\rm e}^{2(\chi-\chi_2)} - 1\right] \ . \tag{3.40}$$

The temporal minimum is reached when

$$\xi = \xi_{\rm 2T.M.} \equiv -\frac{M^2}{2\phi_{\rm c}^2} - \sqrt{\frac{M^4}{4\phi_{\rm c}^4} + \xi_2^2 - \frac{p\phi_{\rm c}^p}{8\mu^p}} \, . \tag{3.41}$$

If the slow-roll conditions violated when

$$\eta_{\psi\psi} \simeq \frac{8M_{\rm pl}^2\xi}{M^2} \simeq -1 \ , \tag{3.42}$$

the inflation ends before reaching the temporal minimum. In contrast, if the slow-roll conditions violated when

$$\eta_{\phi\phi} \simeq \frac{4M_{\rm pl}^2\psi^2}{\phi_{\rm c}^2 M^2} \simeq 1 \, , \tag{3.43}$$

fields evolve through the temporal minimum before the end of inflation. By using Eq. (3.36), one thus finds that

$$\xi_{\rm end} = \begin{cases} -\dfrac{\phi_{\rm c}^2}{8M_{\rm pl}^2} & \text{for} \quad |\xi_{\rm end}| > |\xi_{\rm 2T.M.}| \\ -\dfrac{M^2}{8M_{\rm pl}^2} & \text{for} \quad |\xi_{\rm end}| < |\xi_{\rm 2T.M.}| \end{cases} . \tag{3.44}$$

Assuming that $\xi \ll 1$ and $\chi_2 > 1/2$, the slow-roll equations can be solved exactly in phase 2 before reaching the temporal minimum. Then, one obtains [51]

$$\xi(N^t) = c' \sqrt{\frac{pM^2}{2\phi_{\rm c}^{p-2}\mu^p}} \frac{(c'-c)f(N^t) - c' - c}{(c'-c)f(N^t) + c' + c} \, , \tag{3.45}$$

where $c \equiv \sqrt{\chi_2/2}$, $c' \equiv \sqrt{c^2 - 1/4}$ and

$$f(N^t) = \exp\left[\frac{8\sqrt{2}c' p \phi_{\rm c}^{\frac{p}{2}-1} M_{\rm pl}^2 (N^t - N_1)}{\sqrt{p\mu^p M^2}} \right] \ . \tag{3.46}$$

In the limit $|\xi| \gg |\xi_2|$, one can obtain

$$\frac{1}{\xi} - \frac{1}{\xi_{\rm end}} = \frac{8M_{\rm pl}^2}{M^2}(N^t - N_{\rm end}^t) \ . \tag{3.47}$$

By integrating

$$\frac{{\rm d}\xi}{{\rm d}N} = \frac{8M_{\rm pl}^2\xi}{\phi_{\rm c}^2} \ , \tag{3.48}$$

one obtains the number of e-folds realized along the temporal minimum

$$N_{\rm end}^t - N_{\rm 2T.M.}^t = \frac{\phi_{\rm c}^2}{8M_{\rm pl}^2} \ln\left(\frac{\xi_{\rm end}}{\xi_{\rm 2T.M.}} \right) \ , \tag{3.49}$$

where $N_{\rm 2T.M.}^t$ is the value of the parameter N^t when $\xi = \xi_{\rm 2T.M.}$. Since the unified potential (2.15) is considered as an effective description that valid below the Planck scale, the fields ϕ and ψ should be sub-Planckian. Hence, the critical instability point must satisfy $\phi_{\rm c} \ll M_{\rm pl}$. From Eq. (3.49), we know that the number of e-folds realized after reaching the temporal minimum is very small.

Chapter 4

Non-Gaussianities from the mild waterfall phase

4.1 Analytical results

In this section, the level of non-Gaussianities is calculated by using the δN formalism. It is useful to denote the time of the beginning of the transition between the phases 1 and 2 occurs and the time of horizon exit of the pivot scale k_* by $t_{1,2}$ and t_* respectively. According to the relation between t_* and $t_{1,2}$, one can distinguish two different cases:

1. $t_* > t_{1,2}$, the pivot scale leaves the horizon in phase 2 (long waterfall phase with $N^t_{\rm end} - N^t_* \gg 60$),
2. $t_* < t_{1,2}$, horizon exit occurs in phase 1 (moderately long waterfall phase, with $N^t_{\rm end} - N^t_* \gtrsim 60$).

4.1.1 Case 1: Horizon exit in phase 2

To evaluate the $f_{\rm NL}$ parameter with the δN formalism, the first step is to compute the number of e-folds realized during inflation with an arbitrary starting point (ξ_i, χ_i) in field space. Then, we use this result to evaluate the quantities $N_{,\phi}$, $N_{,\psi}$, $N_{,\phi\phi}$, $N_{,\phi\psi}$ and $N_{,\psi\psi}$ for the pivot scale k_*. Here the unperturbed background fields is denoted by (ξ_*, χ_*).

If inflation ends before the temporal minimum is reached, the trajectories in phase 2 can be rewritten as

$$\psi^2 = \psi_0^2 e^{2\chi} = 2\phi_{\rm c}^2(\xi^2 - \xi_i^2) + \psi_0^2 {\rm e}^{2\chi_i} \,. \tag{4.1}$$

As $\xi \to \xi_{\rm end}$ and $\chi \to \chi_{\rm end}$, this equation also gives $\chi_{\rm end}$. In combination with the slow-roll equation for ϕ, one gets the number of e-folds realized when the fields evolve from (ξ_i, χ_i) to $(\xi_{\rm end}, \chi_{\rm end})$,

$$N^t_{\rm end} - N^t_i = -\frac{M^2}{8M_{\rm pl}^2} \int_{\xi_i}^{\xi_{\rm end}} \frac{{\rm d}\xi}{\xi^2 - \xi_i^2 + \frac{\psi_0 {\rm e}^{2\chi_i}}{2\phi_{\rm c}^2}} \,. \tag{4.2}$$

By defining $C \equiv -\xi_i^2 + \psi_0 {\rm e}^{2\chi_i}/(2\phi_{\rm c}^2)$, we obtain

$$N^t_{\rm end} - N^t_i = -\frac{M^2}{8M_{\rm pl}^2\sqrt{C}} \left[\arctan\left(\frac{\xi_{\rm end}}{\sqrt{C}}\right) - \arctan\left(\frac{\xi_i}{\sqrt{C}}\right) \right] \tag{4.3}$$

if $C > 0$, and

$$N^t_{\rm end} - N^t_i = -\frac{M^2}{8M_{\rm pl}^2\sqrt{C}} \left[{\rm arctanh}\left(\frac{\xi_{\rm end}}{\sqrt{C}}\right) - {\rm arctanh}\left(\frac{\xi_i}{\sqrt{C}}\right) \right] \tag{4.4}$$

if $C < 0$.

For a given initial value ψ_i, we now have the freedom in specifying ψ_0 and χ_i. In order to accordance with the parametrization (3.31), we choose $\psi_0^2 \exp(2\chi_i) = 2\phi_{\rm c}^2\chi_i^2$, such that consequently

$$\psi_0^2 {\rm e}^{2\chi} = 2\phi_{\rm c}^2\xi^2 \tag{4.5}$$

and

$$\xi_i = -\frac{M^2}{8M_{\rm pl}^2\left(N_{\rm end}^t - N_i^t - \frac{M^2}{8M_{\rm pl}^2\xi_{\rm end}}\right)} \,. \tag{4.6}$$

Note that above choice corresponds to taking $C \to 0$. In this limit, Eqs. (4.3) and (4.4) can be expanded in a Taylor series as

$$N_{\rm end}^t - N_i^t = \frac{M^2}{8M_{\rm pl}^2}\left(\frac{1}{\xi_{\rm end}} - \frac{1}{\xi_i} + \frac{|C|}{3\xi_i^3} - \frac{|C|}{3\xi_{\rm end}^3}\right) \,, \tag{4.7}$$

which is a consistent generalization of Eq. (3.47). With this expression, the e-fold derivatives can be calculated. Relabeling $(\xi_i, \chi_i) \to (\xi, \chi)$, one then finds

$$\begin{aligned} N_{,\phi} &= \frac{M^2}{8\phi_{\rm c}{\rm e}^{\xi}M_{\rm pl}^2}\left(\frac{1}{\xi^2} - \frac{2}{3\xi^2} + \frac{2\xi}{3\xi_{\rm end}^3}\right) \\ &\simeq \frac{M^2}{24\phi_{\rm c}M_{\rm pl}^2\xi^2} \end{aligned} \tag{4.8}$$

and

$$\begin{aligned} N_{,\psi} &= \frac{M^2}{8M_{\rm pl}^2}\left(\frac{\psi}{3\phi_{\rm c}^2\xi^3} - \frac{\psi}{3\phi_{\rm c}^2\xi_{\rm end}^3}\right) \\ &\simeq \frac{M^2\psi}{24\phi_{\rm c}^2M_{\rm pl}^2\xi^3} \,. \end{aligned} \tag{4.9}$$

In the last line of above equations, we assumed that $|\xi| < |\xi_{\rm end}|$ and thus $|\xi^3| \ll |\xi_{\rm end}^3|$. This relation is well satisfied when we eventually replace $\xi \to \xi_*$ in the present case. In addition, the second derivatives of the leading order are given by

$$N_{,\psi\psi} = \frac{M^2}{24\phi_{\rm c}^2M_{\rm pl}^2}\left(\frac{1}{\xi^3} - \frac{1}{\xi_{\rm end}^3}\right) \simeq \frac{M^2}{24\phi_{\rm c}^2M_{\rm pl}^2\xi^3} \,, \tag{4.10}$$

$$N_{,\phi\phi} \simeq \frac{4M^2}{24\phi_{\rm c}^2M_{\rm pl}^2\xi^3} \tag{4.11}$$

and

$$N_{,\phi\psi} = -\frac{M^2\psi_k}{8\phi_{\rm c}^3{\rm e}^{\xi}M_{\rm pl}^2\xi^3} \simeq \frac{3\sqrt{2}M^2}{24M_{\rm pl}^2\phi_{\rm c}^2\xi^3} \,. \tag{4.12}$$

According to the relation (4.5), we notice that

$$N_{,\phi} = -\frac{1}{\sqrt{2}}N_{,\psi} \,, \tag{4.13}$$

and

$$N_{,\phi\phi} = 4N_{,\psi\psi} \simeq \frac{4}{3\sqrt{2}} N_{,\phi\psi} \,. \tag{4.14}$$

Replacing (ξ, χ) by (ξ_*, χ_*) in the above derives, one can now obtain the local $f_{\rm NL}$ parameter at the pivot scale

$$f_{\rm NL} \simeq \frac{5}{18}\left(\frac{24M_{\rm pl}^2\xi_*}{M^2}\right) \simeq -\frac{5}{3(N_{\rm exit} - \frac{M^2}{8M_{\rm pl}^2\xi_{\rm end}})} \ll 1 \,. \tag{4.15}$$

where $N_{\rm exit} = N_{\rm end}^t - N_*^t$ denotes the e-fold time that inflation lasts after the horizon exit of the pivot scale. For the supersymmetric F-term and D-term models, the above expression reduces to

$$f_{\rm NL} \simeq -\frac{5}{3(N_{\rm exit}+1)} \,. \tag{4.16}$$

Typically $N_{\rm exit} \approx 60$ e-folds, the level of non-Gaussianities is therefore negative and very low, *e.g.* $f_{\rm NL} \approx -0.03$ for the F-term and D-term models.

Finally, there is still a situation, in which the temporal minimum for the field ψ is reached in phase 2, need to be considered. Then, we need to evaluate

$$N = N_*^{\rm T.M.} + N_{\rm T.M.}^{\rm end} \,, \tag{4.17}$$

where $N_*^{\rm T.M.}$ is the number of e-folds realised between t_* and the time when the temporal minimum is reached, and $N_{\rm T.M.}^{\rm end}$ is the e-fold time that fields evolve from the temporal minimum to the end of inflation. On the trajectory, that crosses the temporal minimum in phase 2 with an arbitrary initial condition, the value of ξ must satisfy

$$\xi_{\rm 2T.M.} = -\frac{M^2}{2\phi_{\rm c}^2} - \sqrt{\frac{M^4}{4\phi_{\rm c}^4} + \xi_i^2 + \psi_i^2/(2\phi_{\rm c}^2)}. \tag{4.18}$$

Then, one can take Eq. (4.7) and replace $\xi_{\rm end}$ by $\xi_{\rm 2T.M.}$ to calculate $N_{*,\phi}^{\rm T.M.}$. For the derivatives, we again replace $(\xi_i, \chi_i) \to (\xi, \chi)$ and notice that

$$\frac{{\rm d}\xi_{\rm 2T.M.}}{{\rm d}\xi} = \frac{-\xi}{\frac{M^2}{2\phi_{\rm c}^2} - \xi_{\rm 2T.M.}} \,. \tag{4.19}$$

An additional term $-({\rm d}\xi_{\rm 2T.M.}/{\rm d}\phi_i)/\xi_{\rm T.M.}^2$ arise in the parentheses of Eq. (4.8). However, compared to the leading term, it is negligible. With Eq. (3.49), one can obtain

$$N_{\rm T.M.,\phi}^{\rm end} = \frac{\phi_{\rm c}}{8M_{\rm pl}^2\xi_{\rm 2T.M.}}\frac{{\rm d}\xi_{\rm 2T.M.}}{{\rm d}\xi} = \frac{\phi_{\rm c}}{M_{\rm pl}^2}\mathcal{O}(\xi) \,. \tag{4.20}$$

Since $|\xi| < |\xi_{\rm end}| = \phi_{\rm c}^2/(8M_{\rm pl}^2)$, one finds that $N_{\rm T.M.,\phi}^{\rm end} \ll N_{*,\phi}^{\rm T.M.}$, as $\phi_{\rm c} \ll M_{\rm pl}$, which is required for the validation of the effective theory description.

Similarly, the leading terms in $N_{\rm T.M.,\psi}^{\rm end}$, $N_{\rm T.M.,\psi\psi}^{\rm end}$, $N_{\rm T.M.,\phi\psi}^{\rm end}$ and $N_{\rm T.M.,\phi,\phi}^{\rm end}$, as well as in $f_{\rm NL}$, are not modified when the temporal minimum is reached, except replacing $\xi_{\rm end}$ by $\xi_{\rm T.M.}$. Therefore, we conclude that the level of non-Gaussianities is reduced compared to the contributions from $N_*^{\rm T.M.}$ and impossible to increase up to an observable level.

4.1.2 Case 2: Horizon exit in phase 1

The same as the discussion for case 1, we first consider the situation where the temporal minimum is not reached. In the discussion of Sec. 3.4.1, we have fixed the initial value of ξ to zero. However, in order to obtain the necessary e-folds derivatives for the δN approach, we have to generalize our analysis for more general initial values ξ_i.

The slow-roll equations in phase 1 yield the trajectory

$$\xi^2 - \xi_i^2 = \frac{p\phi_c^{p-2} M^2 (\chi - \chi_i)}{4\mu^p} \,. \tag{4.21}$$

For the number of e-folds generated in phase 1, one has to integrate Eq. (3.34) from the initial point (ξ_i, χ_i) until reaching the onset of phase 2 (ξ_{2i}, χ_2), which gives

$$N_1 = N_2^t - N_i^t = -\frac{\mu^p (\xi_{2i} - \xi_i)}{p M_{\rm pl}^2 \phi_c^{p-2}} \,, \tag{4.22}$$

where $\xi_{2i} = -\sqrt{\xi_i^2 + p\phi_c^{p-2} M^2 (\chi_2 - \chi_i)/(4\mu^p)}$, N_i^t is the value of the parameter N^t at the initial point (ξ_i, χ_i), N_2^t its value at (ξ_{2i}, χ_2), and χ_2 is given by Eq. (3.33). Then the total number of e-folds is given by $N_1 + N_2$, where N_2 are the e-folds that realized in phase 2 before the violation of slow-roll. Here, we again drop the index i on the initial field values, *i.e.* $(\xi_i, \chi_i) \to (\xi, \chi)$ and $(\phi_i, \psi_i) \to (\phi, \psi)$. The e-fold first derivatives then can be written as

$$N_{,\phi} = \frac{1}{\phi_k} \left(N_{1,\xi} + N_{2,\xi} \right) \,, \tag{4.23}$$

$$N_{,\psi} = \frac{1}{\psi_k} \left(N_{1,\chi} + N_{2,\chi} \right) \,. \tag{4.24}$$

For Eq. (4.24), the first term yields

$$N_{1,\chi} = -\frac{\mu^p}{p\phi_c^{p-2} M_{\rm pl}^2} \frac{{\rm d}\xi_{2i}}{{\rm d}\chi} = \frac{M^2}{8 M_{\rm pl}^2 \xi_2} \,, \tag{4.25}$$

and the second term gives

$$N_{2,\chi} = -\frac{p\phi_c^{p-2} M^2}{16 \xi_2 \mu^p} \frac{{\rm d}N_2}{{\rm d}\xi_{2i}} \,. \tag{4.26}$$

The number of e-folds elapse in phase 2 is given by Eq. (4.7) with ξ_{2i} and χ_{2i} instead of ξ_i and χ_i. Then one obtains

$$\frac{{\rm d}N_2}{{\rm d}\xi_{2i}} = \frac{M^2}{8 M_{\rm pl}^2 \xi_{2i}^2} \left(1 - \frac{2}{3} + \frac{2\xi_{2i}^3}{3\xi_{\rm end}^3} \right) \simeq \frac{M^2}{24 M_{\rm pl}^2 \xi_{2i}^2} \,, \tag{4.27}$$

and thus

$$N_{2,\chi} = -\frac{p\phi_c^{p-2} M^4}{384 \xi_2^3 M_{\rm pl}^2 \mu^p} = -\frac{1}{12\chi_2} N_{1,\chi} \,. \tag{4.28}$$

The last expression is obtained by inserting the value of ξ_2 from Eq. (3.38). From Eq. (3.33)], one knows that χ_2 is a large logarithm. Hence, the contribution from phase 1 dominate in Eq. (4.24). Therefore, the term $N_{2,\chi}$ is negligible, such that

$$N_{,\psi} \simeq \frac{M^2}{8 M_{\rm pl}^2 \xi_2 \psi} \,. \tag{4.29}$$

Now let we turn to Eq. (4.23). The two derivatives can be written as

$$\frac{\mathrm{d}N_1}{\mathrm{d}\xi} = -\frac{\mu^p}{pM_{\rm pl}^2\phi_{\rm c}^{p-2}}\left(\frac{\xi}{\xi_2}-1\right) \tag{4.30}$$

and

$$\frac{\mathrm{d}N_2}{\mathrm{d}\xi} = \frac{\mathrm{d}N_2}{\mathrm{d}\xi_{2i}}\frac{\xi}{\xi_2} \approx \frac{M^2\xi}{24M_{\rm pl}^2\xi_2^3}\,, \tag{4.31}$$

respectively. From Eq. (3.38), we find that

$$\frac{\mathrm{d}N_1}{\mathrm{d}\xi} = 6\chi_2\left(\frac{\xi_2}{\xi}-1\right)\frac{\mathrm{d}N_2}{\mathrm{d}\xi}\,. \tag{4.32}$$

Again, the derivative term come from phase 2 can be neglected, and thus $N_{,\phi}$ reads

$$N_{,\phi} \simeq \frac{\mu^p}{pM_{\rm pl}^2\phi_{\rm c}^{p-1}}\,. \tag{4.33}$$

In addition, because $\psi_* \ll \psi_2$, we may use that $N_{,\phi} \ll N_{,\psi}$.

In a similarly way, one finds that terms from phase 1 dominate the second derivatives. Then one gets

$$\begin{aligned} N_{,\psi\psi} &= -\frac{M^2}{8M_{\rm pl}^2\xi_2\psi^2}\left(1+\frac{1}{2\chi_2}\right) \\ &\simeq -\frac{M^2}{8M_{\rm pl}^2\xi_2\psi^2} \simeq -\frac{1}{\psi}N_{,\psi}\,, \end{aligned} \tag{4.34}$$

$$N_{,\phi\psi} \simeq -\frac{M^2\xi}{8M_{\rm pl}^2\xi_2^3\phi_{\rm c}\psi} \simeq -\frac{1}{\xi_2^2\phi_{\rm c}}N_{,\psi}\,, \tag{4.35}$$

and

$$N_{,\phi\phi} = \frac{\mu^p}{pM_{\rm pl}^2\phi_{\rm c}^{p-2}\phi^2}\left(-1+\frac{\xi}{\xi_2}-\frac{1}{\xi_2}+\frac{\xi^2}{\xi_2^3}\right) \tag{4.36}$$

$$\simeq -\frac{\mu^p}{pM_{\rm pl}^2\phi_{\rm c}^{p-2}\xi_2\phi_{\rm c}^2}\,. \tag{4.37}$$

We know that the derivatives with respect to the inflaton field ϕ, as well as the contribution from the number of e-folds in phase 2, are negligible since $\psi_* \ll \psi_2$ and $\chi_2 > \mathcal{O}(1)$. Thus, the parameter $f_{\rm NL}$ can be written as

$$f_{\rm NL} \simeq -\frac{5}{6}\frac{N_{,\psi\psi}(N_{,\psi})^2}{(N_{,\psi})^4} \simeq \frac{20M_{\rm pl}^2\xi_2}{3M^2} \simeq -\frac{10\sqrt{p}M_{\rm pl}^2\phi_{\rm c}^{p/2-1}}{3M\mu^{p/2}}\sqrt{\chi_2}\,. \tag{4.38}$$

For the F-term model, this gives

$$|f_{\rm NL}| \simeq \frac{5\kappa\sqrt{\mathcal{N}}\sqrt{\log 2}M_{\rm pl}^2}{6\sqrt{2}\pi m^2}\sqrt{\chi}_2 \lesssim 0.13\sqrt{\chi_2}\,. \tag{4.39}$$

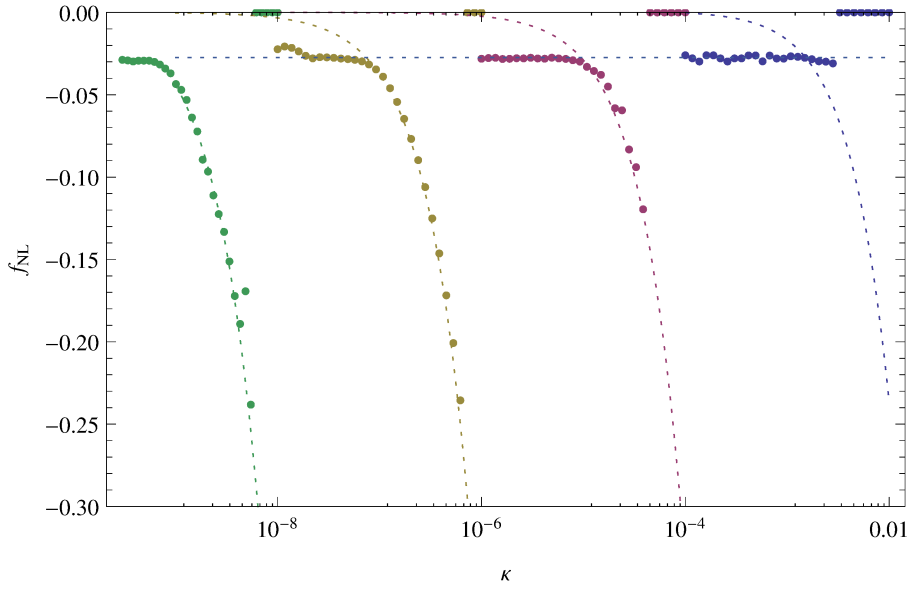

Figure 4.1: Non Gaussianity parameter $f_{\rm NL}$ as a function of κ, for the F-term model, with from left to right $m = 10^{-4}M_{\rm pl}$, $m = 10^{-3}M_{\rm pl}$, $m = 10^{-2}M_{\rm pl}$, $m = 10^{-1}M_{\rm pl}$. The bold dots are the numerical results using the δN formalism. The dotted horizontal line corresponds to $f_{\rm NL} = -5/[3(N_{\rm exit}+1)]$ [the approximate result from Eq. (4.38)] and the dashed lines to Eq. (4.38), which are respectively valid for $t_* > t_{1,2}$ and $t_* < t_{1,2}$. For simplicity, we take $N_{\rm exit} = 60$

If the duration of waterfall is just about 60 e-folds ($\kappa\sqrt{\mathcal{N}} \approx m^2/M_{\rm pl}^2$), the level of non-Gaussianity $|f_{\rm NL}|$ reaches its maximum [52]. Particle physics experiments give the upper bound $\sqrt{\chi_2} \lesssim 6$ by imposing a lower bound on m. Therefore, the absolute value of $f_{\rm NL}$ is never greater than about unity. It indicates that the level of non-Gaussianities is below the Planck sensitivity. In FIG. 4.1 the level of local non-Gaussianities given by Eqs. (4.38) and (4.15) are plotted as a function of κ for the F-term model with different values of m. Replacing m by $m_{\rm FI}$, one obtains the expression of $f_{\rm NL}$ for the D-term model, which is independent of the parameter g except logarithmically through the $\sqrt{\chi_2}$ factor.

For the original model, it requires at least 60 e-folds realized in the waterfall phase that imposes $M\mu \gtrsim 40M_{\rm pl}^2$ [50]. The parameter $f_{\rm NL}$ is independent of the model parameter Λ and $\phi_{\rm c}$ (apart through $\sqrt{\chi_2}$). Hence, the maximal value of $f_{\rm NL}$ is about 0.7, as for the F-term and D-term models. For original model, the level of non-Gaussianities from analytical approximations are given in TABLE 4.1 for various parameter sets, which cover the qualitatively different regimes. They are also compared to the numerical results. One may still worry about the case where the field trajectory reaches the temporal minimum in phase 1. From the relation (3.37), we find that in this case it requires $\chi_2 \ll 1$, where the quantum diffusion is dominating at the time t_*. Therefore, we conclude that this particular case is not relevant.

At this point, we can justify our choice of a final hypersurface of constant field value $\xi = \xi_{\rm end}$, instead of a surface of uniform density. Considering only the phase 2, $\psi_{\rm end}$ is

given by

$$\psi_{\rm end}^2 = 2\phi_{\rm c}^2\left(\xi_{\rm end}^2 - \xi_{\rm i}^2\right) + \psi_{\rm i}^2 \tag{4.40}$$

The shift $\Delta(\psi_{\rm end}^2)$ induced by perturbations of the fields at the time t_* can be derived with the δN formalism. For perturbations of the inflaton field, we obtain

$$\frac{\Delta(\psi_{\rm end}^2)}{\Delta\phi_*} = 4\phi_{\rm c}\xi_* \tag{4.41}$$

while perturbations of the waterfall field lead to

$$\frac{\Delta(\psi_{\rm end}^2)}{\Delta\psi_*} = 2\psi_* = 2\sqrt{2}\phi_{\rm c}\xi_* \tag{4.42}$$

At the end of inflation, the potential reads

$$V(\phi_{\rm end},\psi_{\rm end}) = \Lambda\left(1 + 2\xi_{\rm end}\frac{\psi_{\rm end}^2}{M^2}\right) . \tag{4.43}$$

In order to reach a surface of constant density, the shift in $\psi_{\rm end}$ should be compensated by a shift in $\xi_{\rm end}$, which reads

$$\frac{\Delta\xi_{\rm end}}{\Delta\phi_*} = \frac{8\phi_{\rm c}\xi_*}{M^2} . \tag{4.44}$$

$$\frac{\Delta\xi_{\rm end}}{\Delta\psi_*} = \frac{4\sqrt{2}\phi_{\rm c}\xi_*}{M^2} , \tag{4.45}$$

For $\xi_* \simeq -M^2/(8M_{\rm pl}^2 N_*)$, one obtains

$$\frac{\Delta\xi_{\rm end}}{\Delta\psi_*} = \frac{\sqrt{2}}{2}\frac{\Delta\xi_{\rm end}}{\Delta\phi_*} \ll 1 . \tag{4.46}$$

In the limit $|\xi_*| \gg |\xi_{\rm end}|$, we can safely neglect the shifts in Eqs. (4.8), (4.9), (4.10), (4.11) and (4.12) that caused by the different choices for the final hypersurface.

If the pivot scale exits the Hubble radius in phase 1, the shift of ξ_2^2 as $\Delta\xi_2^2 = -\Delta\xi_*^2$ and $\Delta\xi_2^2 = -p\phi_{\rm c}^{p-2}M^2\Delta\chi_*/(4\mu^p)$ for field perturbations can be calculated both in the longitudinal and transverse directions. By using $\Delta(\psi_{\rm end}^2) = -2\phi_{\rm c}^2\Delta\xi_2^2$ and then $\Delta\xi_{\rm end} = 2\Delta\psi_{\rm end}^2/M^2$, it is straightforward to show that

$$\frac{\Delta\xi_{\rm end}}{\Delta\psi_*} \ll 1, \qquad \frac{\Delta\xi_{\rm end}}{\Delta\phi_*} \ll 1 . \tag{4.47}$$

In the derivatives $N_{,\phi}$, $N_{,\psi}$, $N_{,\phi\phi}$, $N_{,\psi\psi}$ and $N_{,\phi\psi}$, the terms from the variation of the number of e-folds in phase 1 is dominant and again the shift in the terms from phase 2 can be neglected. Therefore, our results are independent of the possible choices for the final hypersurface.

4.2 Numerical analysis

The analytical calculations of the previous section are based on many approximations, namely,

1. the slow-roll approximation,

2. a sharp transition between phase 1 and phase 2,

3. the final hypersurface with a fixed field value $\xi = \xi_{\rm end}$ [according to Eq. (3.44)],

4. the Taylor expansion (4.7) of the number of e-folds in phase 2,

5. some terms neglected in the e-folds derivatives.

Thus, we need to check the validity and the accuracy of our results. For this purpose, a numerical calculation base on the δN formalism has been employed. Practically, the numerical integration is divided into four steps:

1. The exact multifield background dynamics is integrated from the critical instability point, where we set $N^t = 0$, until the end of inflation, such that the total number of e-folds $N^t_{\rm end}$ is obtained.

2. The background dynamics is integrated again from the critical point to the time of horizon exit of the pivot scale $k_* = 0.05{\rm Mpc}^{-1}$. Thus, the initial conditions for the perturbations are fixed at this time.

3. A numerical integration of the field dynamic is performed from initial conditions on a 3×3 grid of values centered on (ϕ_*, ψ_*) in order to determine the number of e-folds N to reach the final hypersurface.

4. The derivatives $N_{,i}$ and $N_{,ij}$ are calculated numerically. Then, the amplitude $\mathcal{P}_\zeta$ and the spectral tilt $n_{\rm s}$ of the power spectrum of curvature perturbations as well as the level of non-Gaussianities $f_{\rm NL}$ can be computed by using Eqs. (3.9), (3.10) and (3.13).

In order to maintain the stability of the code, the differences between the initial conditions need to be carefully chosen. It should be sufficiently small for the numerical derivatives $N_{,i}$ and $N_{,ij}$ to be accurate. However, at the same time, it should be sufficiently large to ensure that the differences between the values of N is much larger than the steps of integration (which cannot be lower than $\Delta N \sim 10^{-4}$ without increasing unreasonably time consuming).

In addition, it is particularly difficult to define the final hypersurface numerically. The reason is that along the waterfall trajectories the variation of the false vacuum potential is too tiny to be resolved under a limited numerical precision. Hence, we have considered the following alternatives:

- the hypersurface at the end of the slow-roll regime, where one of the slow-roll parameters reaches unity;

- a hypersurface of uniform energy just after the end of inflation, when for example $\rho_{\rm end} = 0.99\rho_{\rm inf}$ In this case, we assume that the effects of the tachyonic preheating are negligible, and the classical trajectories are valid down to the final hypersurface;

- a hypersurface of uniform potential energy density.

Between these possible methods, there is no noticeable difference.

In the vicinity of the critical point, the quantum diffusion of the waterfall field is dominant, and classical trajectories must be seen as emerging from this quantum stochastic regime. They are valid if the classical vev of the waterfall field satisfies $\psi \gg \sqrt{\langle \psi_{\rm qu}^2 \rangle}$, where $\psi_{\rm qu}$ is the operator for the quantum field fluctuations around the classical expectation value ψ. In the numerical integration, the value from the process of quantum diffusion [50, 52]

$$\psi_0 \simeq \frac{\sqrt{\kappa} M_{\rm F}^3}{2\sqrt{3}\pi^{3/4}(\ln 2)^{1/4}} \quad \text{for the F-term}\,, \tag{4.48}$$

$$\psi_0 \simeq \frac{g m_{\rm FI}^3}{8\sqrt{3\kappa}\pi^{3/4}(\ln 2)^{1/4}} \quad \text{for the D-term}\,, \tag{4.49}$$

$$\psi_0 \simeq \sqrt{\frac{\Lambda \mu M}{96\pi^{3/2}}} \quad \text{for the original model}\,, \tag{4.50}$$

has been taken as the initial condition of the waterfall field at the critical instability point. Moreover, we only consider the trajectory as valid when $\psi \gg \psi_0$. In practice, one can notice however that ψ_0 does not enter into the dominant term among the $N_{,i}$ and $N_{,ij}$ values (or only logarithmically), and thus its value does not change the generated level of non-Gaussianities and the power spectrum of curvature perturbations. This has been confirmed numerically by checking that the results are independent of ψ_0 as long as it does not vary by several orders of magnitudes.

We have plotted in FIG. 4.1 both numerical and analytical results of the level of non-Gaussianities as a function of κ for the term model with different values of m in the range $10^{-4} M_{\rm pl} < m < 0.1 M_{\rm pl}$. From this figure, we find that numerical and analytical results agree well in the regime $f_{\rm NL} < -0.03$ and $m \lesssim 0.01 M_{\rm pl}$. For larger values, in the regime $t_* < t_{1,2}$, since the e-fold derivatives with respect of the inflaton ϕ become important, our approximation given by Eq. (4.38) is not valid anymore and the $|f_{\rm NL}|$ parameter takes lower values. For the D-term model, where the parameter $f_{\rm NL}$ is nearly independent of the model parameter g, one can draw identical conclusions. Finally, for the original model, there are two additional dimensions for the parameter space. With our numerical method, it is very difficult to explore the parameter space entirely. However, we have made a comparison of numerical and analytical results for a few sets of parameters corresponding to the different regimes that is presented in TABLE 4.1. This confirms the agreement between the analytical approximations and the numerical results.

Parameters	Regime	$f_{\rm NL}^{\rm num}$	$f_{\rm NL}^{\rm app}$	$n_{\rm s}^{\rm num}$	$n_{\rm s}^{\rm app}$	$\mathcal{P}_\zeta^{\rm num}(k_*)$	$\mathcal{P}_\zeta^{\rm app}(k_*)$
$M=\phi_{\rm c}=0.01\ M_{\rm pl}, \mu=10^5\ M_{\rm pl}, \Lambda=10^{-20}\ M_{\rm pl}^4$	$t_{1,2}<t_*$	-0.030	-0.029	0.929	0.930	0.017	0.019
$M=\phi_{\rm c}=0.001\ M_{\rm pl}, \mu=10^6\ M_{\rm pl}, \Lambda=10^{-30}\ M_{\rm pl}^4$	$t_{1,2}<t_*$	-0.033	-0.033	0.921	0.921	1.1×10^{-6}	1.3×10^{-6}
$M=0.001\ M_{\rm pl}, \phi_{\rm c}=10^{-5}, \mu=10^6\ M_{\rm pl}, \Lambda=10^{-30}\ M_{\rm pl}^4$	$t_{1,2}<t_*$	-0.033	-0.032	0.921	0.921	0.0011	0.012
$M=0.01\ M_{\rm pl}, \phi_{\rm c}=0.1\ M_{\rm pl}, \mu=10^5\ M_{\rm pl}, \Lambda=10^{-20}\ M_{\rm pl}^4$	$t_{1,2}<t_*<t_{TM}$	-0.030	-0.030	0.929	0.929	1.8×10^{-4}	1.9×10^{-4}
$M=0.001\ M_{\rm pl}, \phi_{\rm c}=0.1\ M_{\rm pl}, \mu=10^6\ M_{\rm pl}, \Lambda=10^{-30}\ M_{\rm pl}^4$	$t_{1,2}<t_*<t_{TM}$	-0.033	-0.032	0.921	0.921	1.1×10^{-10}	1.3×10^{-10}
$M=\phi_{\rm c}=0.01\ M_{\rm pl}, \mu=10^4\ M_{\rm pl}, \Lambda=10^{-20}\ M_{\rm pl}^4$	$t_*<t_{1,2}$	-0.10	-0.11	0.881	0.880	0.23	0.29
$M=\phi_{\rm c}=0.01\ M_{\rm pl}, \mu=10^{3.8}\ M_{\rm pl}, \Lambda=10^{-20}\ M_{\rm pl}^4$	$t_*<t_{1,2}$	-0.17	-0.18	0.946	0.955	1.2	1.36
$M=\phi_{\rm c}=0.001\ M_{\rm pl}, \mu=10^5\ M_{\rm pl}, \Lambda=10^{-30}\ M_{\rm pl}^4$	$t_*<t_{1,2}$	-0.14	-0.15	0.78	0.77	2.9×10^{-4}	4.6×10^{-4}
$M=\phi_{\rm c}=0.001\ M_{\rm pl}, \mu=10^{4.8}\ M_{\rm pl}, \Lambda=10^{-30}\ M_{\rm pl}^4$	$t_*<t_{1,2}$	-0.23	-0.24	0.77	0.77	0.021	0.035
$M=0.001\ M_{\rm pl}, \phi_{\rm c}=10^{-4}M_{\rm pl}, \mu=10^5 M_{\rm pl}, \Lambda=10^{-30}M_{\rm pl}^4$	$t_*<t_{1,2}$	-0.12	-0.13	0.82	0.81	6.1×10^{-3}	8.4×10^{-3}
$M=0.001\ M_{\rm pl}, \phi_{\rm c}=10^{-4}M_{\rm pl}, \mu=10^{4.8}M_{\rm pl}, \Lambda=10^{-30}M_{\rm pl}^4$	$t_*<t_{1,2}$	-0.20	-0.21	0.83	0.84	0.15	0.21

Table 4.1: Comparison of the power spectrum, the spectral index and the non-Gaussianities for various parameter sets, corresponding the horizon exit of the observable scales during the qualitatively different phases in the original model. The numerical results are obtained with the δN formalism by assuming instantaneous reheating.

Chapter 5

Power spectrum of curvature perturbations

5.1 Using the δN formalism

With Eqs. (3.9) and (3.10), one can calculate the amplitude and spectral tilt of the power spectrum of curvature perturbations. Besides the e-fold derivatives that have been calculated in the previous chapter, the field derivatives at the time t_* of horizon exit of the pivot scale are also needed for the calculation of the spectral index.

5.1.1 Case 1: Horizon exit in phase 2

In this case where $t_* > t_{1,2}$, we find

$$\frac{\mathrm{d}\phi}{\mathrm{d}N^t} = -\frac{8M_{\rm pl}^2\phi_{\rm c}\xi^2}{M^2} = -\frac{1}{3N_{,\phi}}\,, \tag{5.1}$$

$$\frac{\mathrm{d}\psi}{\mathrm{d}N^t} = \sqrt{2}\frac{8M_{\rm pl}^2\phi_{\rm c}\xi^2}{M^2} = -\frac{1}{3N_{,\psi}}\,. \tag{5.2}$$

Using Eq. (3.10), we obtain

$$n_{\rm s} - 1 \simeq \frac{32\xi_* M_{\rm pl}^2}{M^2} \simeq -\frac{4}{\left(N_{\rm exit} - \frac{M^2}{8M_{\rm pl}^2\xi_{\rm end}}\right)}\,. \tag{5.3}$$

Here ϵ_* is neglected since it is tiny when observable scales exit the horizon near the critical instability point. Moreover, the amplitude of the power spectrum of curvature perturbations is given by

$$\mathcal{P}_\zeta(k_*) \simeq \frac{\Lambda M^4}{16\times 24^2\pi^2 M_{\rm pl}^6\phi_{\rm c}^2\xi_*^4} \simeq \frac{4\Lambda M_{\rm pl}^2(N_{\rm exit} - \frac{M^2}{8M_{\rm pl}^2\xi_{\rm end}})^4}{9\pi^2 M^2\phi_{\rm c}^2} \tag{5.4}$$

The expressions of n_s and $\mathcal{P}_\zeta(k_*)$ recover the results of Refs. [51, 52] in coarse picture where the waterfall trajectories are considered as effective single field. Therefore, the case, that horizon exit of the pivot scale occurs in phase 2, is effectively single field. For the F-term and D-term models, the power spectrum is red tilted. However, the spectral index is too small when compared to CMB observations. For the original model, there is a free parameter Λ. In principle, the value of spectral index can be increased up to $n_{\rm s} \simeq 0.94$ by increasing Λ. However, in this case, the energy scale of inflation is near the limit of the B-mode polarization search in the CMB. Moreover, for the case where the temporal minimum is reached before the end of inflation, our discussion is still valid and $\xi_{\rm end}$ can be replaced by $\xi_{2.\rm TM}$ in Eq. (5.3).

5.1.2 Case 2: Horizon exit in phase 1

In the case where $t_* < t_{1,2}$, one finds

$$\frac{\mathrm{d}\phi}{\mathrm{d}N^t} = -\frac{p\phi_{\mathrm{c}}^{p-1}M_{\mathrm{pl}}^2}{\mu^p} = -\frac{1}{N_{,\phi}}\,, \tag{5.5}$$

$$\frac{\mathrm{d}\psi}{\mathrm{d}N^t} = -\frac{8M_{\mathrm{pl}}^2\psi\xi}{M^2} = -\frac{\xi}{N_{,\psi}\xi_2}\,. \tag{5.6}$$

By neglecting the derivative with respect to ϕ, one obtains the dominant term for the spectral index,

$$n_{\mathrm{s}} - 1 \simeq \frac{16M_{\mathrm{pl}}^2\xi_*}{M^2}\,. \tag{5.7}$$

When $\xi_* \to \xi_2$, it connects continuously to the spectral index for $t_* > t_{1,2}$. In FIG 5.2, we have plotted the spectral index as a function of κ and different values of M for the F-term model. The value of spectral index first is lower than expected for effectively single field trajectories. The reason for this behavior is that $|\xi_2|$, and thus $|\xi_*|$, first increases with κ. Then it is creasing when the horizon exit occurs deeper in phase 1. When $\xi_* \to 0$, the spectral index increase up to the unit. Therefore, in this case, one can find a regime of parameter space where the value of spectral index is in accordance with CMB observations. Now, let we turn to the amplitude of the power spectrum which is given by

$$\mathcal{P}_\zeta(k_*) \simeq \frac{\Lambda M^2\mu^p}{192\pi^2 pM_{\mathrm{pl}}^6\phi_{\mathrm{c}}^{p-2}\chi_2\psi_*^2}\,. \tag{5.8}$$

In the limit $t_* \simeq t_{1,2}$, one can replace $\psi_* = \psi_0\exp(\chi_2)$, such that the amplitude reads

$$\mathcal{P}_\zeta(k_*, t_* \simeq t_{1,2}) \simeq \frac{\Lambda\mu^{2p}}{48\pi^2p^2M_{\mathrm{pl}}^6\phi_{\mathrm{c}}^{2p-2}\chi_2}\,, \tag{5.9}$$

and it is connected to the amplitude in Eq. (5.4) for $t_* > t_{1,2}$. As the horizon exit of the pivot scale occurs deeper in phase 1, the amplitude grows exponentially as

$$\mathcal{P}_\zeta(k_*) \times \exp\left[2\chi_2\left(1 - \frac{N_*^{t\,2}}{N_1^2}\right)\right]\,, \tag{5.10}$$

where N_1 is the number of e-folds that realized in phase 1 and N_t^* is the number of e-folds between the critical instability point and the horizon exit of the pivot scale k_*. Hence, in the limit $t_* \simeq 0$, the amplitude reaches it maximum,

$$\mathcal{P}_\zeta(t_* \simeq 0) \simeq \frac{\Lambda M^2\mu^p}{192\pi^2p^2M_{\mathrm{pl}}^6\phi_{\mathrm{c}}^{p-2}\chi_2\psi_0^2}\,, \tag{5.11}$$

which is typically larger than unity. It is important to note that one cannot modify the amplitude of the curvature power spectrum without changing its spectral index since ψ_* in Eq. 9.6 is related to ξ_* through the waterfall dynamics in phase 1. From previous discussions, we know that the value of ψ_0 is given by Eqs. (4.48), (4.49) or (4.50) from the

process of quantum diffusion, and χ_2 only depends logarithmically on the model parameters which is typically of order unity. In the case where horizon exit of observable modes in phase 1 and $N_{\rm end} \gtrsim 60$, *i.e.* for parameter values $\kappa \sim M^2/M_{\rm pl}^2$ or $M\mu \sim M_{\rm pl}^2$, the amplitude of curvature power spectrum is several orders of magnitude larger than CMB observations.

For the F-term model, the spectrum amplitude as a function of κ is plotted in FIG. 5.1 with different values of m. In combination with FIG. 5.2, it explicitly shows that the exponential growth of the amplitude prevents it to be in agreement with CMB observations when the spectral index is in the allowed range of CMB observations. As mentioned in the previous Chapter, the case, where the temporal minimum is reached in phase 1, is not relevant because of the quantum diffusion.

5.2 From the numerical integration of multifield perturbations

The numerical methods for multifield perturbations were explained in Sec. 3.3.2. In the numerical integration, we can follow the sub-horizon and super-horizon evolution of the fields along the waterfall trajectories. Furthermore, the contributions of the field to the rescaled adiabatic and entropic perturbations, which are respectively defined as [77]

$$\delta\pi_{\rm a} = \frac{\dot\phi\delta\phi}{\sqrt{\dot\phi^2+\dot\psi^2}} + \frac{\dot\psi\delta\psi}{\sqrt{\dot\phi^2+\dot\psi^2}}\,, \tag{5.12}$$

$$\delta\pi_{\rm e} = \frac{\dot\psi\delta\phi}{\sqrt{\dot\phi^2+\dot\psi^2}} + \frac{\dot\phi\delta\psi}{\sqrt{\dot\phi^2+\dot\psi^2}}\,. \tag{5.13}$$

can be identified. For the F-term model, the evolution of curvature, rescaled adiabatic and entropic perturbations are plotted in Figs. 5.3 and 5.4 for the case $t_* > t_{1,2}$ and $t_* < t_{1,2}$, respectively. Moreover, we find that the behaviors for the original and D-term models are similar to that for the F-term model. In the case $t_* > t_{1,2}$, the curvature perturbations freeze out after horizon exit as expected in effective single-field description. Besides, we also note that in the sub-horizon regime, the adiabatic perturbations produced by $\delta\phi$ with $\delta\psi$ initially set to zero are identical to the isocurvature perturbations produced by $\delta\psi$ with $\delta\phi$ initially set to zero, and vice versa. This equivalence is expected because of the independent evolution of the field perturbations with identical amplitudes in the sub-horizon regime and because

$$\delta\pi_{\rm a} = \cos\theta\delta\phi - \sin\theta\delta\psi\,, \tag{5.14}$$

$$\delta\pi_{\rm e} = \sin\theta\delta\phi + \cos\theta\delta\psi\,, \tag{5.15}$$

where θ is the angle between a tangent vector of the field trajectory and the $\phi = 0$ direction.

In the case $t_* < t_{1,2}$, super-horizon curvature perturbations are enhanced by entropic perturbations during phase 1 and then frozen out during phase 2. This is due to the strong enhancement of the amplitude of the power spectrum in Eq. (5.10) obtained within the δN formalism.

For comparison, we have added numerical results of the amplitude and the spectral index of the curvature power spectrum for the F-term model into Figs. 5.1 and 5.2 respectively, for the same parameters as the analytical approximations. In general, we find agreement between the different methods. Moreover, these plots show the violation of the prediction of curvature perturbations from the effectively single-field dynamics. For the D-term model, the results are very similar.

In TABLE 4.1, the power spectrum and spectral index have been compared in the original model for some parameter sets which correspond to the different regimes. In the case $t_* < t_{1,2}$, there is a high discrepancy (up to 40%) between the numerical and analytical results for the spectrum amplitude. Since we assume a sharp transition between phase 1 and 2 in the analytic approximation, the quantity $N_2^t - N_{\rm end}^t$ cannot be computed with a very good precision. However, a tiny modification of this quantity can cause a huge difference in the spectrum amplitude in phase 1. Therefore, such a substantial discrepancy is not relevant. In the regime where $t_* > t_{1,2}$, numerical and analytical results agree well.

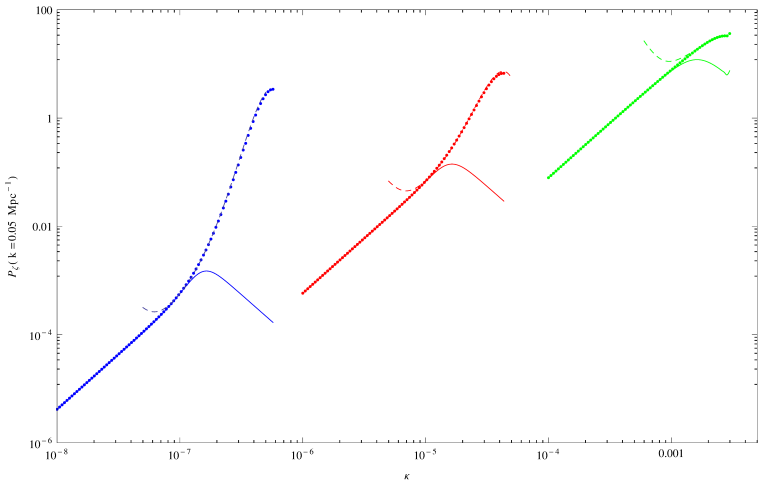

Figure 5.1: Spectrum amplitude of curvature perturbations derived from the analytic approximations based on the δN formalism (Hubble exit in phase 1: dashed), from the numerical integration (points), and assuming effectively single field trajectories (solid) as a function of the κ parameter for the F-term model, for a pivot scale $k_* = 0.05\text{Mpc}^{-1}$, and from left to right, $m = 10^{-3}/10^{-2}/10^{-1}$.

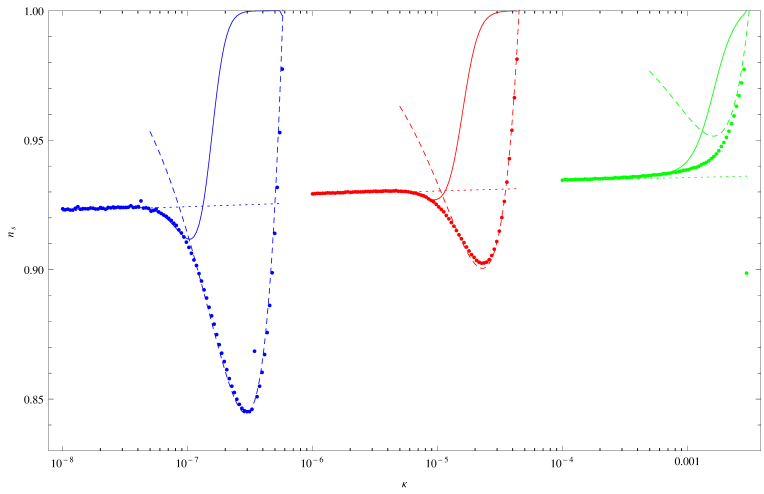

Figure 5.2: Spectral index of the power spectrum of curvature perturbations derived from the analytic approximations based on the δN formalism (Hubble exit in phase 1: dashed / phase 2: short dashed), derived from the numerical integration (points), and assuming effectively single field trajectories (solid), as a function of κ for the F-term model, for a pivot scale $k_* = 0.05\text{Mpc}^{-1}$, and from left to right, $m = 10^{-3}/10^{-2}/10^{-1}$.

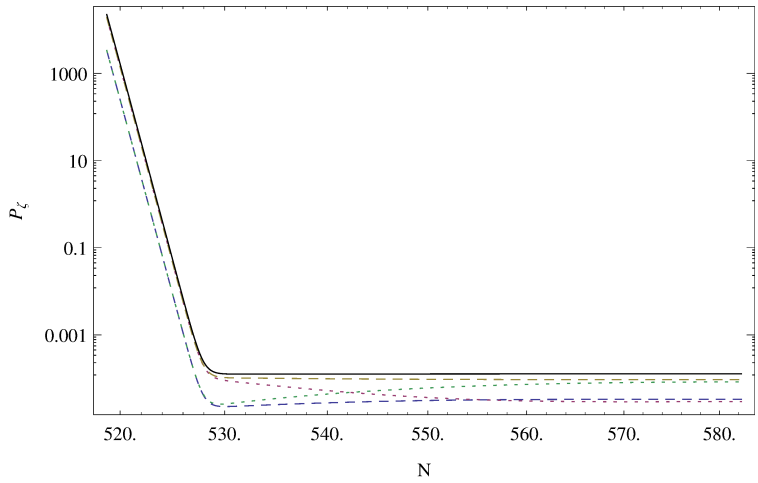

Figure 5.3: Evolution of the power spectrum of curvature perturbations (black) as well as of rescaled adiabatic (dashed) and entropic (dotted) perturbations, generated respectively by initial perturbations of ϕ (blue and red curves) and ψ (green and yellow curves), and the power spectrum of curvature perturbations (black curve) for a pivot scale $k_* = 0.05\text{Mpc}^{-1}$ and F-term model with parameters $m = 10^{-3}$ and $\kappa = 5 \times 10^{-8}$ which correspond to the case $t_* > t_{1,2}$.

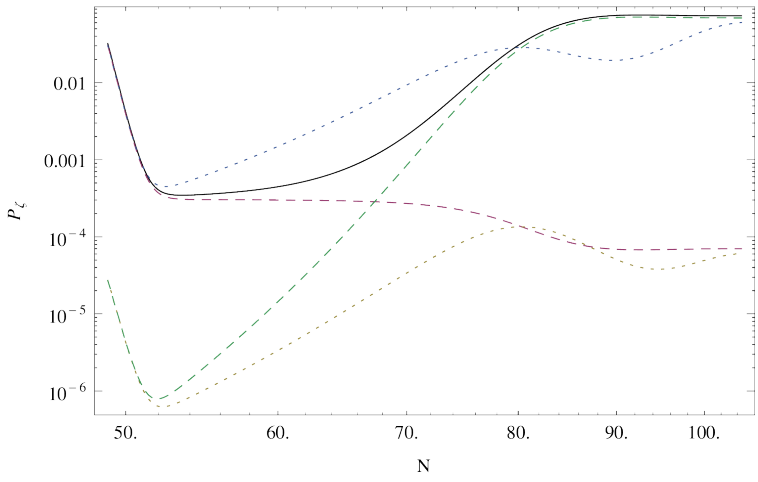

Figure 5.4: Evolution of the power spectrum of curvature perturbations (black) as well as of rescaled adiabatic (dashed) and entropic (dotted) perturbations, sourced respectively by initial perturbations of ϕ (blue and red curves) and ψ (green and yellow curves), and the power spectrum of curvature perturbations (black curve) for a pivot scale $k_* = 0.05\text{Mpc}^{-1}$ and F-term model with parameters $m = 10^{-3}$ and $\kappa = 3 \times 10^{-7}$ which correspond to the case $t_* < t_{1,2}$.

Conclusion

In this part, we have evaluated the level of non-Gaussianities, as well as the amplitude and the tilt of the power spectrum of curvature perturbation, both analytically and numerically for the unified potential of hybrid inflation models in a mild waterfall phase. The unified potential (2.15), which is based on a common parametrization, characterizes the supersymmetric F-term and D-term hybrid models as well as the original model. For the F-term and D-term models, the mild waterfall phase can only occur in the weak coupling regime *i.e.* $\kappa \lesssim M^2/M_{\rm pl}^2$, whereas it happens when $\mu M > M_{\rm pl}^2$ for the original model. In order to provide effective field theory description is valid, we consider only the sub-Planckian field case. Duration of the mild waterfall phase is required to be more than 60 e-folds, such that possible cosmological defects are stretched outside the observable universe. In our discussion, we have distinguished two different cases. The first case is that the horizon exit of observable modes occurs in phase 2 where the waterfall terms dominate the slope of the potential in the valley direction ($t_* > t_{1,2}$). In the second case, this horizon-crossing happens in the phase 1 where the slope of the inflationary valley dominates ($t_* < t_{1,2}$).

In the generic case 1 ($t_* > t_{1,2}$), we find that the effective single-field description is valid for all models. The level of non-Gaussianities is nearly independent of the model parameters with $f_{\rm NL} \approx -5/(3(N_{\rm exit}+1)) \approx -0.03$. Moreover, for the amplitudes and the spectral index of curvature power spectrum, we find agreement with the results of Refs. [50, 51, 52]. Note that the spectral index $n_{\rm s} = 1 - 4/N_{\rm exit}$ is typically outside and below the bounds imposed by CMB observations. Therefore, this regime is strongly disfavored.

In the case 2 where the model parameters are tuned such that $t_* < t_{1,2}$, the effective single-field description is no longer valid. We find that the absolute value of local $f_{\rm NL}$ can increase up to unity that is in the allowed regime from the Planck experiments. However, due to the effects of entropic modes, the power spectrum of curvature perturbations is strongly enhanced by several orders of magnitude up to a maximal amplitude larger than unity. This enhanced curvature power spectrum cannot satisfy the constraints of CMB observation and the upper bound of primordial black hole formation at the same time. Contrary to what was thought before [50, 51, 52], it is therefore impossible to find parameters in agreement with CMB observations.

Part II

Testing inflation and curvaton scenarios with CMB distortions

Contents

Introduction

Observations of CMB anisotropies have been dramatically improved in angular resolution and sensitivity over two decades. The observed power spectrum of curvature perturbations is nearly Gaussian and scale-invariant in consistent with the generic prediction of inflation models [19, 20]. The most recent Planck observation [78] have measured the CMB angular power spectrum up to the lowest multipole, whereas the Atacama Cosmology Telescope [79], and the South Pole Telescope [80] observe smaller scales up to multipoles $l = l_{\rm max} \sim 3000$. This range of angular scales corresponds to the k-modes of density perturbations $k_{l\rm max} = 2 \times 10^{-4}{\rm Mpc}^{-1} \lesssim k \lesssim 0.2{\rm Mpc}^{-1} = k_{l\rm min}$, which is about $7 \approx \ln k_{\ell\rm max}/k_{\ell\rm min}$ e-folds of expansion in the context of inflation. The modes of larger scales are still super-horizon, while the smaller scale modes are highly suppressed due to the Silk damping. Therefore, both earlier and later periods of the inflationary epoch remain inaccessible to observations.

In order to explore the physics of small-scales for the inflationary epoch, other signals and observational techniques must be envisaged. One example is the 21cm angular power spectra from the dark age and the subsequent reionisation (see e.g [81, 82, 83, 84]). Another is the distortions of the CMB black-body radiation which is less futuristic and potentially interesting. Spectral distortions can be induced by energy injection into the CMB photons through several processes [85, 86, 87], such as the dissipation of primordial acoustic modes, the decay or the annihilation of relic particles, the evaporation of primordial black holes, recombination radiations, the interaction of CMB photons with ordinary matter after recombination [85] and structure formation. Future CMB distortion experiments are plausible to probe modes in the range $8 \lesssim k \lesssim 10^4{\rm Mpc}^{-1}$. This means that the epoch of inflation is accessible to observations up to 17 e-folds.

In general, any perturbations in the primeval plasma during the tightly coupled regime and towards its end can generate spectral distortions of CMB. However, at very early time (redshifts $z \gtrsim 2 \times 10^6$), distortions are completely erased by thermalization which is very efficient. Fortunately, spectral distortions generated at lower redshifts may survive and still be observable today. Usually, CMB spectral distortions are classified as two types: μ-distortions and y-distortions. The μ-distortions are characterized by a frequency-dependent chemical potential $\mu(\nu)$, whereas y-distortions are characterised respectively by a reduction/increase of the intensity at low/high frequencies that mostly associated with SZ clusters. Moreover, μ-distortions dominate until $z \approx 2 \times 10^5$, while y-distortions dominate at redshifts $z \lesssim 1.5 \times 10^4$. At the intermediate regime $1.5 \times 10^4 \lesssim z \lesssim 2 \times 10^5$, there is a phase of the so-called Comptonized intermediate i-distortions where μ- and y-distortions are mixed [88, 89]. From the COBE-FIRAS experiment, the upper bound for μ- and y-distortions are $y < 1.5 \times 10^{-5}$ and $\mu < 9 \times 10^{-5}$ in 95% C.L.. Recently, the next generation experiment, Primordial Inflation Explorer (PIXIE) [53], has been proposed to improve these limits by approximately three orders of magnitude. Besides, the sensitivity to spectral distortions can be still improved by one order of magnitude compared to PIXIE in the next-to-next generation of experiments, such as the Polarized Radiation Imaging

and Spectroscopy Mission (PRISM) [54, 55].

To forecast possible constraints on the power spectrum of curvature perturbations with its amplitude and spectral index as well as the running of spectral index, some progresses have been made recently for various experimental configurations [89, 90, 91]. It shows that if the value of spectral index can be extended to scales probed by CMB distortions, the PIXIE experiments of CMB distortions cannot reach the sensitivity to improve current constraints. However, it is still unclear whether new constraints will arise for specific models with enhanced power spectrum at the distortion scales. In addition, curvaton scenarios, where a curvaton field can induce the curvature perturbations as well as inflaton, has also not yet been studied.

In this part, we are interested in the dissipation of primordial acoustic waves due to Silk damping. In this case the energy in sound waves is dissipated into the CMB monopole, which generates specific distortions of the CMB black-body spectrum [89, 90, 91, 92, 93]. Such distortions in principle reveal some information about primordial curvature perturbations at the scale much smaller than that of CMB anisotropy experiments. Moreover, we adopt a model-orient approach evaluating the level of CMB distortions by the modified `idistort` template [88] and performing Markov-Chain-Monte-Carlo (MCMC) parameter estimation by the `Greens` package [94]. We introduce the different types of CMB distortions and the expected sensitivity of the PIXIE and of PRISM-class experiments respectively in Chapter 6 and 7. Then, we have examined all 49 single-field inflation models listed in Ref. [27] and find out the models that predict an enhanced power spectrum at small scales for certain parameter space. In Chapter 8, the level of CMB distortions are evaluated for each of these models. In Chapter 9, we study three effective scenarios of multifield inflation: softly turning, suddenly turning and mild waterfall trajectories. Besides, a specific curvaton model is investigated in Chapter 10. Finally, we summarize our findings in the Conclusion.

Chapter 6

μ-type, y-type and intermediate i-type CMB distortions

6.1 The thermal SZ effect

The thermal SZ effect [95] means the effect that CMB photons are Comptonized by very hot electrons in the deep gravitational well formed by clusters of galaxies. Typically, the temperature of electrons exceeds the temperature of photons by more than eight orders of magnitudes. This effect induces a y-type distortion to the CMB black-body radiation where the change in the intensity reads

$$\Delta I(\nu) = y \frac{x \mathrm{e}^x}{\mathrm{e}^x - 1} \left[\frac{x(\mathrm{e}^x + 1)}{\mathrm{e}^x - 1} - 4 \right] I_0(\nu) \,, \tag{6.1}$$

where $x \equiv h\nu/(k_B T_0)$, ν is the frequency, k_B, h the Boltzmann and Planck constants, T_0 is the CMB black-body temperature and $I_0(\nu)$ is its intensity. The key parameter y is given by the integral

$$y = \int \frac{k_B T_e n_e \sigma_T a^2 H}{m_e c^2} \mathrm{d}\eta \,, \tag{6.2}$$

where m_e, T_e and n_e are respectively the electron mass, temperature and number density, σ_T is the Thomson cross-section and η the conformal time. In common, due to y-distortions, the intensity of the CMB is reduced at frequencies where the Rayleigh-Jeans limit is valid and increased in the Wien part of the spectrum. Typical values of y for the thermal SZ effect in galaxy clusters are $y \sim 10^{-4}$. Note that y-distortions can also be induced by energy injection before the epoch of recombination, but the changes in the intensity should still have the form of Eq. (6.1).

6.2 Before recombination: distortions induced by energy release

Before the epoch of recombination, energy injection can break the thermal equilibrium for photons in the primeval plasma, even though electrons and ions remain in thermal equilibrium because of Coulomb collisions. There are four phases can be distinguished,

1. At $z \gtrsim 2 \times 10^6$: the efficiency of Compton scattering is enough to maintain thermal equilibrium between photons, electrons, and baryons. The injected energies are redistributed over the entire spectrum of photons. The Maxwellian distribution of electrons is also maintained by Compton scattering. The chemical potential is driven to zero by double Compton scattering and Bremsstrahlung. Hence, the distribution

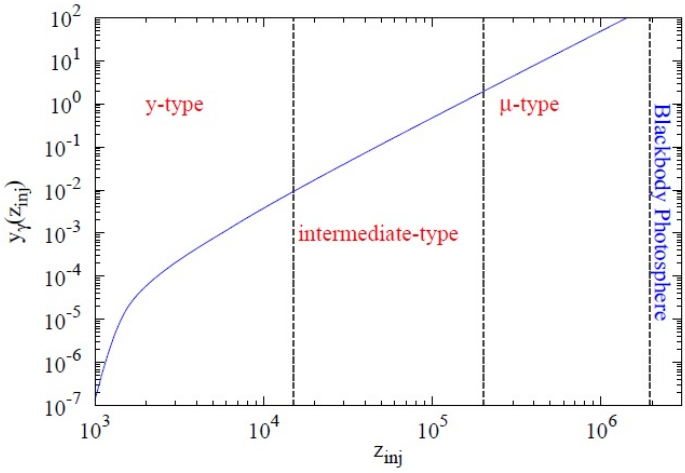

Figure 6.1: Compton parameter as a function of redshift, $y_\gamma(z_{inj})$. The dash lines are the boundaries of the different types of CMB distortions. Figure from [88]

of CMB photons is almost prefect black body even if in the presence of massive energy injection.

2. At $2 \times 10^5 \lesssim z \lesssim 2 \times 10^6$: double Compton scattering and Bremsstrahlung processes are inefficient in creating photons, whereas kinetic equilibrium is maintained by Compton scattering. If energy injected into the primeval plasma by some process, such as dissipating acoustic waves, evaporation of primordial black holes and decay/annihilation of relic particles, then the distribution of photons depart from the black body to a Bose-Einstein distribution with a chemical potential μ. This is the so-called μ-type distortions.

3. At $1.5 \times 10^4 \lesssim z \lesssim 2 \times 10^5$: kinetic equilibrium with photons can only be established partially by Compton scattering. If an energy injected, then the distortions induced in the CMB black body spectrum are of the intermediate $i-$type, where the CMB spectrum is Comptonized and not Bose-Einstein spectrum anymore.

4. At $z \lesssim 1.5 \times 10^4$: kinetic equilibrium cannot be established since the efficiency of Compton scattering is very low. In the presence of energy injection, deviations to the black body CMB spectrum would be in the form $y-$type distortions.

The relation of Compton parameter and different types of distortion is shown explicitly in FIG. 6.1. The various types of distortions can be employed to distinguish between models and energy injection processes. More detailed discussions can be found in Ref. [85] and other references.

6.3 Distortions from dissipating acoustic waves in the Silk-damping tail

After re-enter the particle horizon, density perturbations induce acoustic wave of ordinary matter. If the mean free path of photons is comparable to the acoustic wavelength, the tail of the CMB power spectrum will be damped by the diffusion of photons. This process is called as Silk damping (also known as photons diffusion damping). During the Silk damping, the energy initially stored within acoustic oscillations is dissipated into the CMB monopole.

Let we define the fractional dissipated energy $Q \equiv \Delta E/E$. In the tight coupling regime, the evolution of Q satisfies [93]

$$\frac{\mathrm{d}Q}{\mathrm{d}t} \simeq \frac{9}{4}\frac{\mathrm{d}(1/k_{\mathrm{D}}^2)}{\mathrm{d}z}\int \frac{\mathrm{d}k^3}{(2\pi)^3} k^2 P_i^{\gamma}(k)\mathrm{e}^{-k^2/k_{\mathrm{D}}^2}\,, \tag{6.3}$$

where $P_i^{\gamma}(k) \equiv 4P_{\zeta}(k)/(0.4R_{\nu}+1.5)$, $R_{\nu} = \rho_{\nu}/(\rho_{\nu}+\rho_{\gamma}) \simeq 0.4$, and k_{D} is the Silk damping scale. The dissipated energy Q depends on the power spectrum of curvature perturbations P_{ζ}. In order to compute the total modifications of the CMB spectrum induced by energy injection which is described by the function $Q(t)$, we employ the `idistort` template [88] to solve the Kompaneets equation numerically. In addition, a modified version of the `Greens` code [94] has been used for the estimation of standard power spectrum parameters with a MCMC method.

Chapter 7

Sensitivities of the PIXIE and PRISM-class experiments

In 2011, the PIXIE experiment [53] was proposed as an NASA Explorer class mission. One major scientific goal to constrain the tensor-to-scalar ratio r to the order 10^{-3} by measuring the B-mode polarization of the CMB on large angular scales. Another important objective is to probe the spectral distortion of the CMB black body spectrum. The PIXIE will map the absolute intensity and the linear polarization of the CMB, as well as measure its absolute frequency spectrum in 400 spectral channels from 30 GHz to 6 THz. The instrument sensitivity to the unpolarized signal in each frequency bin will be

$$\delta I_\nu^{\rm PIXIE} = 5 \times 10^{-26} {\rm Wm}^{-2}{\rm Sr}^{-1}{\rm Hz}^{-1} \ , \tag{7.1}$$

which will allow a detection of distortions characterized by [53]

$$\mu = 5 \times 10^{-8} \ \text{ and } \ y = 1 \times 10^{-8} \ \text{ at } \ 5\sigma \, . \tag{7.2}$$

Typically, spectral distortions due to reionsation and structure formation have a maximum $\delta I_\nu = 10^{-23}{\rm Wm}^{-2}{\rm Sr}^{-1}{\rm Hz}^{-1}$, single-field slow-roll models with no running $\delta I_\nu \sim 10^{-25}{\rm Wm}^{-2}{\rm Sr}^{-1}{\rm Hz}^{-1}$, while recombination radiations predict that spectral distortions do not exceed $\delta I_\mu \sim 10^{-26}{\rm Wm}^{-2}{\rm Sr}^{-1}{\rm Hz}^{-1}$. In FIG 7.1, it shows some typical distortion spectra. From the figure, one can find that distortions due to reionsation and structure formation vanish for frequencies close to $\nu \simeq 200$GHz. It is a window for the detection of distortion from inflation or from decaying particles.

For standard single field models with no significant running, the scalar power spectrum on distortion scales can be obtained by extrapolating that to CMB anisotropy scales. In this case, the distortions are not detectable by the PIXIE experiment. However, in Ref. [89], forecasts for the amplitude and spectral index of the scalar spectrum have been done with a Fisher matrix method at the pivot scale $k_{\rm d} = 42{\rm Mpc}^{-1}$, which lies in the middle of the range of perturbation modes that can be probed with CMB distortions. In order to estimate scalar power spectrum parameters at the same pivot scale, we have employed a Bayesian MCMC approach based on the `Greens` code [94] with the fiducial values are given by the best fit of Planck. Besides, we take the fiducial value of the CMB monopole temperature as $T_0 = 2.7263$K, and define the variation as $\Delta^* \equiv \Delta_T = (T - T_0)/T_0$. Then, we marginalize over Δ^*, as well as $y_{\rm re}$ which corresponds to the y-distortions generated during reionization and large scale structure formation. In FIG. 7.2, we have shown the marginalized posterior probabilities. Note that the strongly non-Gaussian shape of the likelihood in the plane $(A_{\rm s} - n_{\rm s})$, indicates that the Fisher matrix method is not reliable. For spectral index values close to unity around the scale $k_{\rm d}$,

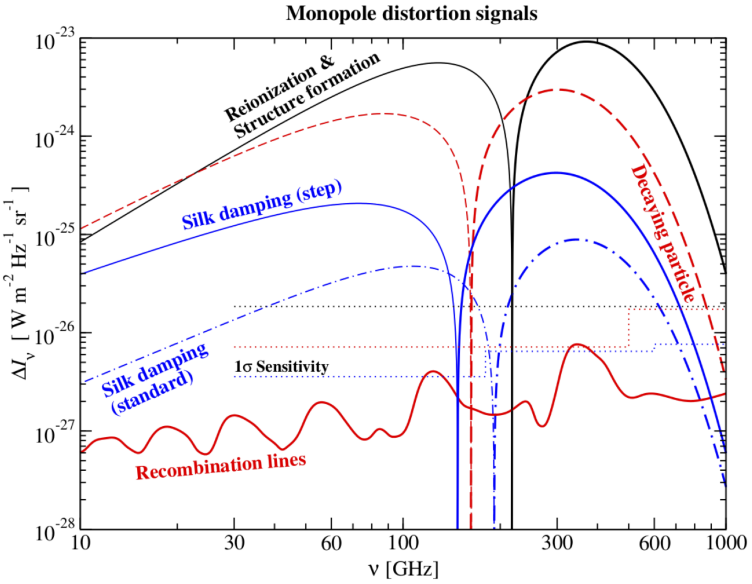

Figure 7.1: Spectral distortions induced by various sources and 1σ sensitivity for PRISM (dotted) for different designs. Figure from Ref. [54]

$1 < n_{\rm s} \lesssim 1.1$, we find that the lowest scalar power spectrum amplitude, that can be detected at 95 % C.L., is approximately

$$\mathcal{P}_\zeta(k_{\rm d} = 42\ {\rm Mpc}^{-1}) \approx 2.8 \times 10^{-9} \text{ for PIXIE}\,. \tag{7.3}$$

In addition, the Polarized Radiation Imaging and Spectroscopy Mission (PRISM) [54, 55] has been proposed in 2013 as an L-class ESA mission. Although it has been rejected, the best instrumental configuration PRISM still can be a good example of the possible ultimate next to next generation of CMB distortion experiment. The sensitivity of PRISM is of the order of ten times better than PIXIE

$$\delta I_\nu^{\rm PRISM} = 6.5 \times 10^{-27} {\rm Wm}^{-2}{\rm Sr}^{-1}{\rm Hz}^{-1} \tag{7.4}$$

for frequencies $\nu < 600$GHz which are the most relevant to CMB distortions. From FIG. 7.1, one find that the 1σ sensitivity of PRISM is close to the predicted signal from recombination lines. Therefore, it can measure the scalar power spectrum at distortion scales with a good accuracy. Moreover, it also improves the constraints on the spectral index running, which is defined as

$$n_{\rm run} = \frac{d\log n_s}{d\log k}\,, \tag{7.5}$$

to the order of 10^{-3} [96]. Nevertheless, the instrumental sensitivity of PRISM is not enough for the most general single field models of which the values of running are of second order in slow-roll parameters. By employing a MCMC analysis based on the package `Greens` [94], we illustrate a projection for the anomalously large running observation in FIG. 7.3, with the fiducial values $n_{\rm run} = 0$, $y_{\rm re} = 4 \times 10^{-7}$, $\Delta^* = 0$ and $\mathcal{P}_\zeta(k_{\rm p}) = 2.20 \pm 0.06 \times 10^{-9}$,

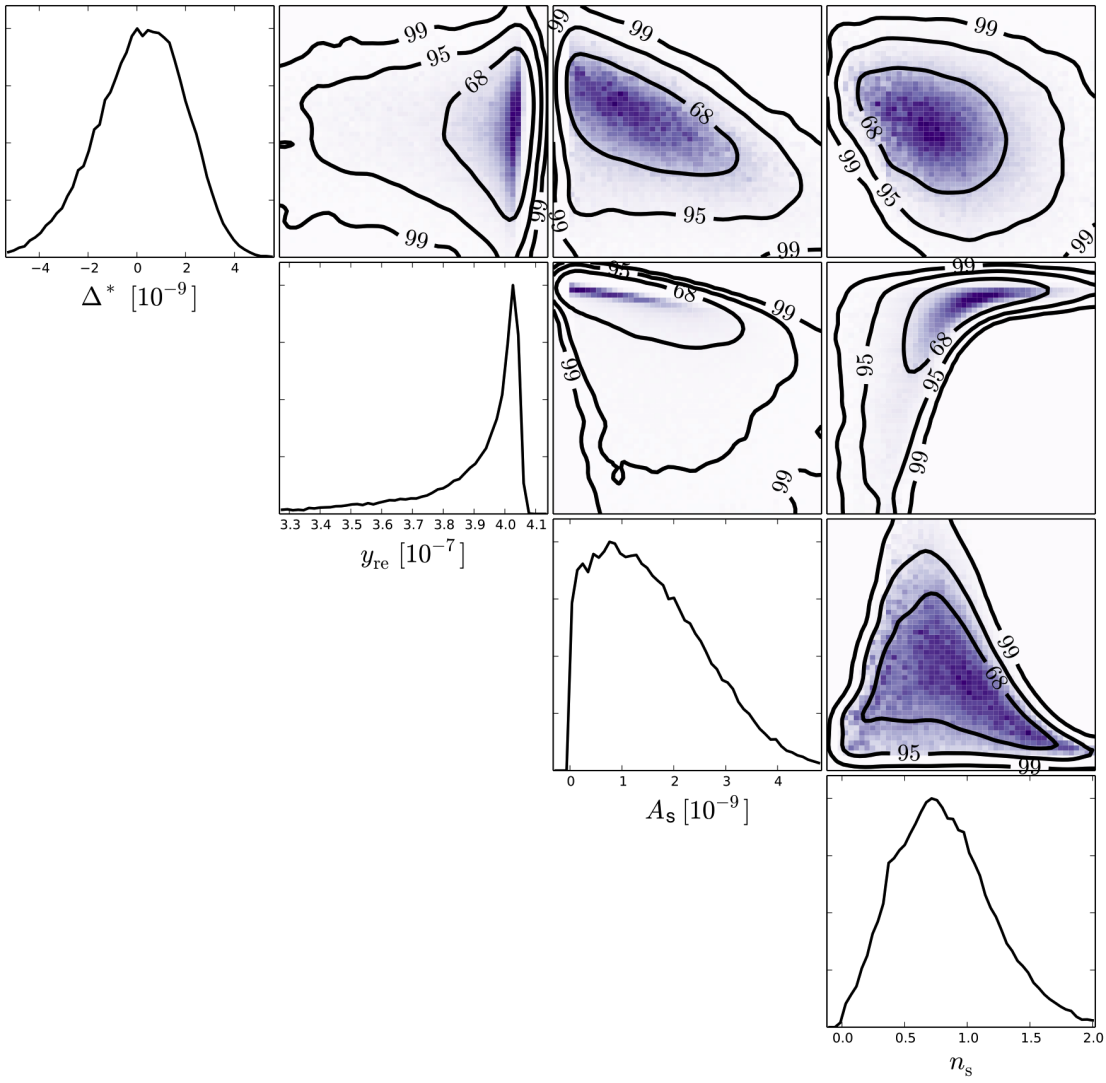

Figure 7.2: Forecast for the parameters $A_{\rm s}$, $n_{\rm s}$, $y_{\rm re}$ and Δ^* at $k_{\rm d} = 42$ Mpc^{-1}, for PIXIE configuration, using a MCMC sampling method with the `Greens` code [94]. The 1-D and 2-D posterior marginalized probability density distributions are illustrated in the figure, for a fiducial model given by the best fit of Planck, with no running, and $y_{\rm re}^{\rm fid} = 4 \times 10^{-7}$.

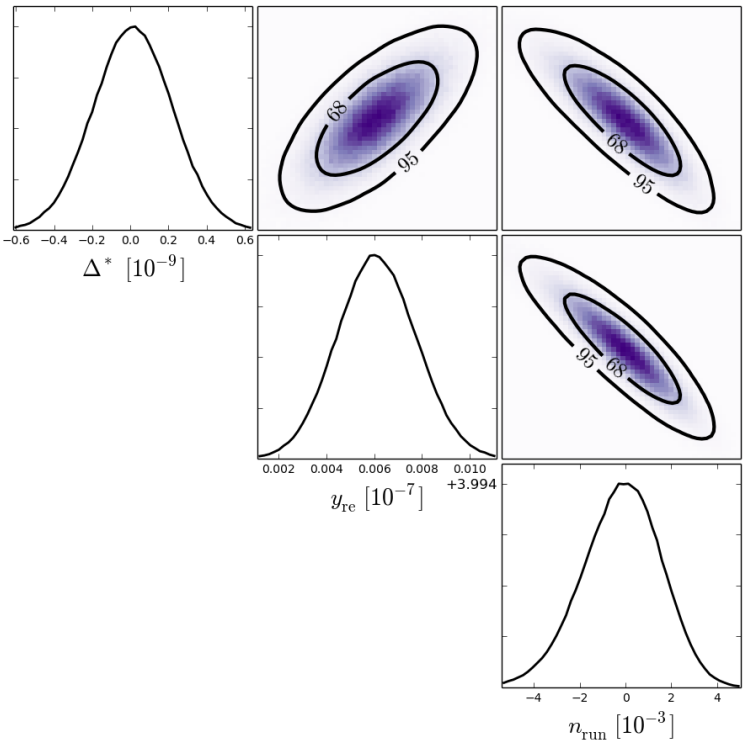

Figure 7.3: Projected exclusion bounds on $n_{\rm run}$ for a PRISM-class experiment which is ten times more sensitive than in Eq. (7.1).

$n_{\rm s}(k_{\rm p}) = 0.960 \pm 0.007$ at the CMB anisotropy pivot scale $k_{\rm p} = 0.05$ Mpc^{-1}. Then, we confirm that the instrumental sensitivity of a PRISM-class experiment can be ten time better than that of PIXIE, and $|n_{\rm run}| \gtrsim 4 \times 10^{-3}$ can be excluded at 95% C.L.

The next two chapters are dedicated to evaluating the level of CMB distortions for inflationary scenarios and to compare with the detectable limit given by Eq. (7.3). The possible detectability by an ultimate experiment like PRISM is also discussed.

Chapter 8

Testing single-field inflation with CMB distortions

In this chapter, we first build up three criteria for identifying single-field models that may induce an observable level of CMB distortions. With these criteria, we examine the 49 single-field models listed in Ref. [27] for all the possible regime, and find that only few of them may lead to CMB distortions at observable level by the proposed experiments. For each of these models, the regime of parameter space, which predict an increase in power for the curvature perturbation at the CMB scales, are found out. Then, the spectrum of μ-type and i-type distortions are evaluated for some relevant parameter sets with a modified version of the `idistort` code [88] and compared with the expected sensitivity of the PIXIE experiment. The y-type distortions are not interested, because one cannot distinguish the contribution from the pre-combination era to that from the SZ effect.

8.1 Criteria for observable CMB distortions

The single-field inflation scenario and its power spectrum of curvature perturbations are discussed in Sec. 1.2. The first and second slow-roll parameters are given by Eqs. (1.22) and (1.23) respectively. Here, we adopt a more accurate form of the spectral parameters (amplitude and spectral index) beyond slow-roll approximation but still at first order in slow-roll parameters. The spectrum amplitude reads [97]

$$\mathcal{P}_\zeta(k) = \frac{H_k^2}{8\pi^2 M_{\rm pl}^2 \epsilon_{1k}} \left[1 - 2(C+1)\epsilon_{1k} - C\epsilon_{2k}\right] , \tag{8.1}$$

and the spectral index

$$n_{\rm s}(k) = 1 - 2\epsilon_{1k} - \epsilon_{2k} , \tag{8.2}$$

where $C \equiv \gamma_{\rm E} + \ln 2 - 2 \simeq -0.7296$ and $\gamma_{\rm E}$ is the Euler-Mascheroni constant. The quantities with subscript k are evaluated at the time t_k of horizon exit of mode k, *i.e.* when $k = a(t_k)H(t_k)$.

At the anisotropy scales, the Planck results[20] strongly constrains the values of amplitude and spectral index of the power spectrum of curvature perturbations. At the pivot scale $k_{\rm p} = 0.05$ Mpc^{-1}, it gives

$$\mathcal{P}_\zeta(k_{\rm p}) = 2.20 \pm 0.06 \times 10^{-9}, \qquad n_{\rm s}(k_{\rm p}) = 0.960 \pm 0.007 . \tag{8.3}$$

As already mentioned, the CMB distortions experiments can look into a scale that much smaller then the anisotropy scales. However, due to the instrumental sensitivity, only if the amplitude of the power spectrum is enhanced at the distortion scales, the distortions

can be detected by the PIXIE experiment. Therefore, three necessary criteria can be imposed to inflation model to satisfy the Plank constraints and to induce an observable level of CMB distortions:

1. There exists a phase where $\epsilon_2 < -2\epsilon_1 < 0$: This condition ensures that the amplitude of power spectrum will be increased (*i.e.* a locally blue spectrum) at some scales. Broad classes of inflation models are ruled out by this restriction, such as Higgs inflation, natural inflation, exponential SUSY inflation, Logamediate inflation (for which $\epsilon_2 < 0$ is possible but with $\epsilon_2 \gtrsim -2\epsilon_1$ only).

2. A phase with $n_\mathrm{s} < 1$ must be followed by a stage with $n_\mathrm{s} > 1$: This condition ensures that the blue spectrum appears after the phase where the spectral index is in agreement with CMB anisotropy observation (*i.e.* the spectrum is red at the scale k_p). Hence, we can eliminate models where $n_\mathrm{s} > 1$ at all times, and models with blue spectrum only at scales that larger than the pivot scale k_p (e.g. Supergravity Brane inflation, Brane SUSY breaking inflation). In addition, to avoid external inflation (infinite or extremely large number of e-folds) phase at the inflection point ($n_\mathrm{s} = 0$), we imposes an additional criterion that $\epsilon_1 \neq 0$ (in other words, there is no point where the slope of the potential is vanishing) between these two phases. This criterion permits to eliminate MSSM Inflation and Inflection Point inflation models.

3. $n_\mathrm{s} = 0.960 \pm 0.007$ at $k_\mathrm{p} = 0.05\mathrm{Mpc}^{-1}$ and $n_\mathrm{s} > 1$ at $k_\mathrm{d} = 42\mathrm{Mpc}^{-1}$: This criterion is the most restrictive one. The first condition is inherited from the Planck constraints while the second one is a sufficient, but not necessary, condition for the enhancement of the power spectrum at CMB distortions scales. The pivot distortion scale $k_\mathrm{d} = 42\mathrm{Mpc}^{-1}$ lies in the middle of the range of modes that can be probed with CMB distortions. The choice to k_d is arbitrary. In principle, if $n_\mathrm{s} > 1$ on scales $k_\mathrm{p} < k < k_\mathrm{d}$, one can also obtain a sufficient increase of power on distortion scales. However, we did not find any single-field model in practice where the scalar power spectrum is enhanced only for scales within this range. Besides, there is no condition for the amplitude of the power spectrum at the pivot scale, since it can be adjusted by rescaling the potential without modifying the field evolution.

It is hard to apply the third criterion directly since it requires evaluating spectral parameters on the relevant scales by integrating field trajectories. Nevertheless, by imposing the first two criteria, most single-field models are excluded, and only five of them survive. They are

- Hybrid inflation in the valley (VHI)
- Generalized minimal supersymmetric model (GMSSM)
- Generalized renormalisable inflection point inflation (GRIPI)
- Running mass inflation (RMI)
- non-canonical Kähler inflation (NCKI)

In the following sections, we have a discussion to explore the parameter space of these models in detail and to evaluate the level of CMB distortions from them.

8.2 Hybrid inflation in the Valley (VHI)

The original hybrid model is already discussed in Sect. 2.1. Hybrid inflation in the valley refers to the inflationary phase that is driven by the inflaton as the waterfall field $\langle\psi\rangle = 0$. It ends at the critical point then the waterfall field triggers a tachyonic instability. This scenario can be described by the effective one-field potential (2.2) which is plotted in the top left panel of FIG. 8.1. By substituting the potential (2.2) into Eqs. (1.22) and (1.23), we obtain the slow-roll parameters

$$\epsilon_1 = \frac{2M_{\rm pl}^2 x^2}{\mu^2 \left(1+x^2\right)^2} \ , \tag{8.4a}$$

$$\epsilon_2 = \frac{4M_{\rm pl}^2 \left(-1+x^2\right)}{\mu^2 \left(1+x^2\right)^2} \ , \tag{8.4b}$$

where we have defined $x \equiv \phi/\mu_{\rm VHI}$. They are also plotted in FIG. 8.1 for various values of $\mu_{\rm VHI}$. In order to maintain the slow-roll dynamics, we consider only parameter values $\mu_{\rm VHI} \gtrsim 1.5 M_{\rm pl}$. Moreover, in order to induce a red spectrum at anisotropy scales and a blue spectrum on small scales, the regime of parameter space must be chosen carefully. Modes of CMB anisotropy scales exit the particle horizon close to the point where $\phi = \mu_{\rm VHI}$, at which $\epsilon_1 = \mathcal{O}(0.1)$ and $|\epsilon_2| < \epsilon_1$, such that a red spectrum of scalar perturbations is expected. A few e-folds later, it goes into the vacuum dominated regime where $\epsilon_1 \ll 1$ and $\epsilon_2 < 0$, and the spectral index turns to blue. The power spectrum of curvature perturbations is therefore enhanced on small scales that may induce observable CMB distortions.

In the slow-roll inflation scenario, by integrating

$$\frac{{\rm d}\phi}{{\rm d}N} = -M_{\rm pl}^2 \frac{{\rm d}\ln V}{{\rm d}\phi} \tag{8.5}$$

one obtains the number of e-folds realized some field value ϕ and the end of inflation at $\phi_{\rm end} = \phi_{\rm c}$,

$$N(\phi) - N_{\rm end} = -\frac{\mu_{\rm VHI}^2}{4M_{\rm pl}^2}\left[x^2 + 2\ln(x)\right] + \frac{\mu_{\rm VHI}^2}{4M_{\rm pl}^2}\left[x_{\rm end}^2 + 2\ln(x_{\rm end})\right] \ . \tag{8.6}$$

Obviously the number of e-fold N_k for the field value ϕ_k at which the mode k exit the horizon, before the end of inflation can be obtained by inverting this relation. For simplicity, the number of e-folds realized at the pivot scale of CMB anisotropy is set to be independent of the energy scale of inflation and the details of the reheating process as $N_{k_{\rm p}} = 60$. Thus, once ϕ_k is obtained, it is straightforward to compute the spectral parameters for the mode k by using Eqs. (8.1), (8.2) and (8.4).

There are two free parameters $\mu_{\rm VHI}$ and $x_{\rm end}$ for the VHI. In order to apply the third criterion from Sect. 8.1, the spectral index in the plane ($\mu_{\rm VHI}$, $x_{\rm end}$) is calculated for both anisotropy pivot scale $k_{\rm p} = 0.05$ Mpc^{-1} and distortion pivot scale $k_{\rm d} = 42$Mpc^{-1}. The time of horizon exit of k_d is about 6.7 e-folds earlier than that for $k_{\rm p}$. In FIG. 8.2, we have plotted the contours for the spectral index on the scale $k_{\rm d}$. Furthermore, the contours of 95% C.L. constraints from Planck at the scale $k_{\rm p}$ are also plotted. As it can be seen from this figure, there is a region of parameter space, which goes from $\mu_{\rm VHI} \approx 4.2 M_{\rm pl}$ and

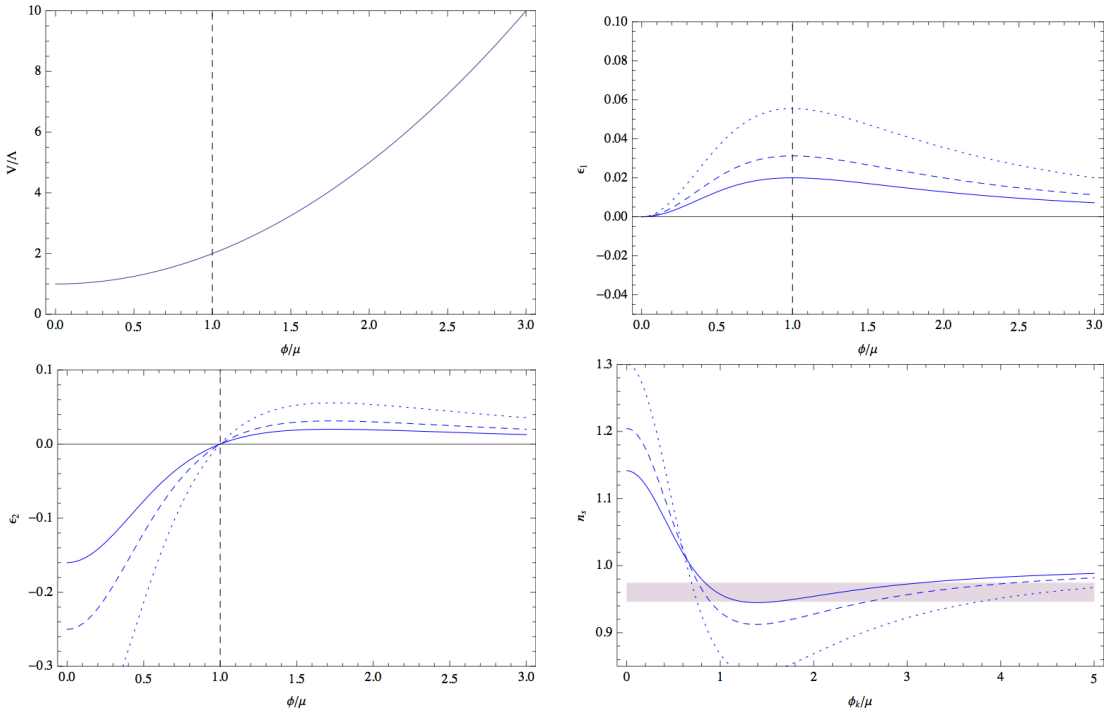

Figure 8.1: Top left: original hybrid potential. Top right and bottom left: first and second slow-roll parameters ϵ_1 and ϵ_2. Bottom right: scalar spectral index n_s as a function of ϕ_k with a horizontal band corresponds to the Planck 95% C.L. constraints. The parameter values in the diagrams for $\epsilon_{1,2}$ and n_s are $\mu_\mathrm{VHI} = 3M_\mathrm{pl}$ (dotted), $\mu_\mathrm{VHI} = 4M_\mathrm{pl}$ (dashed) and $\mu_\mathrm{VHI} = 5M_\mathrm{pl}$ (solid). Note that in the region close to $\phi_k/\mu_\mathrm{VHI} = 1$, the power spectrum of curvature perturbations is red-tilted, but becomes blue-tilted a few e-folds later (*i.e.* at smaller values of ϕ_k.)

$\log_{10} x_\mathrm{end} \approx -12$ up to $\mu_\mathrm{VHI} \approx 7M_\mathrm{pl}$ and $\log_{10} x_\mathrm{end} \approx -7$, can be in agreement with the Planck data and induce an in crease of power on distortion scale at the same time. In this region, the field values of the critical point $\phi_\mathrm{c} = x_\mathrm{end}\mu_\mathrm{VHI}$ are much below the Planck mass.

Then, three representative parameter sets are selected from the region identified in FIG. 8.2. We have plotted the resulting scalar power spectrum as a function of the e-fold time (the scale of mode) in FIG. 8.3, and the resulting spectrum of distortions in FIG. 8.4. From FIG. 8.3, we see that the amplitude of the power spectrum grows exponentially on the distortion scales. It can be one order of magnitude larger than the amplitude on anisotropy scales. According to Eq. (7.3) for PIXIE, distortions corresponding such enhancement are detectable at more than 5σ confidence level. This is confirmed in FIG. 8.4. The maximally enhanced amplitude corresponds to the level of μ-distortions $\mu \gtrsim 10^{-7}$ which is far above 5σ detection level of PIXIE. However, one can not distinguish those μ-distortions from other possible sources, such as evaporation of primordial black holes and dark matter decay/annihilation. Therefore, the spectrum of intermediate i-type distortions is also plotted, in order to distinguish between different origins of the signal. During inflation,

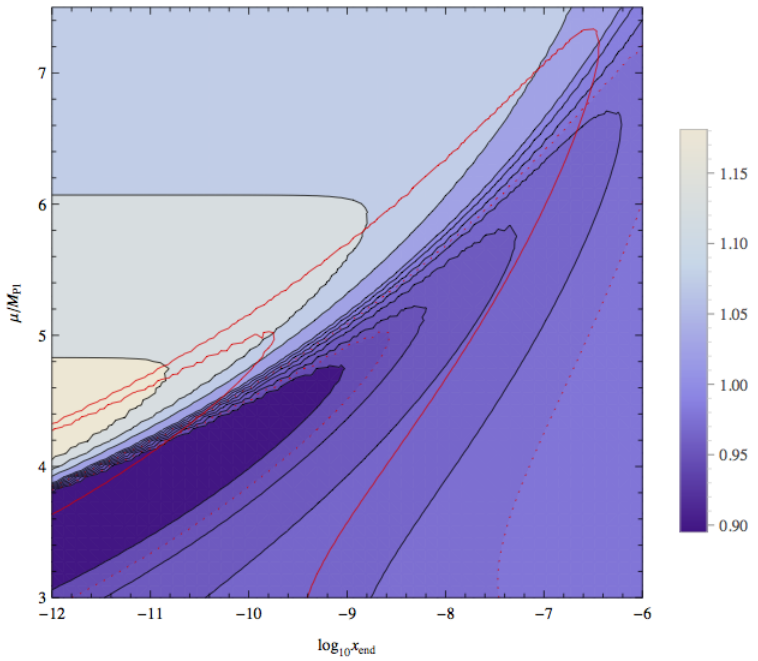

Figure 8.2: Contours of spectral index values from $n_s = 0.94$ up to $n_s = 1.15$ for the hybrid inflation in the valley with $N_{k_{\rm p}} = 60$ in the plane $\mu_{\rm VHI}$ - $\log_{10}(\phi_{\rm c}/\mu_{\rm VHI})$, evaluated at the scale $k_{\rm d} = 42{\rm Mpc}^{-1}$. The area between the solid red contours is consistent with the Planck measurement of the spectral index at $k_{\rm p} = 0.05$ Mpc^{-1} at 95% C.L.. The corresponding contours evaluated at the scale $k_{\rm d}$ are included (dotted red) in order to show how the spectral index changes when the scale varies.

perturbation modes of smallest scales re-enter the horizon earlier than that of larger scales and contribute to energy injection in the primeval plasma at earlier time. Therefore, enhanced power spectrum in the smallest distortion scales induce more μ-distortions, while the enhancement on the largest distortion scales corresponds to more i-type distortions. Then, it is easy to understand the behaviour in FIG. 8.4 where the i-type distortions dominate over the μ-type in the case of a limited enhancement of the power spectrum. With Eq. (7.1), we find that the signal of i-type distortions is detectable by PIXIE at more than 5σ along the band with $\phi_{\rm c} \lesssim 10^{-9} M_{\rm pl}$, and at about 2σ if $\phi_{\rm c} \lesssim 10^{-8} M_{\rm pl}$. Even if the μ-distortions are dominant, the level of i-type distortions does not decrease and is still detectable. For the sensitivity of a PRISM-class experiment, which is ten times better than PIXIE, a precise parameter estimation should be allowed and the probed parameter space would be extended to the entire band identified in FIG 8.2. Finally, we conclude that CMB distortions that induced by the original hybrid model in the fast water fall regime with a transition between the field-dominated and the vacuum dominated regime occurs $N_k \approx 55$ e-folds before the end of inflation, can be observed by PIXIE, only if the inflaton field is super-Planckian and in a fine-tuned regime of the parameter space.

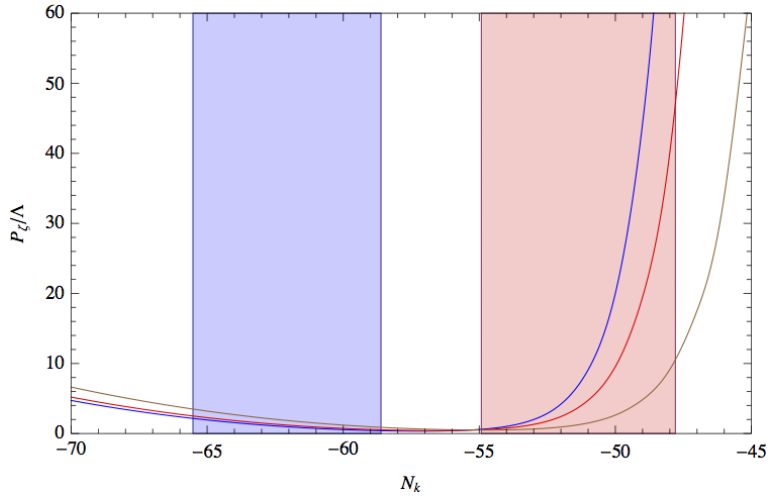

Figure 8.3: Amplitude of the power spectrum of curvature perturbations for three parameter sets: $\mu_{\rm VHI} = 5M_{\rm pl}$ and $\log_{10}(\phi_{\rm c}/\mu_{\rm VHI}) = -10$ (blue), $\mu_{\rm VHI} = 5.5M_{\rm pl}$ and $\log_{10}(\phi_{\rm c}/\mu_{\rm VHI}) = -9$ (red), $\mu_{\rm VHI} = 6.M_{\rm pl}$ and $\log_{10}(\phi_{\rm c}/\mu_{\rm VHI}) = -8$ (brown). The blue region corresponds to scales observable with standard CMB angular observations whereas the red region corresponds to scale that can be probed with CMB distortions. This amplitude can be normalised to $\mathcal{P}_\zeta(k_{\rm p}) = 2. \times 10^{-9}$ by a suitable choice of the parameter Λ.

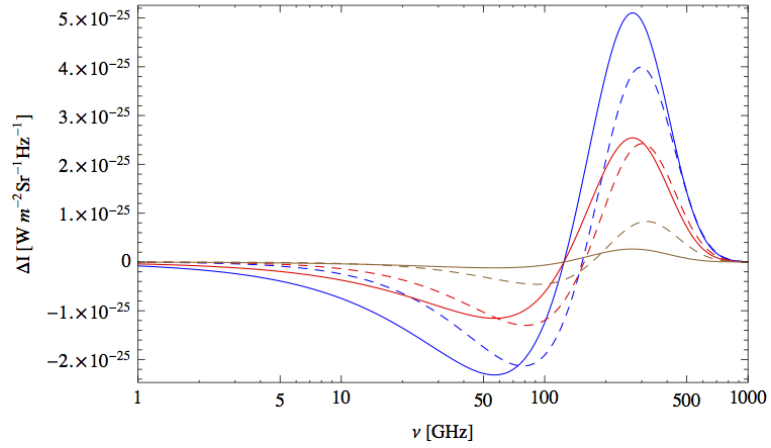

Figure 8.4: Spectrum of intermediate (dashed) and μ-type (solid) spectral distortions, for the HVI and the parameter sets as in Fig. 8.3. They correspond, respectively, to $\mu = 1.7 \times 10^{-7}$ (blue), $\mu = 8.5 \times 10^{-8}$ (red) and $\mu = 2.5 \times 10^{-8}$ (brown). The signal is observable by PIXIE at more than 5σ in the first two cases, and at about 2σ in the latter case.

8.3 Non-canonical Kähler inflation (NCKI)

In the ordinary F-term and D-term hybrid models, the flat direction of the potential is lifted radiative loop corrections and supergravity corrections that are induced by a canonical Kähler potential. Higher order operators may give additional corrections to the potential. If the Kähler potential is non-canonical, it will generate an extra mass term for the inflaton, and become hilltop inflation. The potential reads

$$V(\phi) = \Lambda \left(1 + \alpha \ln x + \beta x^2\right) , \tag{8.7}$$

where $x = \phi/M_{\rm pl}$. The parameter α is dimensionless and positive, whereas β is of order $\mathcal{O}(1)$ and can either be positive or negative. The NCKI potential encompasses a large variety of models, e.g. it recovers the original hybrid model in the limit $\alpha \to 0$ and recovers the potential with a purely radiatively lifted flat direction as $\beta \to 0$. Moreover, inflation can proceed in many different ways for the NCKI potential. In the case of $\beta > 0$, inflation can be driven by field rolls back along the potential that increase monotonously with $|\phi|$, and it ends with a waterfall instability. For $\beta < 0$ case, the field evolves both sides from the maximum of potential will occur inflation. The slow-roll parameters for the present model is given by [27]

$$\epsilon_1 = \frac{\left(\alpha + 2\beta x^2\right)^2}{2\left[\alpha x \log(x) + \beta x^3 + x\right]^2} , \tag{8.8a}$$

$$\epsilon_2 = \frac{2\left[(5\alpha - 2)\beta x^2 + \alpha \log(x)\left(\alpha - 2\beta x^2\right) + \alpha(\alpha + 1) + 2\beta^2 x^4\right]}{\left[\alpha x \log(x) + \beta x^3 + x\right]^2} \tag{8.8b}$$

and are plotted in FIG. 8.5 for several parameter sets. Note that only if $\beta > 0$, the second slow-roll parameter ϵ_2 can take negative values. According to our first criterion in Sec. 8.1, we need only to consider the case where $\beta > 0$. We have also plotted the spectral index in FIG. 8.5. We find that the power spectrum is blue when the field ϕ takes intermediate values. In the NCKI model, inflation can stop by two different ways: i) the field trajectory reaches the critical point ϕ_c where the potential develops a tachyonic instability, which is assumed to be instantaneous, ii) the slow-roll conditions are violated. In order to identify the end of inflation in the second case, we take $\epsilon_2 = 1$ as the condition that is well approximated by the field at

$$\phi_{\rm end} = \sqrt{2}\alpha \, . \tag{8.9}$$

The number of e-folds and field values at horizon exit can be obtained numerically by integration Eq. (8.5) in the slow-roll approximation. In FIG. 8.6, we have plotted the spectral index value for the pivot scale of distortions $k_{\rm d} = 42{\rm Mpc}^{-1}$ in the 2-dimensional parameter space. By imposing the 95% C.L. Planck constraints at the pivot scale $k_{\rm p} = 0.05{\rm Mpc}^{-1}$, we identify a very thin band in parameter space for the parameters α up to $\alpha \simeq 10^{-3}$ and $10^{-2} \lesssim \beta \lesssim 10^{-1}$ where the induced power spectrum is coincided with observations and enhanced on distortion scales. However, as shown in FIG. 8.7 and 8.8, the increase of power cannot exceed one order of magnitude, and the signal of distortions is not detectable. One should also notice that the transition of the spectral index from red to blue between the scales $k_{\rm d}$ and $k_{\rm p}$ requires a trans-Planckian inflaton field during the

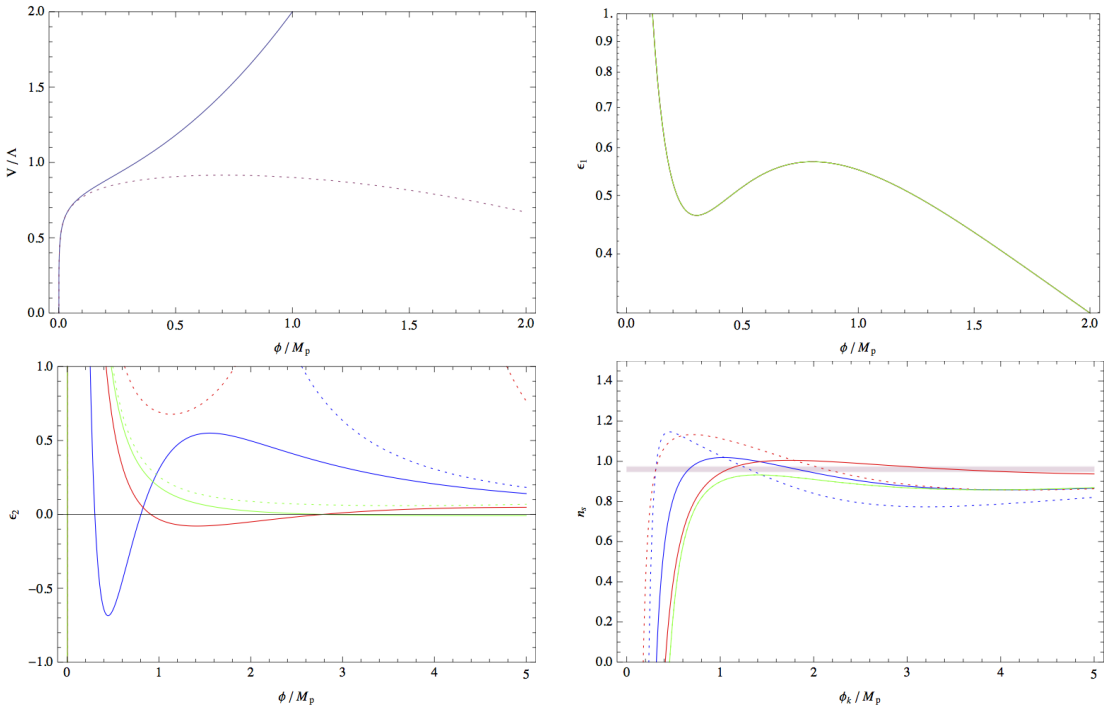

Figure 8.5: Top left: potential of the NCKI model for the parameters $\alpha = 0.1$, $\beta = 1$ (blue, solid) and $\alpha = 0.1$, $\beta = -0.1$ (red, dotted). Top right: first slow-roll parameter ϵ_1. bottom left: second slow-roll parameter ϵ_2. Bottom right: spectral index value as a function of ϕ_k. The parameter sets in the plots for $\epsilon_1, \epsilon_2, n_s$ are: $\alpha = 0.1$, $\beta = 1$ (blue, solid); $\alpha = 0.1$, $\beta = -1$ (blue, dotted); $\alpha = 0.1$, $\beta = 0.1$ (red, solid); $\alpha = 0.1$, $\beta = -0.1$ (red, dotted); $\alpha = 0.1$, $\beta = 0.01$ (green, solid); $\alpha = 0.1$, $\beta = -0.01$ (green, dotted).

horizon exit of these scales. This might contradict the assumptions about the validity of SUSY as an effective field theory, which requires field to be sub-Planckian. Moreover, we notice that the approximation for potential (8.7) is valid only if $\alpha \gg \Lambda^{1/3}/[2^6\pi^{14/3}M_{\rm pl}^{4/3}]$, *cf.* the detailed form of the F-term potential in Ref. [46]. Thus, this constraint has been indicated in FIG. 8.6, and rules out parts the parameter space which satisfies the third condition from Sec. 8.1 from the outset.

8.4 Generalized MSSM inflation (GMSSM)

The Minimal Supersymmetric Standard Model (MSSM) inflation that was proposed in Ref. [98] induce an eternal inflation at the inflection point where the first slow-roll parameter ϵ_1 vanishes. Therefore, it is ruled out by the second criterion from Sec. 8.1. However, the Generalized MSSM Inflation (GMSSM) [27] scenario with only an approximate inflection point [99] is still survived. The GMSSM model can be parameterized as

$$V(\phi) = \Lambda\left(x^2 - \frac{2}{3}\alpha x^6 + \frac{1}{5}\alpha x^{10}\right), \tag{8.10}$$

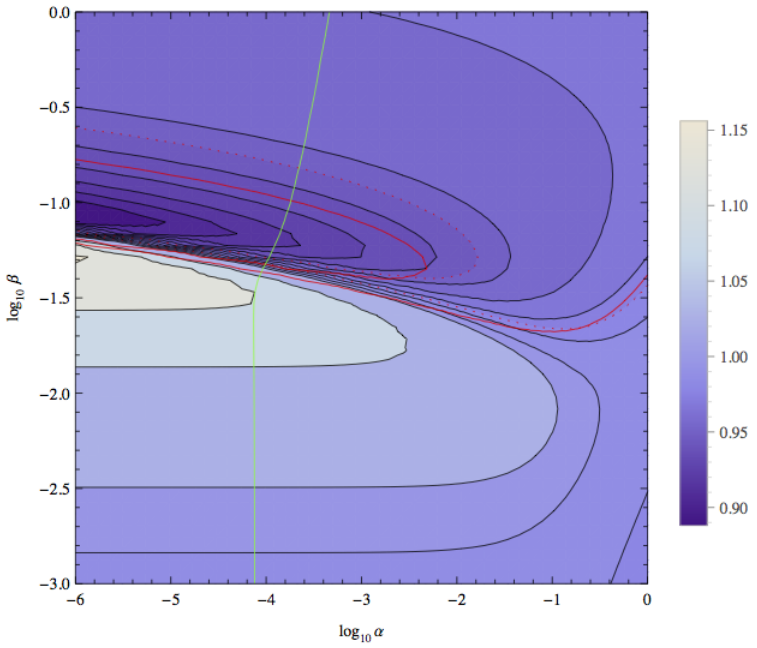

Figure 8.6: Contours of spectral index values for the NCKI model, at $k_{\rm d} = 42$ Mpc^{-1}. The area between the solid red contours is in agreement with the Planck constraints on $n_{\rm s}$ for the pivot scale of CMB anisotropies $k_{\rm p} = 0.05$ Mpc^{-1}. The dashed red contours for the scale $k_{\rm d}$ are added (dotted red) to illustrate how the spectral index changes when the scale varies. To the left of the green, solid and almost vertical line, the approximation of the radiative correction to the potential in the form (8.7) is not valid.

where $x \equiv \phi/\phi_0$ and α is a dimensionless parameter. The power terms of x comes from the lowest order soft and non-renormalizable operators which lift the flat direction in the MSSM [98]. If $\alpha = 1$, the potential recovers the original MSSM model which features an exact inflection point. As $\alpha > 1$, it develops a maximum. Inflation can occur for three different field trajectories (evolve toward both sides of the maximum and from the large field regime toward decreasing field values). For $\alpha < 1$, the potential is monotonous. There is no inflection point and only one possible inflationary regime. The different possibilities are represented in FIG. 8.9. The slow-roll parameters read [27]

$$\epsilon_1 = M_{\rm pl}^2 \frac{450\left[\alpha\left(x^4-2\right)x^4+1\right]^2}{\phi_0^2 x^2\left[\alpha\left(3x^4-10\right)x^4+15\right]^2}\,, \tag{8.11a}$$

$$\epsilon_2 = M_{\rm pl}^2 \frac{60\left(\alpha x^4\left\{x^4\left[\alpha\left(3x^8+20\right)-78\right]+40\right\}+15\right)}{\phi_0^2 x^2\left[\alpha\left(3x^4-10\right)x^4+15\right]^2}\,. \tag{8.11b}$$

Note that for $\alpha < 9/25$, the second slow-roll parameter ϵ_2 is always positive since the potential is convex everywhere. With our first criterion from Sec. 8.1, this case can be rejected. In the standard situation [98, 99], it requires $\phi \ll M_{\rm pl}$ during inflation to valid the effective field theory description. Moreover, in the MSSM scenario, we have $\Lambda \sim M_{\rm pl}^{3/2} m_{\rm SUSY}^{5/2}$ and $\phi_0 \sim M_{\rm pl}^{3/4} m_{\rm SUSY}^{1/4}$. Therefore, inflation can only proceed in the vicinity of the approximate inflection point (or the vicinity of the local maximum point),

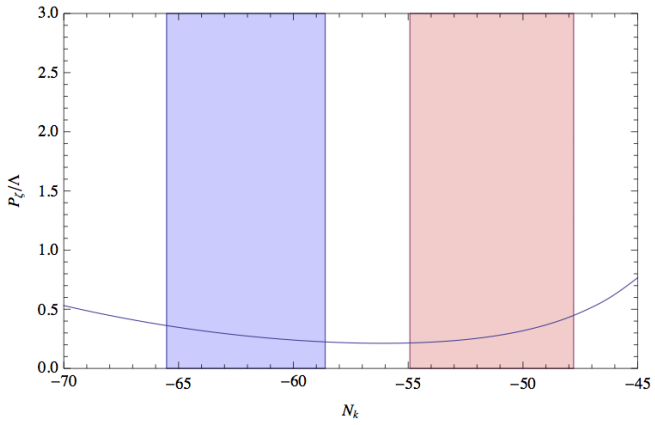

Figure 8.7: Amplitude of power spectrum of curvature perturbations for the NCKI model with $\alpha = 10^{-6}$ and $\beta = 10^{-1.2}$. Those parameter values lie in the region where the approximation of the radiative corrections is not valid but are representative of the strongest possible enhancement of power on CMB distortion scales considering an effective potential of the form of Eq. 8.7.

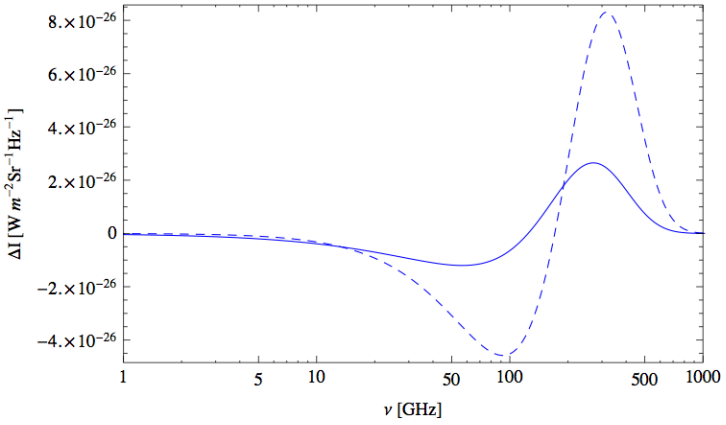

Figure 8.8: Intermediate and μ-distortions (respectively dashed and solid line) as a function of frequency for the NCKI model with $\alpha = 10^{-6}$ and $\beta = 10^{-1.2}$. They correspond to $\mu = 8.9 \times 10^{-9}$ and $y = 5.5 \times 10^{-9}$ and can not reach the detectability by PIXIE. They are nevertheless enough for the sensitivity of a PRISM-class experiment.

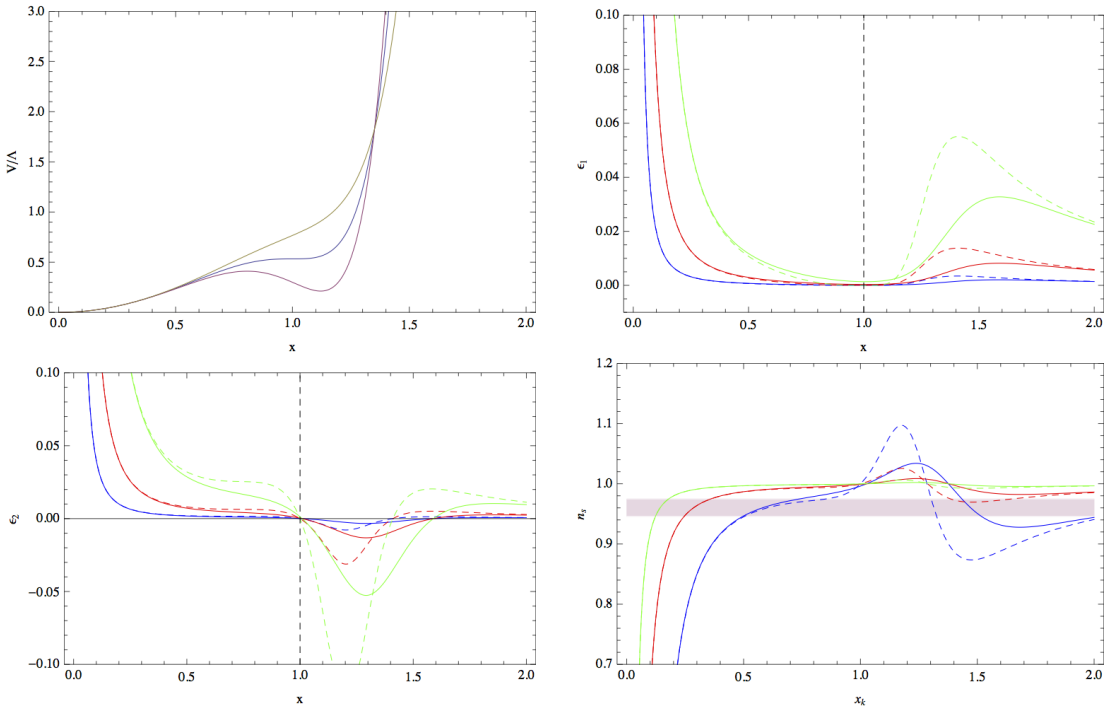

Figure 8.9: Field potential (top left) for the GMSSM model with $\alpha = 1.5$ (red), $\alpha = 1$ (blue) and $\alpha = 0.5$ (yellow). First and second slow-roll parameters (respectively top right and bottom left) and spectral index value as a function of ϕ_k (bottom right), for $\phi_0 = (100, 50, 25)M_{\rm pl}$ (respectively blue, red and green) and $\alpha = 0.5, 1$ (respectively dashed and solid). A blue tilted phase ($n_{\rm s} > 1$) follows a red-tilted phase ($n_{\rm s} < 1$) in the case $\alpha < 1$ and $\phi_0 \gg M_{\rm pl}$.

and $\alpha \simeq 1$, such that the value of the second slow-roll parameter is not much larger than unity during inflation. Besides, the second slow-roll parameter ϵ_2 can only pass from negative to positive values during inflation that implies a blue spectrum on the large scale and a red spectrum on smaller scales. Therefore, this regime cannot lead to a detectable level of distortions for PIXIE.

Nevertheless, if we allow the effective theory description breaks down due to a super Planckian field value $\phi \gg M_{\rm pl}$ and take $\alpha < 1$, then the value of ϵ_2 pass from positive to negative and then again become positive. In this case, inflation is also viable since $\epsilon_1 \ll 1$. Hence, it is an interesting regime. For this regime, the slow-roll parameters and spectral index is presented in FIG. 8.9. Inflation ends at the point $x_{\rm end} \simeq \sqrt{2}M_{\rm pl}/\phi_0$ by violation of the slow-roll conditions. Again, we integrate the Klein-Gordon equation (8.5) in the slow-roll approximation to obtain the value of inflaton ϕ_k at horizon exit for the given mode. Then, we can evaluate the values of spectrum index at the two pivot scale $k_{\rm p} = 0.05{\rm Mpc}^{-1}$ and $k_{\rm d} = 42{\rm Mpc}^{-1}$, which are illustrated in FIG. 8.10. One can observe that the spectral index on the scale $k_{\rm d}$ is always below unity if the Planck constraints are imposed. As a consequence, the third criterion from Sec. 8.1 cannot be satisfied with this regime. We can therefore conclude that the model cannot lead to any detectable spectral

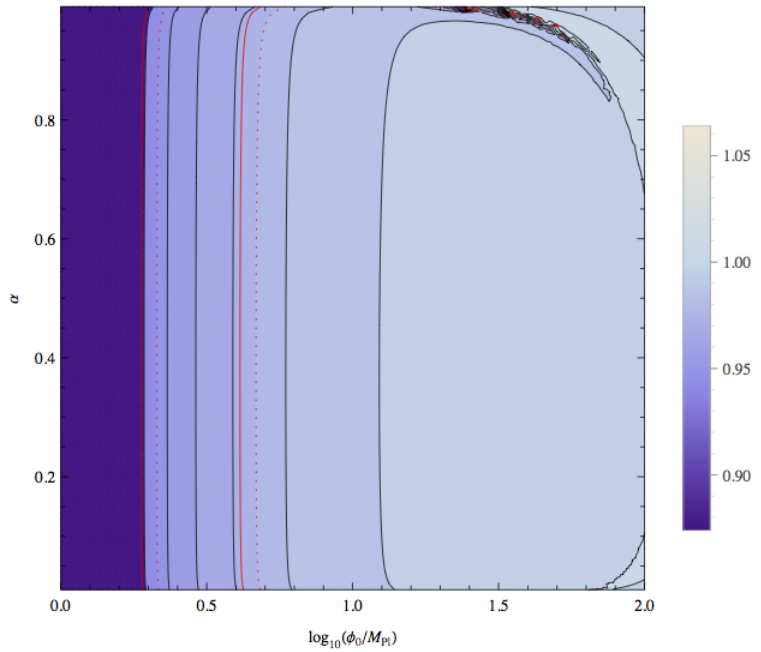

Figure 8.10: Spectral index value in the parameter space for the GMSSM model, for the pivot scale of CMB anisotropies $k_{\rm p} = 0.05$ Mpc^{-1} and of CMB distortions $k_{\rm d} = 42$ Mpc^{-1}. Between the solid red contours is the area allowed by the Planck constraints. The same contours for the scale $k_{\rm d}$ (dashed red) visualize how the spectral index changes when the scale varies.

distortion of the CMB spectrum.

8.5 Generalized renormalizable inflection point inflation (GRIPI)

The potential of GRIPI is very similar to the GMSSM scenario except the differ in power, which reads

$$V(\phi) = \Lambda \left(x^2 - \frac{4}{3}\alpha x^3 + \frac{1}{2}\alpha x^4 \right) , \tag{8.12}$$

where we define $x \equiv \phi/\phi_0$. The dimensionless parameter α distinguishes the model from the renormalizable inflection point inflation (RIPI) scenario, which has an exact inflection point. The theoretical motivations for the GRIPI are also similar to the GMSSM case. The potential of GRIPI can be given by the MSSM with three additional superfields representing right handed neutrinos. In this case, the A-term is cubic, and it requires $\phi_0 \sim 10^{14}$ GeV to keep the soft SUSY-breaking mass in the anticipated range [100]. The field potential is plotted in FIG. 8.11. In the case where $\alpha = 1$, it recovers the RIPI model. When $\alpha > 1$, the potential develops a maximum and, as for the GMSSM model, there are three possible inflationary regimes, whereas if $\alpha < 1$ the potential increases monotonously

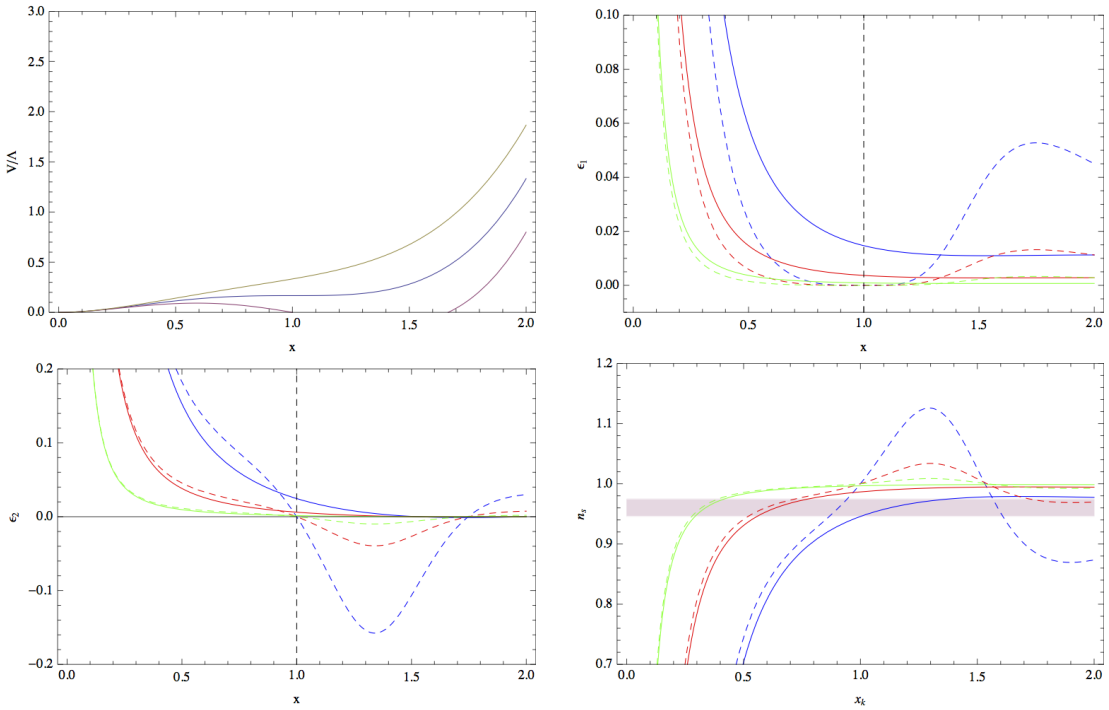

Figure 8.11: Field potential (top left) for the GRIPI model with $\alpha = 0.8/1/1.2$ (respectively in yellow, blue and red). First and second slow-roll parameters (respectively top right and bottom left), as well as spectral index value as a function of ϕ_k (bottom right), for the parameters $\phi_0 = 10M_{\rm pl}$ (blue), $\phi_0 = 20M_{\rm pl}$ (red) and $\phi_0 = 40M_{\rm pl}$ (green), and $\alpha = 0.5$ (solid) or $\alpha = 1$ (dashed). As for the GMSSM model, a phase with $n_{\rm s} > 1$ occurs between two phases with $n_{\rm s} < 1$ when $\alpha < 1$ and $\phi_0 \gg M_{\rm pl}$.

and there is no exact inflection point. The slow-roll parameters are given by [27]

$$\epsilon_1 = M_{\rm pl}^2 \frac{72\left[\alpha(x-2)x+1\right]^2}{\phi_0^2 x^2\left[\alpha x(3x-8)+6\right]^2}\,, \tag{8.13}$$

$$\epsilon_2 = M_{\rm pl}^2 \frac{24\left(\alpha x\left\{x\alpha\left[3(x-4)x+16\right]+3x-16\right\}+6\right)}{\phi_0^2 x^2\left[\alpha x(3x-8)+6\right]^2}\,. \tag{8.14}$$

They are presented in FIG. 8.11, as well as the spectral index as a function of ϕ_k. Because of the same reasons as the GMSSM case, the standard regime with $\phi_0 \ll M_{\rm pl}$ cannot lead simultaneously to a red spectrum on CMB anisotropy scales and a blue spectrum on distortion scales. Although the regime where $\phi_0 \gtrsim M_{\rm pl}$ with $\alpha < 1$ is not well-motivated in the original SUSY framework, it can be considered as a toy model and is interesting in the view of CMB distortions.

As for the GMSSM model, inflation ends at $x_{\rm end} \simeq \sqrt{2}M_{\rm pl}/\phi_0$ by violation of the slow-roll conditions. The field value ϕ_k at the horizon exit of mode k can be determined by integration the Klein-Gordon equation in the slow-roll approximation. Then, we have evaluated the spectral index in the two-dimensional parameter space of the model for the scales $k_{\rm p}$ and $k_{\rm d}$. Those are illustrated in FIG. 8.12. As for the GMSSM case, the spectral

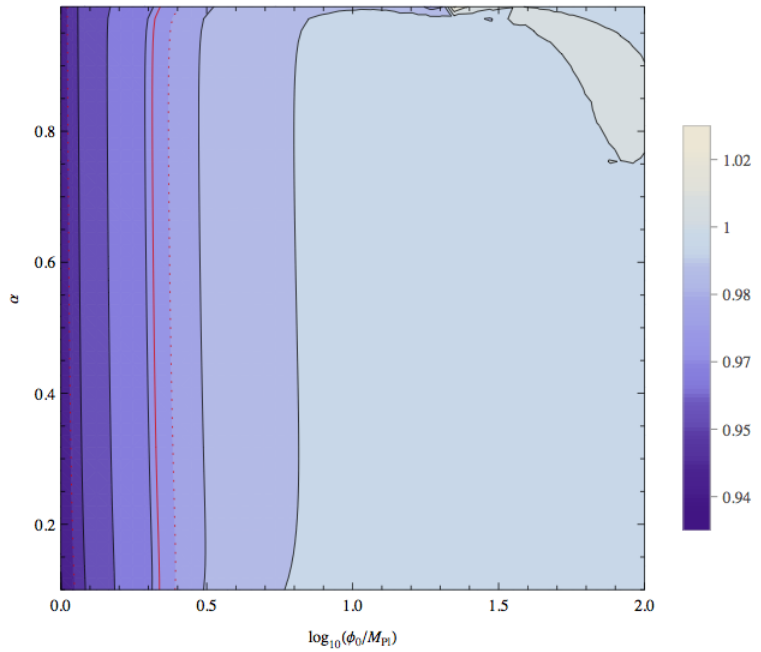

Figure 8.12: Contours of Spectral index values for the GRIPI model evaluated for the pivot scale of CMB distortions $k = 42\text{Mpc}^{-1}$ (right). To the left of the solid red contour, there is the Planck-allowed region for the spectral index evaluated at the scale $k_\text{p} = 0.05\ \text{Mpc}^{-1}$. The same contours at the scale k_d (dashed red) visualize how the spectral index changes when the scale varies.

index on distortion scales cannot be larger than unity after imposing the 95 % C.L. Planck constrains. Therefore, we conclude that the model cannot induce any observable distortion of the CMB black-body spectrum.

8.6 Running-mass inflation (RMI)

This model is base on the supersymmetric framework with a flat direction of the potential that is lifted by a soft-SUSY breaking mass term [101, 102, 103, 104, 105]. The higher order terms are suppressed since the inflaton field is sub-Planck where $\phi \ll M_\text{pl}$. Loop logarithmic corrections are embedded into the tree level potential that reads [27]

$$V(\phi) = \Lambda \left[1 - \frac{c}{2} \left(-\frac{1}{2} + \ln \frac{\phi}{\phi_0} \right) \frac{\phi^2}{M_\text{pl}^2} \right] , \tag{8.15}$$

where the dimensionless parameter c can be either positive or negative. With the assumption of a Hubble-scale soft mass $m \simeq H$, one can estimate that $c \lesssim 0.1$ [27]. When $\phi = \phi_0$, the potential develops a maximum for the case $c > 0$, and develops a minimum for $c < 0$. The potential is present in FIG. 8.13. There are four inflationary regimes which named as RMI1, RMI2, RMI3 and RMI4 in Ref. [27]. RMI1 corresponds to $c > 0$ and $\phi < \phi_0$ (field evolves from the maximal potential point to small field values); RMI2 to $c > 0$ and $\phi > \phi_0$ (field evolves from the maximal potential point towards large values); RMI3 to

$c < 0$ and $\phi < \phi_0$ (inflation proceeds from small field toward the minimum) and RMI4 corresponds to $c < 0$ and $\phi > \phi_0$ (inflation proceeds from large field toward the minimum). The slow-roll parameters read

$$\epsilon_1 = \frac{8c^2x^2\ln^2\left(\frac{x}{\phi_0}\right)}{\left[-2cx^2\ln\left(\frac{x}{\phi_0}\right)+cx^2+4\right]^2}\,, \tag{8.16}$$

$$\epsilon_2 = \frac{8c\left\{\ln\left(\frac{x}{\phi_0}\right)\left[2cx^2\ln\left(\frac{x}{\phi_0}\right)-cx^2+4\right]+cx^2+4\right\}}{\left[-2cx^2\left(\frac{x}{\phi_0}\right)+cx^2+4\right]^2}\,, \tag{8.17}$$

where $x \equiv \phi/M_{\rm pl}$. Together with spectral index as a function of ϕ_k, they are presented in FIG. 8.13.

In the RMI2 regime, the second slow-roll parameter is always positive which leads to a red scalar power spectrum. Thus, this regime is not interested in the present context. In contrast, the first two criteria of Sec. 8.1 can be satisfied in RMI1, RMI3 and RMI4 regimes. Therefore, we discuss on them respectively with a numerical integration on the slow-roll dynamics. Furthermore, for a PRISM-class probe, a useful parameter $s = c\log(\phi_0/\phi_*)|_{k=k_{\rm p}}$ can be introduced following Ref. [105]. Then, one obtains

$$s = \mp\, c\mathrm{e}^{-cN_{k_{\rm kp}}}\log c_2\,, \quad \text{for RMI1 and RMI2}\,, \tag{8.18a}$$

$$s = -\,c\mathrm{e}^{-cN_{k_{\rm kp}}}\log(1-c_2)\,, \quad \text{for RMI3 and RMI4}\,. \tag{8.18b}$$

(Note that for RMI1,2,3, $c_2 > 0$, while for RMI4, $c_2 < 0$.) Thus, one can relate the bounds from FIG. 7.3 to the model parameters with the relations $n_s = -2c + 2s$ and $n_{\rm run} = 2sc$. Earlier projections which is not based on MCMC analysis have been done in Ref. [90].

8.6.1 RMI1: $c > 0$, $\phi < \phi_0$

In the RMI1 regime, inflation ends by violation of the slow-roll conditions when trajectories reach the point $\phi \simeq \phi_0\exp[-6(1+1/2c)]$. However, this value is exponentially suppressed since $c \lesssim 1$. In practice, we consider that inflation ends before this point with a tachyonic waterfall instability which is triggered by some auxiliary fields. Moreover, we have assumed that the waterfall phase is instantaneous. Nevertheless, it introduces an additional parameter $\phi_{\rm c}$ which is the field value at the critical point. Here, we define the dimensionless parameter $c_2 \equiv \phi_{\rm c}/\phi_0$, and focus on the regime $\phi_0 < M_{\rm pl}$.

For the case $\phi_0 = 0.1M_{\rm pl}$, the prediction for the scalar spectral index at the scales $k_{\rm p}$ and $k_{\rm d}$ in the plane (c, c_2) are illustrated in FIG. 8.14. Note that the contours change insignificantly when varying ϕ_0 in the range $\phi_0 < M_{\rm pl}$. From this figure, one can observe that the blue tilted spectral at the distortion scales are impossible to be consistent with the 95 % C.L. constraints of Planck. Therefore, we conclude that the RMI1 regime does not give rise to any observable distortion of the CMB spectrum.

8.6.2 RMI3: $c < 0$, $\phi < \phi_0$

In the RMI3 regime, the minimum of potential locates at $\phi = \phi_0$. Inflation is realized when the inflaton field rolls from small values toward the minimum, and stops at the critical

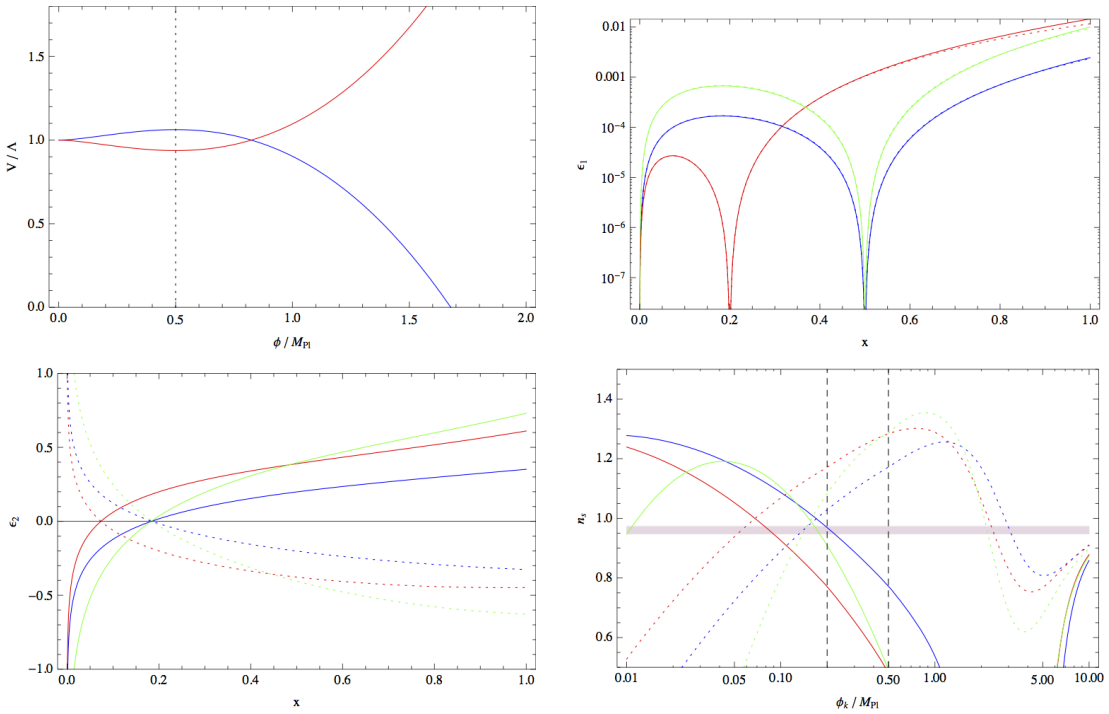

Figure 8.13: Field potential (top left) for the RMI, for $\phi_0 = 0.5M_{\rm pl}$, $c = 1$ (blue) and $c = -1$ (red). First and second slow-roll parameters (respectively top right and bottom left) as well as spectral index as a function of ϕ_k (bottom right) are represented for the parameters $\phi_0 = 0.5M_{\rm pl}$ and $c = 0.1$ (solid blue), $\phi_0 = 0.2M_{\rm pl}$ and $c = 0.1$ (solid red), $\phi_0 = 0.5M_{\rm pl}$ and $c = 0.2$ (solid green), $\phi_0 = 0.5M_{\rm pl}$ and $c = -0.1$ (dotted blue), $\phi_0 = 0.2M_{\rm pl}$ and $c = -0.1$ (dotted red), $\phi_0 = 0.5M_{\rm pl}$ and $c = -0.2$ (dotted green).

point $\phi_c < \phi_0$ where a tachyonic instability is triggered. For convenience, the additional parameter c_2 is defined as $\phi_c = (1 - c_2)\phi_0$.

As for RMI1, contours of the spectral index at the scale $k_{\rm d}$ in the plane (c, c_2), together with the Planck 95 % C.L. constraints at the scale $k_{\rm p}$ are presented in FIG. 8.15 for the case $\phi_0 = 0.1M_{\rm pl}$. Contrary to RMI1, there is a narrow region of parameter space where $c \sim \mathcal{O}(0.1)$ and $c_2 < 0.01$ can lead to a blue spectrum on distortion scales and satisfies the Planck constraints simultaneously. The scalar power spectrum and the resulting distortions for two representative parameter sets are plotted in FIG. 8.17 and FIG. 8.18 respectively. Then, we find that the level of spectral distortions induced by the enhancement of scalar power spectrum, cannot be detected by PIXIE. However, it is detectable by an experiment with instrumental sensitivity of the PRISM class. Moreover, note that for the small values of c_2, the power spectrum on the largest observable scales is also enhanced due to the abrupt variation of the spectral index. Furthermore, note that as long as $\phi_0 < M_{\rm pl}$, our results are independent of the value of ϕ_0.

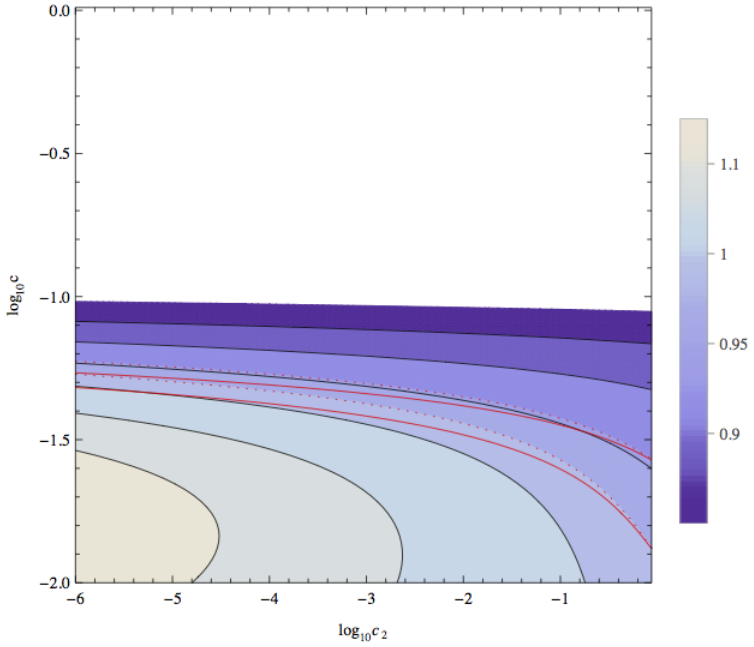

Figure 8.14: Spectral index for the RMI1 regime, with $\phi_0 = 0.1M_{\rm pl}$, evaluated for the pivot scale of CMB distortions $k = 42{\rm Mpc}^{-1}$ and Planck-allowed region for the spectral index evaluated at the scale $k_{\rm p} = 0.05$ Mpc^{-1} (red). The corresponding contours at the scale $k_{\rm d}$ are added (dashed red) to illustrate how the spectral index changes when the scale varies. The white region correspond to values of ϕ_k too close of ϕ_0 to be numerically tractable. In this case the spectral index is well approximated by $n_{\rm s} = 1 - 2\epsilon_k \simeq 1 - 4c$.

8.6.3 RMI4: $c < 0$, $\phi > \phi_0$

In the RMI3 regime, inflation is realized when the inflaton field rolls from large values toward the minimum $\phi = \phi_0$, and stops at the critical point $\phi_c > \phi_0$ where a tachyonic instability is triggered. As for RMI3, the parameter c_2 is defined as $\phi_c = (1 - c_2)\phi_0$. Contrary to RMI1 and RMI3 cases, the shape of the contours of the spectral index depends on the value of ϕ_0 in the RMI4 regime. In FIG. 8.16, we have illustrated the contours for $\phi_0 = M_{\rm pl}$ and $\phi_0 = 0.1M_{\rm pl}$, and again, imposed the Planck limits. As $\phi_0 \lesssim 0.1M_{\rm pl}$, there is no overlap between the region of $n_{\rm s}(k_{\rm d}) > 1$ and the Planck bound. However, when $\phi_0 \sim M_{\rm pl}$, there can be a very narrow-overlapped band. Since inflation proceeds at the field value close to the Planck mass, the flatness of the potential is destroyed by SUGRA corrections. Even thought in this case, one cannot obtain a sufficient increase of power (illustrated in FIG. 8.17) to induce detectable distortions in the CMB frequency spectrum as shown in FIG. 8.18.

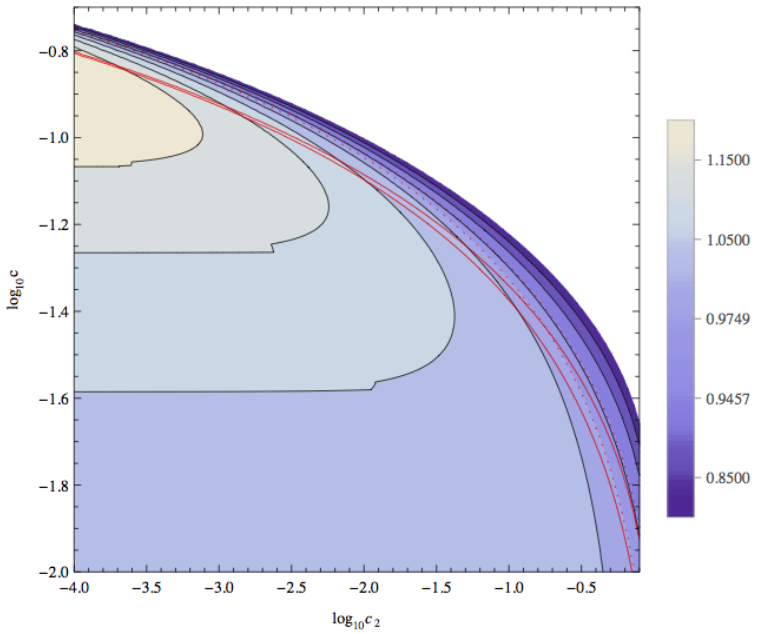

Figure 8.15: Same as in FIG. 8.14, for the RMI3 regime, with $\phi_0 = 0.1 M_{\rm pl}$.

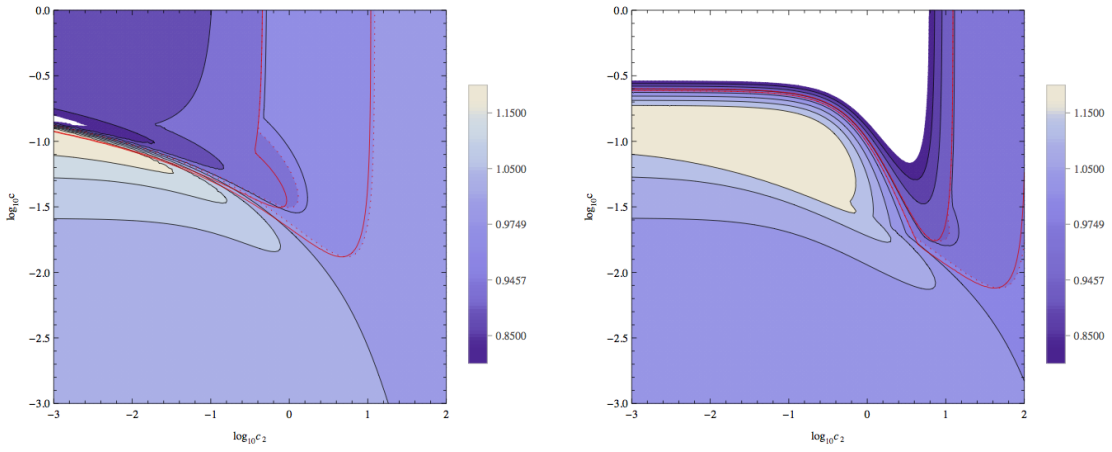

Figure 8.16: Same as in FIG. 8.14, for the RMI4 regime, with $\phi_0 = M_{\rm pl}$ (left) and $\phi_0 = 0.1 M_{\rm pl}$ (right).

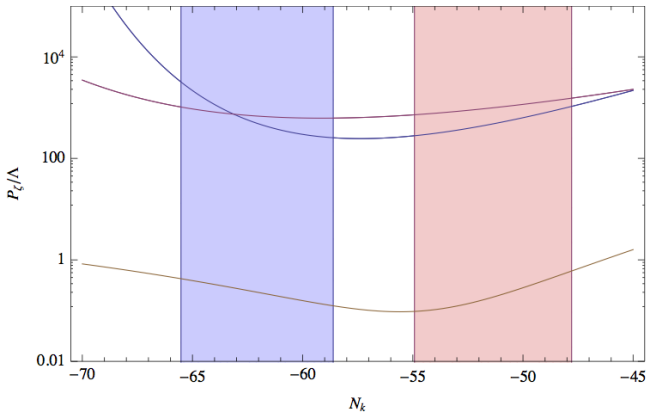

Figure 8.17: Amplitude of power spectrum of curvature perturbations for the RMI3 and RMI4 regimes with $c_2 = 10^{-4}$, $c = -\log_{10}(-0.8)$ (RMI3, blue), $c_2 = \log_{10}(-2.6)$, $c = -0.1$ (RMI3, red) and $c_2 = 10^{-3}$, $c = -\log_{10}(-0.9)$ (RMI4, brown). This amplitude can be normalized by a suitable choice of Λ.

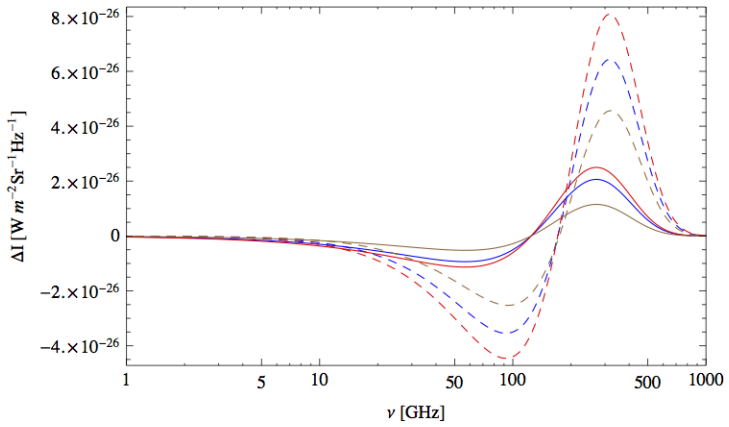

Figure 8.18: Intermediate and μ-distortions (respectively dashed and solid line) as a function of frequency for the RMI model, same parameters as in FIG. 8.17. They correspond to $\mu = 6.9\times10^{-9}$, $y = 6.4\times10^{-9}$ (blue), $\mu = 8.4\times10^{-9}$, $y = 5.2\times10^{-9}$ (red), $\mu = 3.9\times10^{-9}$, $y = 5.8\times10^{-9}$ (brown). In all cases the signal is below the 2σ sensitivity of PIXIE.

Chapter 9

Testing multi-field inflation with CMB distortions

The recent CMB anisotropy experiments [19, 20] still allow for multifield inflation models which can arise naturally from SUSY, GUT and string landscape. In multifield inflation scenarios, the isocurvature perturbations usual induce curvature perturbations as well as the adiabatic ones when field trajectories present some turns in field space. In this case, the field perturbations are no longer frozen on super-horizon scales. Therefore, a substantial level of non-Gaussianity is potentially generated, and the power spectrum of curvature perturbations is modified simultaneously. If an increase of power occurred on small scales, it might induce a detectable level of distortion of CMB spectrum. In this chapter, we consider three simple models of effective two-field scenarios:

- a softly turning trajectory,
- a suddenly turning trajectory,
- a mild waterfall trajectory.

Our analyses are base on analytical approximations which are derived in the literature [106, 107, 108, 109].

9.1 Softly turning trajectory

It is common to classify entropic (or isocurvature) and adiabatic field components [73] by their alignment orthogonal or parallel to the field trajectory respectively. The scalar power spectrum can be derived by several methods, such as the δN formalism [44, 74], the closed time path (CTP, also known as "in-in" or Schwinger-Keldysh) formalism[110], the effective field theory [111], etc. For the effective two-field inflation with a softly turning trajectory, one can identify three different cases,

- Both fields are almost massless: The curvature perturbations are related to the adiabatic perturbations, where the contribution of entropy modes is neglectable. It can be directly described by the single-field slow-roll dynamics with a small level of non-Gaussianity;
- The mass of isocurvature component is heavy ($m_{\rm iso} \gg H$): In order to realize slow-roll inflation, the mass of the adiabatic component must be sufficiently small. In this case, isocurvature perturbations decay quickly. It can be treated as *effectively single field*;

- The isocurvature mass is of the order of or larger than the Hubble rate ($m_{\rm iso} \simeq H$): It is called as *quasi effectively single field*, where entropy modes can take effect on the scale power spectrum on a broad range of scales.

In this section, we focus on the third case which can leads to an increase of power at distortion scales. In addition, we assumed the turning on the field trajectory starts at the time t_1 and ends at the time t_2 with a constant isocurvature mass $m_{\rm iso}$ as well as a constant angular velocity. Thus, for modes exit the horizon during the turn, the power spectrum of curvature perturbations is given by [106, 107]

$$\mathcal{P}_\zeta = \frac{H^4}{4\pi^2 R^2 \dot{\theta}^2} \left[1 + 8C(\mu_{\rm iso}) \left(\frac{\dot{\theta}}{H} \right)^2 \right] , \tag{9.1}$$

where $\mu_{\rm iso} \equiv \sqrt{m_{\rm iso}^2/H^2 - 9/4}$, R is the curvature radius of the turn in the field space, and $\theta(t)$ is the angle between the tangent vector to the trajectory and the initial direction of the trajectory. In the regime $m_{\rm iso} > 3H/2$, the function $C(\mu)$ can be well approximated by $C(\mu) = 1/4\mu^2$ [107].

At the starting point of the turn, one has $\dot{\phi} = R\dot{\theta}$. Thus, the standard expression for the spectrum amplitude of curvature perturbations is recovered. Under the slow-roll approximation, the first slow-roll parameter can be expressed by the radius R and the angular velocity $\dot{\theta}$ as $\epsilon_1 = \dot{\phi}^2/(2H^2 M_{\rm pl}^2)$. Then, one can obtain

$$\frac{\dot{\theta}^2}{H^2} = \frac{\epsilon_1}{R^2} \, . \tag{9.2}$$

Hence, the enhancement factor is proportional to $\sim \epsilon_1 M_{\rm pl}^2/(\mu_{\rm iso}^2 R^2)$. In the case where $\epsilon_1 \ll 1$ and $\mu \simeq \mathcal{O}(1)$, it requires $R \lesssim \sqrt{\epsilon} M_{\rm pl}$ to generate a significant increase of power. Moreover, if $\epsilon_1 \simeq \mathcal{O}(0.1)$, it requires $R \lesssim \mathcal{O}(0.1) M_{\rm pl}$ to potential induce observable distortions in the CMB spectrum with a enhanced power spectrum. In both cases, the value of R cannot exceed the typical value of field variation within the time of one e-fold, $\Delta\sigma \sim \sqrt{\epsilon} M_{\rm pl}$. This small R indicates that the turn lasts less than one e-fold, and it cannot have any significant change on the resulting spectral distortions compared with that for a trajectory with no turn. Therefore, we can conclude that the multifield inflation with a softly turning trajectories cannot induce an observable level of CMB distortions for the PIXIE experiment. To illustrate this result, the amplitude of power spectrum has been plotted in FIG. 9.1 for several parameter sets, with the adiabatic field variation during the turn $\Delta\sigma = R$ and with the number of e-folds N_t when the turn occurs. The corresponding CMB distortions are represented in FIG. 9.2. Note that the signal of CMB distortions at maximum is detectable with a PRISM-class experiment.

In fact, the formula (9.1) which should be applied only for constant turn trajectories, not strictly suit the case where the turn lasts less than one e-fold. Besides, the effect of damped oscillations or a bump-like shape that is generated at the onset of the turn [112, 113] is also not taken into account. However, the previous discussion gives a qualitative result for an ideal situation where the turn is slow enough. We left full numerical calculations of scalar power spectrum for the case of softly turning trajectories as future work.

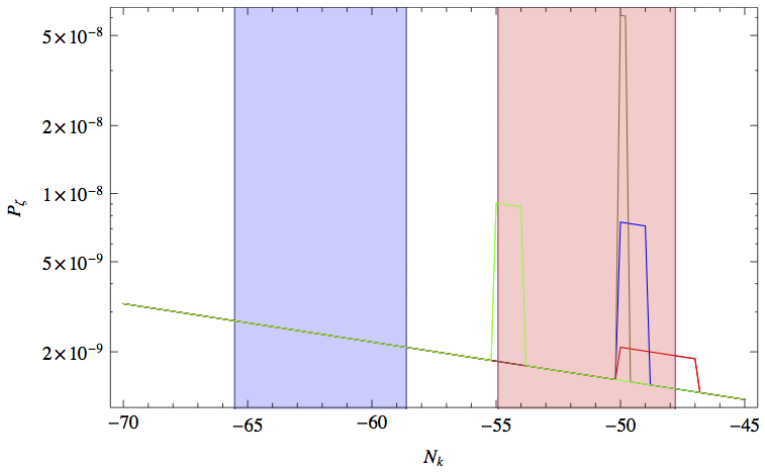

Figure 9.1: Spectrum amplitude of curvature perturbations as a function of the e-fold time of horizon exit, for softly turning trajectories, for $\mu_{\rm iso} = 1$ (which gives a maximum enhancement), with $N_t = 50$ (blue, brown and red curves) and $N_t = 55$ (green), and ΔN_t corresponding to $\Delta\sigma_t = R$. Blue and Green curves are for $\epsilon_1/(\mu_{iso}R)^2 = 1$ and $\epsilon_1 = 0.1$, the yellow curve is for $\epsilon_1/(\mu_{iso}R)^2 = 10$ and $\epsilon_1 = 10^{-5}$ and the red curve is for $\epsilon_1/(\mu_{iso}R)^2 = 0.1$ and $\epsilon_1 = 10^{-3}$.

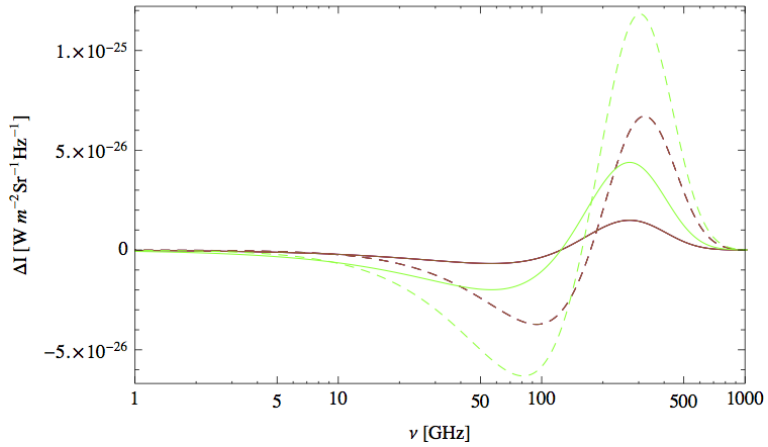

Figure 9.2: Spectrum of intermediate (dashed) and μ-type (solid) spectral distortion for the effective model of a softly turning trajectory and the same parameters as in FIG. 9.1. The spectra for these parameter sets are superimposed and actually do not significantly differ from that of a single-field trajectory with constant $n_{\rm s}$. They lead to $\mu = 5.0 \times 10^{-9}$ and $y = 5.4 \times 10^{-9}$. In the case of $\mu_{\rm iso} = 1$ (green), which corresponds to a maximal enhancement of power, i-type and μ-type distortions are respectively about two times or three times larger, but nevertheless should below the sensitivity of PIXIE ($\mu = 1.47 \times 10^{-8}$ and $y = 5.4 \times 10^{-9}$). When the enhancement is close to maximal, the generated distortions could nevertheless be detected by a PRISM-class experiment.

9.2 Suddenly turning trajectory

In the case of suddenly turning trajectories, modifications of the power spectrum of curvature perturbations are very sharp and not detectable since the duration of the turn is much less than one e-fold. However, there are two effects on the scalar power spectrum resulted by a transverse heavy field which is excited by the sudden turn and induce high-frequency field oscillations [108, 109]. One of these effects is the so-called deformation effect where the Hubble parameter is modified, whereas the other is the mixing of adiabatic and entropic modes that is called as the conversion effect. For models with canonical kinetic terms, the corresponding power spectrum is characterized by a very clear peak at the turning scale since the parametric resonance caused by the two effects exactly cancel out each other. We are interested in the situation where the power spectrum is enhanced on the distortion scales and remains unaffected prior to the turn. Therefore, we employ the analytical approximation [109]

$$\mathcal{P}_\zeta(k) = \mathcal{P}^0_\zeta(k)\left[1 + \mu_{\rm iso}\alpha^2\frac{(\sin x_t - x_t\cos x_t)^2}{x_t^3}\right] , \tag{9.3}$$

where $x_t \equiv k/k_t$, $\mu_{\rm iso} \equiv \sqrt{m^2_{\rm iso}/H^2 - 9/4}$ and α is the angle of sudden turn in the field space. The mode k_t exit the horizon at the time N_t during the turn. This formula is valid for the heavy isocurvature mass cases where $m_{\rm iso} \gtrsim 10H$.

The behaviour of the function $f(x_t) \equiv (\sin x_t - x_t\cos x_t)^2/x_t^3$ is illustrated in FIG. 9.3. It reaches the maximum at $x_t \simeq 2.46$ with $f(2.46) \simeq 0.43$, then damped with a series of oscillations. The frequency of the oscillations in the power spectrum is fixed by the model, whereas their amplitude is controlled by $\mu\alpha^2$. Serval examples are represented in Fig. 9.4 for the scales of CMB distortions. Note that important deviations from Eq. (9.3) would be shown by a full numerical analysis after a few oscillations [109, 114, 115]. However, those deviations do not affect the signal of distortion that mostly comes from the first three oscillations. In fact, even if one cuts the oscillations in scalar spectrum after three or four oscillations, the distortion spectrum changes only at the percent level.

Due to the oscillatory behaviour of the scale power spectrum, Eq. (7.3) which assumes a power-law shape with a nearly unity spectral index, is no longer applicable. We have to employ the expected sensitivity of PIXIE which is given by Eq. (7.2). The distortion spectra is represented in Fig. 9.5. One can observe that for the case $\mu_{\rm iso}\alpha^2 \sim 10^2$, the signal of distortion is observable at 5σ confidence level, whereas the case of $\mu_{\rm iso}\alpha^2 \sim 10$ cannot give rise to a detection at more than about 2σ. Therefore, for angles $\alpha \lesssim \pi/2$, it requires

$$m_{\rm iso} \gtrsim \mathcal{O}(100)H \tag{9.4}$$

for leading to a detectable level of CMB distortions. Moreover, the turn should be initiated at the distortion scales. We notice that the level of intermediate distortions is greater than that of the μ-type. This is because of the damping of the oscillations in the spectrum, which reduces the smallest scales contribution to the distortion signal. Note that the ratio between μ-type and i-type distortions also depends on the turning scales.

In conclusion, if the bound of Eq. (9.4) is satisfied and if the turn occurs at about 50-55 e-folds before the end of inflation, the signal of CMB distortion from sudden turn-

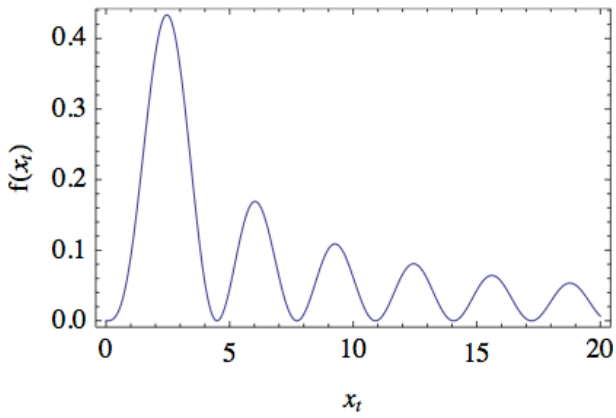

Figure 9.3: Function $f(x_t)$.

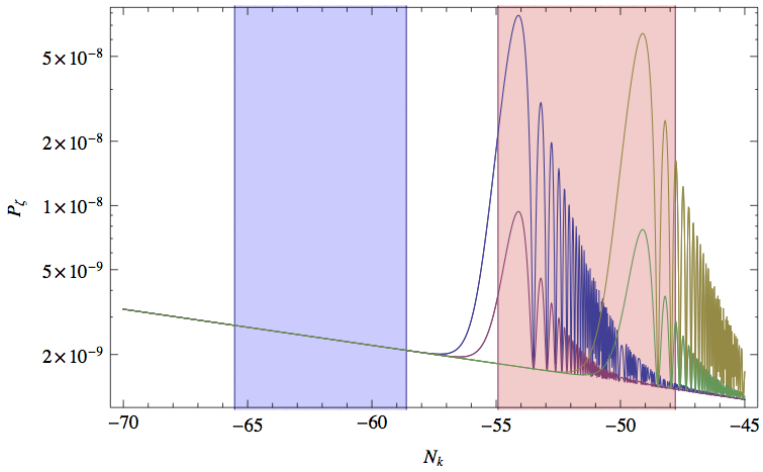

Figure 9.4: Amplitude of Power spectrum of curvature perturbations as a function of horizon the exit time, for suddenly turning trajectories, with $N_t = 55$ (blue and red curves) and $N_t = 50$ (yellow and green curves), and for $\mu_{\rm iso}\alpha^2 = 100$ (blue and yellow) and $\mu_{\rm iso}\alpha^2 = 10$ (red and green).

ing trajectories is observable with PIXIE. For a PRISM-class experiment, the bound of Eq. (9.4) can be reduced by about one order of magnitude.

9.3 Mild waterfall trejectory

As we discussed in part I, the hybrid inflation with a mild waterfall phase which lasts more than 60 e-folds is disfavoured by the CMB anisotropy observations, due to the important contribution from entropic modes. In this section, we consider an intermediate case where duration of the waterfall phase is $20 \lesssim N \lesssim 60$ e-folds. Here, we employ the unified

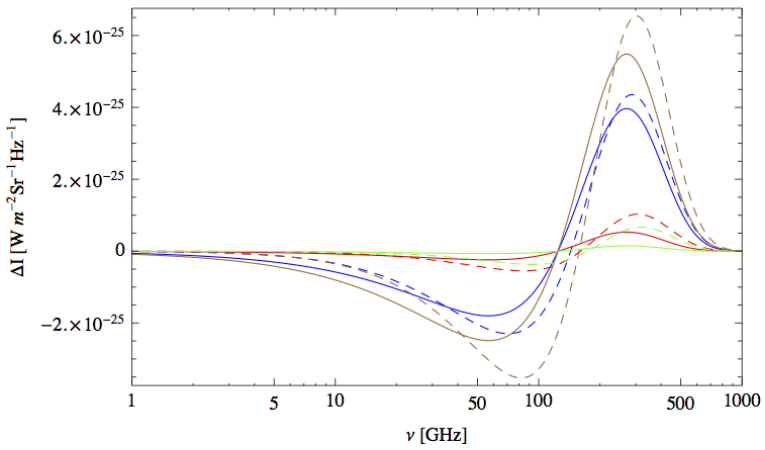

Figure 9.5: Spectrum of intermediate (dashed) and μ-type (solid) spectral distortions for the effective model of a sudden-turning trajectory, and same parameter values as in FIG. 9.4. The spectra corresponding to $\mu_{\rm iso}\alpha^2 = 100$ is detectable by PIXIE at more than 5σ, whereas in the two other cases they reach no more than the 2σ level.

potential for F-term and D-term models, which reads

$$V(\phi,\psi) = \Lambda\left[\left(1-\frac{\psi^2}{M^2}\right)^2 + \frac{\phi}{\mu} + \frac{2\phi^2\psi^2}{\phi_{\rm c}^2 M^2}\right] , \tag{9.5}$$

where as in Eq. (2.15), the global minima locates at $\psi = \pm M$ and $\phi = 0$, and $\phi_{\rm c}$ is the position of critical instability point. Then, we look for a region of the parameter space where the scale power spectrum is in agreement with observations on CMB anisotropy scales, and enhanced by more than one order of magnitude (which leads to a detectable level of CMB distortions) on distortion scales.

As we know from chapter 5, the dynamics in phase 2 can be described as effective single field theory. Therefore, we focus on the case where the horizon exit occurs in phase 1. In this case, the analytical approximation of the amplitude of scale power spectrum is given by

$$\mathcal{P}_\zeta(k) \simeq \frac{\Lambda M^2 \mu \phi_{\rm c}}{192\pi^2 M_{\rm pl}^6 \chi_2 \psi_k^2} , \tag{9.6}$$

where ξ and χ are defined as $\phi = \phi_{\rm c}\exp(\xi) \simeq \phi_{\rm c}(1+\xi)$ and $\psi = \psi_0\exp(\chi)$. As in part I, the phase 1 connects to phase 2 at the point (ξ_2, χ_2) with

$$\chi_2 \equiv \ln\left(\frac{\phi_{\rm c}^{1/2} M}{2\mu_1^{1/2}\psi_0}\right) . \tag{9.7}$$

For mode k exit the horizon in phase 1, one can obtain the relations

$$\xi_k = -M_{\rm pl}^2(N_k + N_2)/(\mu_1\phi_{\rm c}) \tag{9.8}$$

$$\chi_k = 4\phi_{\rm c}\mu_1\xi_k^2/M^2 , \tag{9.9}$$

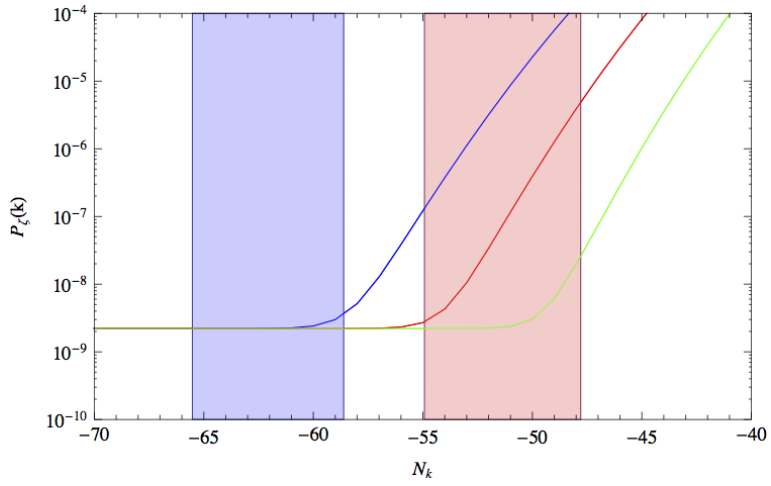

Figure 9.6: Power spectrum for curvature perturbations of the mild waterfall model, with $\Pi = 250/300/350$ (respectively green, red and blue lines).

by solving the slow-roll dynamics. Besides, the quantum stochastic fluctuations of the waterfall field at the critical point reads

$$\sqrt{\langle \psi_0^2 \rangle} = \left(\frac{\Lambda \sqrt{2\phi_c \mu_1} M}{96\pi^{3/2}} \right)^{1/2} . \tag{9.10}$$

The duration of phase 2 can be approximately written as

$$N_2 = -\frac{M^2}{8M_{\rm pl}^2 \sqrt{C}} \left[\arctan\left(\frac{\xi_{\rm end}}{\sqrt{C}} \right) - \arctan\left(\frac{\xi_2}{\sqrt{C}} \right) \right] , \tag{9.11}$$

with $C \equiv -xi_2^2 + \psi_0^2 \exp[2\chi_2]/(2\phi_c^2)$ and $\xi_{\rm end} = -M^2/(8M_{\rm pl}^2)$.

Assembling all these ingredients, the power spectrum of curvature perturbations now can be calculated. Note that for the modes leave the particle horizon a few e-folds before the critical point is reached, Eq. (9.6) is also applicable, since these super-horizon modes are still affected by entropic perturbations from the phase 1 of the waterfall. Also note that the amplitude of the power spectrum is determined by the combination of the parameters $\Pi \equiv M(\phi_c \mu_1)^{1/2}/M_{\rm pl}^2$. For various values of Π, the amplitude of scalar power spectrum is presented in Fig. 9.6. We find that the power spectrum can be significantly increased on CMB distortion scales within the range

$$250 \lesssim \Pi^2 \lesssim 350 , \tag{9.12}$$

while it keeps a nearly scale invariant amplitude on CMB anisotropy scales. The resulting spectral distortions have been plotted in FIG. 9.7. We find that given the bound Eq.s (7.2) and (7.3), this enhancement give rise to a detectable signal at about 2σ of confidence level by the PIXIE experiment.

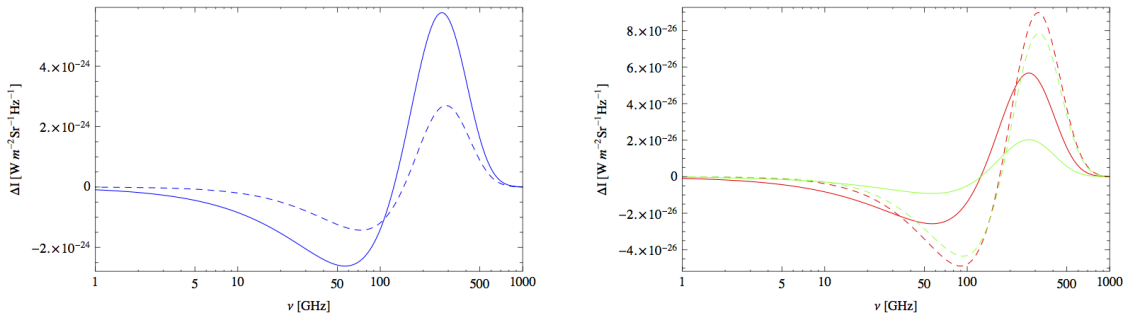

Figure 9.7: Spectrum of intermediate (dashed) and μ-type (solid) spectral distortion for the mild waterfall model, with $\Pi = 350$ (left panel), $\Pi = 300$ (right panel, red line) and $\Pi = 250$ (right panel, green line). In the first case the signal cannot be observed, whereas the latter two cases are detectable by PIXIE at about 2σ level. These parameter sets lead respectively μ-type and y-type distortions at the level $\mu = 1.93 \times 10^{-6}, 1.90 \times 10^{-8}, 6.79 \times 10^{-9}$ and $y = (6.64, 5.32, 5.32) \times 10^{-9}$.

Chapter 10

Testing a curvaton model with CMB distortions

The curvaton scenario is another way to generate a red tilted spectrum on the largest CMB angular scales, and a blue tilted spectrum on the smaller scales. For a massive curvaton, small scale modes experience less damping after the horizon exit than that of larger scales. Thus, a blue spectrum is expected. In order to satisfy all criteria from Sect. 8.1, we assume that the mass of curvaton is of order (but somewhat blow) the Hubble parameter and that the curvaton spectrum dominant over the inflaton spectrum at the scale $k_{\rm d} = 42{\rm Mpc}^{-1}$, but it is subdominant for $k_{\rm p} = 0.05{\rm Mpc}^{-1}$. The mass of curvaton can be considered as a dynamical, Hubble-induced mass.

The massive curvaton still satisfies Klein-Gordon equation with normalized solutions for its momentum modes read

$$\sigma(\mathbf{k}_{\rm c}, \eta) = -H_* \eta \sqrt{\frac{\pi\eta}{4}} H_\nu^{(1)} \left(-|\mathbf{k}_{\rm c}|\eta\right) , \tag{10.1}$$

where

$$\nu = \sqrt{\frac{9}{4} - \frac{m_\sigma^2}{H_*^2}} . \tag{10.2}$$

Here, the comoving momentum $\mathbf{k}_{\rm c} \equiv a\mathbf{k}$, where $\mathbf{k}$ is the physical momentum. Moreover, the Hubble parameter H_* is considered as a constant during inflation, which is always valid for small-field models. At the end of inflation, the power spectrum of curvaton perturbations is given by

$$\mathcal{P}_{\delta\sigma}(\mathbf{k}, t_{\rm end}) = \frac{|\mathbf{k}_{\rm c}|^3}{2\pi^2} \sigma^2(\mathbf{k}_{\rm c}, \eta_{\rm end}) = \frac{|\mathbf{k}|^3}{8\pi H} \left| H_\nu^{(1)}(|\mathbf{k}|/H) \right|^2 \approx \frac{H^2}{4\pi^2} \left(|\mathbf{k}|/H\right)^{3-2\nu} , \tag{10.3}$$

where $t_{\rm end}$ denotes the comoving time of the end of inflation. Before the curvaton oscillation start, the power spectrum is damped

$$\mathcal{P}_{\delta\sigma}(\mathbf{k}, t) = \mathcal{P}_{\delta\sigma}(\mathbf{k}, t_{\rm end}) {\rm e}^{-\int\limits_{t_{\rm end}}^{t} dt \frac{2m^2}{3H}} , \quad \text{for} \quad t_{\rm end} < t < t_{\rm osc} , \tag{10.4}$$

where $t_{\rm osc}$ is the comoving time where $H \approx m_\sigma$ and the oscillation of the curvaton field start. Similarly, the background curvaton evolves as

$$\sigma(t) = \sigma(t_{\rm end}) {\rm e}^{-\int\limits_{t_{\rm end}}^{t} dt \frac{m^2}{3H}} , \quad \text{for} \quad t_{\rm end} < t < t_{\rm osc} . \tag{10.5}$$

In sudden decay approximation, the curvaton finally decays at the time $t_{\rm dec}$, and contributes to the cosmic fluid as a fraction $\Omega_{\sigma{\rm dec}}$ of the critical density. The power spectrum of curvature perturbations caused by curvaton can be computed by the δN formalism [74, 116] which gives

$$\begin{aligned}\mathcal{P}_{\zeta_\sigma}(\mathbf{k}) =&\mathcal{P}_{\delta\sigma}(\mathbf{k},t_{\rm osc})\frac{4}{9}\Omega^2_{\sigma{\rm dec}}\left(\frac{1}{\sigma(t_{\rm osc})}\right)^2=\mathcal{P}_{\delta\sigma}(\mathbf{k},t_{\rm end})\frac{4}{9}\Omega^2_{\sigma{\rm dec}}\left(\frac{1}{\sigma(t_{\rm end})}\right)^2 \\ \approx&a_\sigma\left(\frac{|\mathbf{k}|}{k_{\rm pivot}}\right)^{n_{\rm s}^{(\sigma)}-1},\end{aligned} \tag{10.6}$$

where

$$a_\sigma=\frac{H_*^2}{9\pi^2\sigma^2(t_{\rm end})}\Omega^2_{\sigma{\rm dec}}\left(\frac{k_{\rm pivot}}{H_*}\right)^{3-2\nu}. \tag{10.7}$$

Note that the additional damping of the curvaton field after inflation [Eqs. (10.4,10.5)] is canceled in this expression. In addition, provide $H_*\gtrsim m_\sigma$, the epoch of damping is not quantitatively important, since the curvaton oscillations begin soon after the end of inflation. Thus, a strong blue tilted curvature power spectrum can be obtained.

In general, the inflaton induced curvature power spectrum can be parameterized as

$$\mathcal{P}_{\zeta{\rm inf}}(\mathbf{k})=a_{\rm inf}\left(\frac{|\mathbf{k}|}{k_{\rm pivot}}\right)^{n_{\rm s}^{({\rm inf})}-1}. \tag{10.8}$$

The total spectrum of curvature perturbations is given by adding up contributions from inflaton and curvaton linearly [116], which reads

$$\mathcal{P}_\zeta(\mathbf{k})=\mathcal{P}_{\zeta{\rm inf}}(\mathbf{k})+\mathcal{P}_{\zeta_\sigma}(\mathbf{k})\,. \tag{10.9}$$

In the context of CMB distortions, we can treat the amplitude and tilt of the power spectrum as free parameters. Note that the level of non-Gaussianity depends on the fraction $\Omega_{\sigma{\rm dec}}$ by [116] $\frac{3}{5}f_{\rm NL}=\frac{3}{4}(\mathcal{P}_{\zeta\sigma}/\mathcal{P}_\zeta)^2/\Omega_{\sigma{\rm dec}}$. Thus, one cannot tune a_σ by adjusting the value of $\Omega_{\sigma{\rm dec}}$ deliberately. However, the value of a_σ can be adjusted by changing $\sigma(t_{\rm end})$ through initial conditions. In addition to criteria from Sect. 8.1, the strongly enhanced scalar spectrum should also consistent with the constraints from ultracompact minihalos (UCMHs) [117] and primordial black holes (PBHs) [118].

The bound from UCMHs is [117]

$$\mathcal{P}_\zeta(|\mathbf{k}_{\rm UCMH}|)<\mathcal{P}_{\rm UCMH}\,, \tag{10.10}$$

where

$$\mathcal{P}_{\rm UCMH}\approx 5\times10^{-8}\quad\text{and}\quad|\mathbf{k}|_{\rm UCMH}\approx 5\times10^7{\rm Mpc}^{-1}\,. \tag{10.11}$$

The scale $|\mathbf{k}|_{\rm UCMH}$ corresponds to $N_{\rm e}^{\rm UCMH}\approx 21$ after the horizon exit of pivot scale $k_{\rm p}$. Since the power spectrum of curvature perturbations is dominated by the blue-tilted curvaton spectrum on the scales around $|\mathbf{k}|\approx|\mathbf{k}_{\rm UCMH}|$, constraints from UCMHs on larger scales are fulfilled spontaneously provide the lation (10.10) is satisfied.

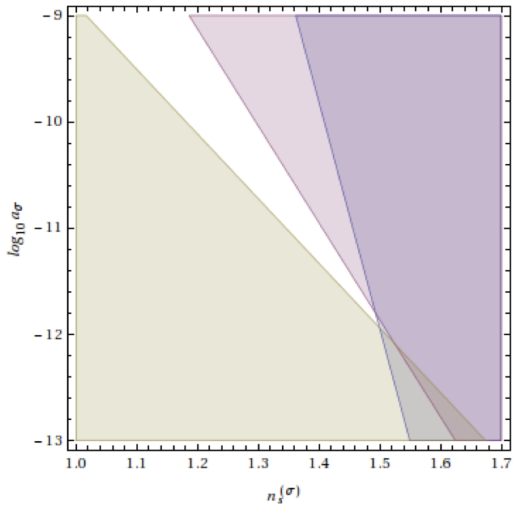

Figure 10.1: Constraints on a_σ and $n_{\rm s}^{(\sigma)}$. The blue region is excluded due to the non-observation of PBHs, relation (10.12), the red region is excluded due to constraints from UCMHs, relation (10.10). Above the brown region, the power spectrum from the curvaton is comparable or larger than the power spectrum from inflaton at the smallest scales relevant for CMB distortions, which is more precisely stated by relation (10.13). The white region therefore indicates the parameter space that is of interest in view of future observations of CMB distortions.

Similarly, the constraint from PBHs is [118]

$$\mathcal{P}_\zeta(|\mathbf{k}|) < \mathcal{P}_{\rm PBH}\,, \quad \text{where} \quad \mathcal{P}_{\rm PBH} \approx 5 \times 10^{-2}\,. \tag{10.12}$$

This constraint works for all scales that exit the Hubble horizon during inflation. Again, because of the blue-tilted power spectrum on small scales, one need only to fulfill the constraints on the smallest scales. Here, we take the scale around $N_{\rm e}^{\rm PBH} \approx 50$ e-folds after the horizon exit of anisotropy pivot scale.

The constraints (10.10,10.12) are illustrated in FIG 10.1. Assuming $n_{\rm s}^{(\rm inf)} = 0.96$, the region for

$$\mathcal{P}_{\zeta_\sigma} = \mathcal{P}_{\zeta \rm inf} \tag{10.13}$$

at the smallest CMB distortions scale ($N_{\rm e} \approx 14$ e-folds after the horizon exit of the pivot scale $k_{\rm p}$) is identified. For three parameter sets in the allow region from FIG 10.1, the total power spectrum of curvature perturbations and the resulting CMB distortions have been plotted in FIG. 10.2 and FIG. 10.3 respectively. Then, we find that the level of CMB spectrum distortions is not observable by PIXIE after imposing the Planck constraints. Nonetheless, for a PRISM-class experiment, we employ a MCMC analysis with fiducial values $a_\sigma = 0$, $n_s^{(\rm inf)} = n_s(k_{\rm p})$ and $\mathcal{P}_{\zeta \rm inf}(k_{\rm p}) = \mathcal{P}_\zeta(k_{\rm p})$ are given by the central values of Planck from Eq. (8.3), and $y_{\rm re} = 4 \times 10^{-7}$, $\Delta^* = 0$. The projected bounds on a_σ, ϱ is presneted in FIG. 10.4, where $\varrho = a_\sigma / a_{\rm inf}$. One can find that a 60% contamination of the scalar perturbations from a curvaton with a blue spectrum, can be ruled out by a PRISM-class probe at 95% C.L.

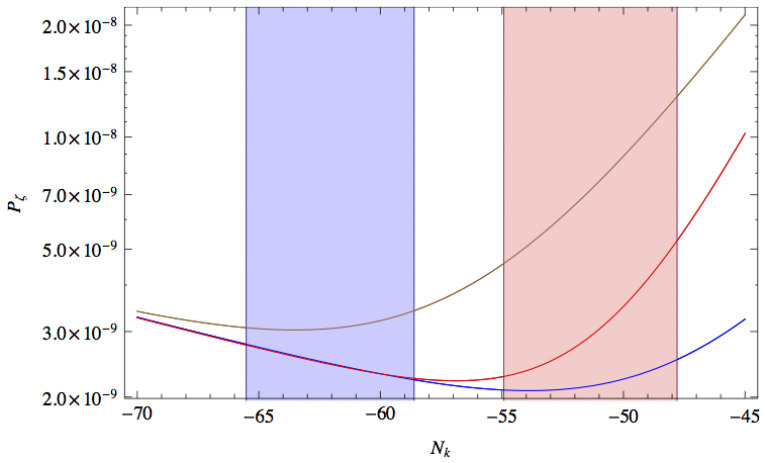

Figure 10.2: Power spectrum of curvature perturbations for the curvaton scenario, for three parameter sets in the white region of FIG. 10.1: $\log_{10} a_\sigma = -10$, $n_s^\sigma = 1.2$ (blue), $\log_{10} a_\sigma = -10$, $n_s^\sigma = 1.3$ (red) and $\log_{10} a_\sigma = -9$, $n_s^\sigma = 1.2$ (brown).

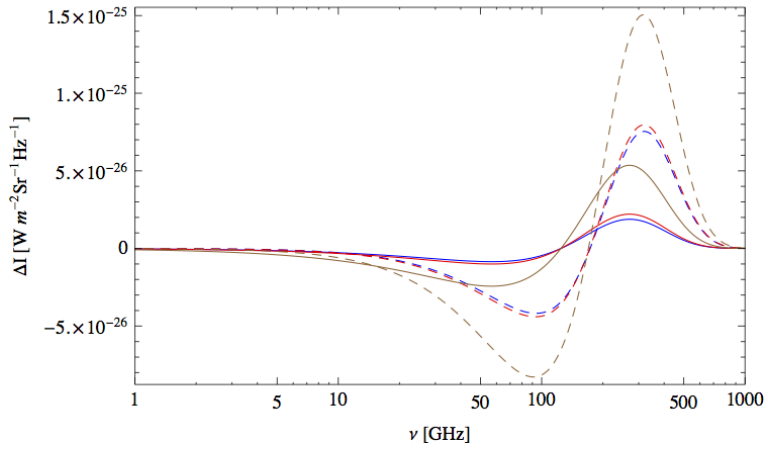

Figure 10.3: Spectrum of intermediate (dashed) and μ-type (solid) spectral distortion for the curvaton model and same parameter values as in FIG. 10.2.

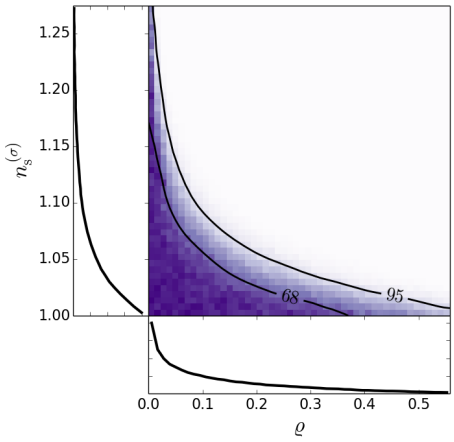

Figure 10.4: Projected exclusion bounds on the curvaton model from a PRISM-class experiment.

Conclusion

In this part, we have briefly reviewed on different types of CMB spectral distortions and the expected sensitivities for the future PIXIE and PRISM-class experiments. Then, an exhaustive model-oriented analysis was performed for inflation in scope of μ-type and intermediate i-type CMB distortions which are caused by energy injection to the primeval plasma from the dissipation of acoustic waves before the epoch of recombination. The y-type distortions are not of interest, since it is dominated by other sources which are produced in the stage posterior to recombination, such as the thermal SZ effect. We found that only few models can give rise to an observable level of CMB distortions for the PIXIE experiment.

For all 49 single-field modes listed in Ref. [27], only one of them can induce a power spectrum of curvature perturbations satisfying the Planck constraints on the CMB anisotropy scales and getting sufficiently enhanced at the distortion scales simultaneously. This model is the original hybrid inflation in the valley with a super-Planckian inflaton field. When inflation proceeds from the field dominated regime towards the false vacuum dominated regime, a blue spectrum at smaller scales is generally predicted. However, we found that the region of parameter space inducing a power spectrum satisfies all criteria in Sect. 8.1 simultaneously need to be fine-tuned. Nevertheless, the situation can be greatly improved for a PRISM-class experiment with the sensitivity ten time higher than PIXIE. In principle, the PRISM experiment can detect the signal of CMB distortions from models with a large running of spectral index which causes a substantial change in power between anisotropy and distortions scales, for example the Non-Canonical Kähler and the Running Mass inflation models.

In addition, we have examined three effective multi-field inflation scenarios: a softly turning, a suddenly turning and a mild waterfall trajectory. We found that the latter two scenarios can generate CMB distortions at a level to be probed by PIXIE. In the cases of suddenly turning trajectories, the scalar power spectrum develops a peak and then experiences damping oscillations at a scale close to the turn. Only if the turn is initiated at the scales of CMB distortions, a detectable signal of distortion can be generated. For the hybrid models with a mild waterfall phase, a peak in the power spectrum of curvature perturbations was shown to emerge. We focused on the case with the duration of the waterfall phase of about 40 e-folds and determined the parameter range which generate an observable signal of CMB distortions for the PIXIE experiment. Besides, distortions induced by trajectories with a soft turning can be still detectable by a PRISM-class experiment in a tuned region of parameter space. Moreover, we remark that one can distinguish different models by the ratio between μ-type and i-type distortions.

Finally, we tested the curvaton scenarios where the blue spectrum from massive curvaton is dominant at distortion scales and subdominant at anisotropy scales. Imposing the constraints from the ultra compact minihalos, we found that curvaton scenarios cannot lead to a detectable level of CMB spectral distortion for the PIXIE experiment. However, a PRISM-class experiment can be used to constrain its parameter space in the context of

CMB distortions.

From our analysis, one can find that only very few inflation models with fine-tuned parameter sets can induce detectable CMB distortion signals for the future experiments. Even if μ- or i-type distortions are discovered in the future, one might still need to consider other potential sources such as energy injection from evaporation of primordial black holes or decay/annihilation of relic particles.

Part III

Infrared correlation in de Sitter space: field theoretic vs. stochastic approach

Contents

Introduction

In the previous two parts, the field and curvature perturbations are investigated at the linear order, which coincide with the sensitivity of recent CMB anisotropy experiments. The effects of loop corrections have not yet been observed. Nonetheless, these are at least of conceptual interest, and they may leave signatures observable *e.g.* by future observations of 21 cm radiation in the high redshift region ($z \sim 50$) [119]. But, perturbation theory breaks down due to IR effects for some important special cases, such as for massless scalar fields or arguably for gravitons. For simplicity, people usual consider loop corrections to field perturbations in a pure de Sitter spacetime, where the duration of inflation is infinite. On a de Sitter background, quantum fluctuations of a free massless scalar field which couples to gravitation minimally feature a IR divergence due to the redshift of k-modes of the field [120]. The deeper reason is that the Bunch-Davies vacuum, which is commonly used, is not de Sitter invariant, and a de Sitter invariant vacuum is missing [121, 122]. However, the situation may changed for an interaction scalar field theory.

The first resummation of quantum fluctuations of a scalar field on de Sitter background has been done by Starobinsky and Yokoyama [123, 124] with the stochastic approach. In this approach, the short-wavelength modes are treated as a stochastic noise to the horizon-size modes which are approximately considered as classical. For a massless ϕ^4 theory, the resummation of contribution from all loop orders which gives a finite IR correlation indicates the IR divergence should be self-regulatory. In addition, the author derives an invariant quantum state to leading IR order for massless ϕ^4 theory in Euclidean de Sitter space in Ref. [125]. It is confirmed in Ref. [126] with a loop expansion and the necessary resummation. Moreover, it argues that the Euclidean quantum field theory (QFT) result agrees with the result from stochastic approach for scalar fluctuations in Lorentzian de Sitter space [123, 124]. A similar agreement is pointed out for the propagators between Euclidean and Lorentzian de Sitter space in Ref. [127]. Nevertheless, beyond the leading IR approximation, the massive field correlations for large separations on the Euclidean de Sitter background are characterized by an exponentially decaying behaviour [128, 129]. However, for the massless case, this decay behaviour cannot be confirmed yet [130].

Therefore, people might ask several questions for the quantum field theory (QFT) on Lorentzian background: i) Do the field correlations decay at large distance? ii) The IR divergence is self-regulatory or not? iii) What is the role of the stochastic approximation in a full QFT calculation? etc. To answer these questions, one usually employ the CTP formalism [131, 132] as an appropriate tool in the QFT framework. In this formalism, the field evolves both forward and backward in time. Thus, we also refer to it as Amphichronous QFT. With the Amphichronous QFT, many work have been done with a wide range of methods, such as ordinary perturbation theory [133, 134, 135, 136, 137, 138, 139, 140], the Hartree-Fock method [141, 142, 143] ,a large N expansion in O(N)-symmetric theories [144, 145, 146, 147, 148, 138], the Wigner-Weisskopf method [149], functional renormalisation group techniques [150] or other partial resummation schemes [151]. However the non-perturbative resummation, which is readily performed in the Stochastic approach,

does not appear to be recovered by these approaches.

In this part, we try to answer above-mentioned question with the ϕ^4 theory which has been most widely studied. The Lagrangian is given by

$$\mathcal{L} = \sqrt{-g}\left[\frac{1}{2}g^{\mu\nu}(\partial_\mu\phi)(\partial_\nu\phi) - V(\phi)\right], \tag{10.14}$$

with the potential

$$V(\phi) = \frac{1}{2}m^2\phi^2 + \frac{\lambda}{4!}\phi^4\,. \tag{10.15}$$

where m is the mass of scaler field. The scalar field minimally couples to gravitation through the metric. In order to obtain significant IR enhancement for superhorizon modes, we restrict that the mass of field is much smaller than the Hubble parameter, *i.e.* $m^2 \ll H^2$. Moreover, we focus on a 4-dimensional spacetime with metric in global and conformal coordinates reads [152]

$$ds^2 = dt^2 - a^2(t)(dx^2 + dy^2 + dz^2) = a^2(\eta)(d\eta^2 - dx^2 - dy^2 - dz^2), \tag{10.16}$$

where the scale factor a of spacetime is given by $a = -1/(H\eta) = \exp(Ht)$. A de Sitter invariant length function is defined as [133, 153]

$$y(x;x') = a(\eta)a(\eta')H^2\Delta x^2 = \frac{\Delta x^2}{\eta\eta'} = -4sin^2\left(\frac{1}{2}H\ell(x;x')\right), \tag{10.17}$$

where $\Delta x^2 = (\eta-\eta')^2 - (\mathbf{x}-\mathbf{x}')^2$, $\mathbf{x}$ is the spatial-vector. The length ℓ along geodesic can be purely imaginary for a time-like separation $y > 0$, be real for a space-like separation $-4 < y < 0$, and be complex for a separation cannot connect by geodesics.

With the above setup, this part is organized as following: In chapter 11, we have a brief review on the Fokker-Planck method that is used by Starobinsky and Yokoyama to resum leading IR fluctuations. Besides, we develop a diagrammatic expansion for the stochastic method based on the Langevin equation. In chapter 12, based on the first principle of QFT, we extract the leading IR behaviours from the propagators of the scalar field and show the agreement on diagram contributions between both stochastic and field theoretic approaches up to two loops order. Then, the equivalence between field theoretical and stochastic diagrams at leading IR order is proved in chapter 13 up to all orders. The resummation in chapter 14 gives the same result as in Refs. [123, 124]. Finally, we summarize out results and possible implications in the Conclusions.

Chapter 11

Stochastic approach

In the stochastic approach [123, 124], the scalar field ϕ can be divided into a long wavelength part $\bar{\phi}$ and a short wavelength part respect to a IR cutoff $\epsilon a(t)H$, as following

$$\phi(\mathbf{x},t) = \bar{\phi}(\mathbf{x},t) + \int \frac{d^3k}{(2\pi)^{3/2}}\theta(|k| - \epsilon a(t)H)\left[a_{\mathbf{k}}\phi_{\mathbf{k}}(t)e^{-i\mathbf{k}\cdot\mathbf{x}} + a^{\dagger}_{\mathbf{k}}{\phi_{\mathbf{k}}}^{*}(t)e^{i\mathbf{k}\cdot\mathbf{x}}\right], \quad (11.1)$$

where $\theta(z)$ is a Heavi-side function, $\epsilon \ll 1$ is a small constant, and $\phi_{\mathbf{k}}(t)$ are free mode functions for ϕ. The long wavelength part of the field can be treated as a classical field [154, 155], whereas the short wavelength part is quantum.

From the Klein-Gordon equation $\Box\phi + \frac{\partial V}{\partial\phi} = 0$, one can obtain the Langevin equation for the long wavelength part $\bar{\phi}$ [56]

$$\dot{\bar{\phi}} + \frac{1}{3H}\frac{\partial V(\phi)}{\partial\phi} = \xi(t), \quad (11.2)$$

where $\xi(t)$ is a Gaussian stochastic noise which satisfies

$$\langle\xi(t)\rangle = 0, \quad \text{and} \quad \langle\xi(t)\xi(t')\rangle = \frac{H^3}{4\pi^2}\delta(t-t'). \quad (11.3)$$

11.1 Fokker-Planck equation and the IR correlation

With the Langevin equation (11.2), one can derive the Fokker-Planck equation by defining the one-point probability distribution function (PDF) for long wavelength part $\bar{\phi}$ as

$$P(\chi,t) \equiv \left\langle\delta(\chi - \bar{\phi})\right\rangle. \quad (11.4)$$

Note that the PDF is time dependent. Thus, one can act with a time derivative on it and obtains

$$\begin{aligned}\frac{\partial}{\partial t}P(\chi,t) &= -\frac{\partial}{\partial\chi}\left\langle(\chi-\bar{\phi})\dot{\bar{\phi}}\right\rangle \\ &= \frac{\partial}{\partial\chi}\left(\frac{1}{3H}P(\chi,t)\frac{\partial V(\chi)}{\partial\chi}\right) - \frac{\partial}{\partial\chi}\left\langle\delta(\chi-\bar{\phi})\xi(t)\right\rangle, \end{aligned} \quad (11.5)$$

In order to obtain the second line of this equation, the Langevin equation has been substituted. Note that $\exp[-\int\frac{2\pi^2}{H^3}\xi^2(t)dt']$ is a probability distribution function of the stochastic noise term ξ. Thus, the second term of Eq. (11.5) can be written as

$$\begin{aligned}\left\langle\delta(\chi-\bar{\phi})\xi(t)\right\rangle &= \int\mathcal{D}[\xi(t')]\left\{\delta(\chi-\bar{\phi})\xi(t)\exp\left[-\int\frac{2\pi^2}{H^3}\xi^2(t')dt'\right]\right\} \\ &= -\frac{H^3}{8\pi^2}\frac{\partial}{\partial\chi}\left\langle\delta(\chi-\bar{\phi})\right\rangle. \end{aligned} \quad (11.6)$$

Substituting this equation into Eq. (11.5), one then obtains the Fokker-Planck equation for the PDF of $\bar{\phi}$ which reads,

$$\frac{\partial}{\partial t}P(\psi,t)=\frac{1}{3H}\frac{\partial}{\partial\psi}\left(P(\psi,t)\frac{\partial V(\psi)}{\partial\psi}\right)+\frac{H^3}{8\pi^2}\frac{\partial^2}{\partial\psi^2}P(\psi,t). \tag{11.7}$$

Here we denote $P(\psi,t)\equiv P[\bar{\phi}(\mathbf{x},t)]\equiv P[\phi]$. Solving this equation will give the knowledge of field evolution on the de Sitter background. In the late time limit, the field goes into a static equilibrium, while its PDF which becomes to be time independent reads [123, 124]

$$\varrho(\phi)=\mathcal{N}\mathrm{e}^{-\frac{8\pi^2}{3H^4}V(\phi)}\,, \tag{11.8}$$

where $\mathcal{N}$ is the normalization for

$$\int_{-\infty}^{\infty}d\phi\varrho(\phi)=1\,. \tag{11.9}$$

Therefore, leading IR correlation can be given by the equal time expectation value of ϕ^2 as

$$\langle\phi^2\rangle=\int_{-\infty}^{\infty}d\phi\phi^2\varrho(\phi)=\frac{3H^4}{8\pi^2m^2}-\frac{9\lambda H^8}{128\pi^4m^6}+\frac{9\lambda^2H^{12}}{256\pi^6m^{10}}+\cdots\,, \tag{11.10}$$

for the potential (10.15). This perturbative expansion is valid only if the coupling is not very strong, *i.e.* $\lambda\ll m^4/H^4$. Nevertheless, for the case where the scalar field is massless ($m\to 0$), one obtains [124]

$$\langle\phi^2\rangle=\sqrt{\frac{3}{2\pi}}\frac{\Gamma\left(\frac{3}{4}\right)}{\Gamma\left(\frac{1}{4}\right)}\frac{H^2}{\sqrt{\lambda}}\,, \tag{11.11}$$

after resuming the contribution to all loop orders. It shows that classical stochastic perturbations emerge in the inflationary universe even at late time. Furthermore, we point out that the stochastic approach can be also used to derive quantitative results [144, 156, 157, 158, 159].

11.2 Diagrammatic expansion of the correlators

Although one can obtain perturbative results from the Fokker-Planck equation like Eq. (11.10), it is not easy to get any intuition for connecting them with the QFT. A diagrammatic expansion is therefore needed. Start from the Langevin equation 11.2 with functional (path integral) techniques [160], the expectation value of an operator $\mathcal{O}[\phi]$ can be written as

$$\langle\mathcal{O}[\phi]\rangle=\int D[\xi]\mathrm{e}^{-\frac{1}{2}\int dt\xi^2\frac{4\pi^2}{H^3}}\int D[\phi]\mathcal{O}[\phi]\delta(\dot{\phi}+\partial_\phi V/3H-\xi)\mathcal{J}[\phi]\,. \tag{11.12}$$

Here $\mathcal{J}[\phi]=\left|\mathrm{Det}\left[\frac{\delta}{\delta\phi}\left(\dot{\phi}+\partial_\phi V/3H-\xi\right)\right]\right|$ is the Jacobian of the delta function with respect to the field.To evaluate the determinant, the time interval is discretized in N time

steps of extent Δt such that $\phi_i = \phi(t_i)$ and $\xi_i = \xi(t_i)$ with $i = 0, \ldots, N$. Then the determinant can be rewritten as $\mathcal{J} = |\mathrm{Det}\mathcal{J}_{ij}|$ where

$$\mathcal{J}_{ij} = \frac{\partial}{\partial \phi_j}\left(\frac{\phi_i - \phi_{i-1}}{\Delta t} + \frac{\partial_\phi V(\phi_{i-1})}{3H} - \xi_{i-1}\right). \tag{11.13}$$

Note that a retarded regularization for the operator has been chosen, *i.e.* all field ϕ and the stochastic force ξ are computed at the start of each time-step. With this choice, the diagonal elements of $\mathcal{J}_{ij}$ are $\mathcal{J}_{i,i} = \frac{1}{\Delta t}$ and the only other non-zero elements are the $\mathcal{J}_{i,i-1}$ entries. Note that the $\frac{1}{\Delta t}$ factors can be absorbed into the measure $D[\xi]$ with an appropriate normalization. Thus, we obtain that $\mathcal{J}[\phi] = 1$. Furthermore, the partition function is given by

$$\mathcal{Z} \equiv \int D[\xi] \mathrm{e}^{-\frac{1}{2}\int dt \xi^2 \frac{4\pi^2}{H^3}} \int D[\phi] \delta(\dot{\phi} + \partial_\phi V/3H - \xi) = 1\,. \tag{11.14}$$

By introducing an auxiliary field ψ and integrating out the noise ξ, it can be rewritten as

$$\mathcal{Z} = \int D[\phi] D[\psi] \mathrm{e}^{-\int dt \left\{ \frac{\mathrm{i}}{H^2}\psi\left(\dot{\phi} + \frac{\partial_\phi V}{3H}\right) + \frac{1}{8\pi^2 H}\psi^2 \right\}}. \tag{11.15}$$

Then, with the potential (10.15), we rewrite the above equation in a more symmetric form

$$\begin{aligned} \mathcal{Z} &= \int D[\phi] D[\psi] \mathrm{e}^{-\mathrm{i}\int dt \left\{ \frac{1}{2}\begin{pmatrix}\phi, & \psi\end{pmatrix} \begin{pmatrix} 0 & \frac{1}{H^2}(-\partial_t + \frac{m^2}{3H}) \\ \frac{1}{H^2}(\partial_t + \frac{m^2}{3H}) & -\frac{i}{4\pi^2 H} \end{pmatrix} \begin{pmatrix}\phi \\ \psi\end{pmatrix} + \frac{\lambda}{3!}\frac{\psi\phi^3}{3H^3} \right\}} \\ &\equiv \int D[\phi] D[\psi] \mathrm{e}^{-\mathrm{i}\int dt \left\{ \frac{1}{2}\begin{pmatrix}\phi, & \psi\end{pmatrix} \mathbb{G}_0^{-1} \begin{pmatrix}\phi \\ \psi\end{pmatrix} + \frac{\lambda}{3!}\frac{\psi\phi^3}{3H^3} \right\}}, \end{aligned} \tag{11.16}$$

Note that $\frac{\lambda}{3!}\frac{\psi\phi^3}{3H^3}$ represents the interaction vertex in the Feynman rules. Moreover, the matrix of free propagators $\mathbb{G}_0$ is defined as

$$\mathbb{G}_0(t,t') = \begin{pmatrix} \langle\phi(t)\phi(t')\rangle & \langle\phi(t)\psi(t')\rangle \\ \langle\psi(t)\phi(t')\rangle & \langle\psi(t)\psi(t')\rangle \end{pmatrix} \equiv \begin{pmatrix} F(t,t') & -\mathrm{i}G^R(t,t') \\ -\mathrm{i}G^A(t,t') & 0 \end{pmatrix}. \tag{11.17}$$

The null entry in $\mathbb{G}_0$ is because of the non-dynamical nature of the pure auxiliary field ψ. From the relation $\mathbb{G}_0 \star \mathbb{G}_0^{-1}(t,t') = \mathbb{I}_{2\mathrm{x}2}\delta(t,t')$, we find that $G^{R,A}$ are the retarded and advanced propagators for the operator $\frac{1}{H^2}(\partial_t + \frac{m^2}{3H})$

$$G^R(t,t') = G^A(t',t) = H^2 \mathrm{e}^{-\frac{m^2}{3H}(t-t')}\Theta(t-t')\,, \tag{11.18}$$

whereas the statistical correlator $F(t,t') = \langle\phi(t)\phi(t')\rangle$ is the two-point function of ϕ

$$F(t,t') = \frac{3H^4}{8\pi m^2}\left(\mathrm{e}^{-\frac{m^2}{3H}|t-t'|} - \mathrm{e}^{-\frac{m^2}{3H}(t+t')}\right), \tag{11.19}$$

with the initial condition $F(0,0) = 0$. Note that for a massless scalar field, one obtains $F(t,t) \approx \frac{H^3}{4\pi}t$ which grows linear with time. The perturbative expansion breaks down due

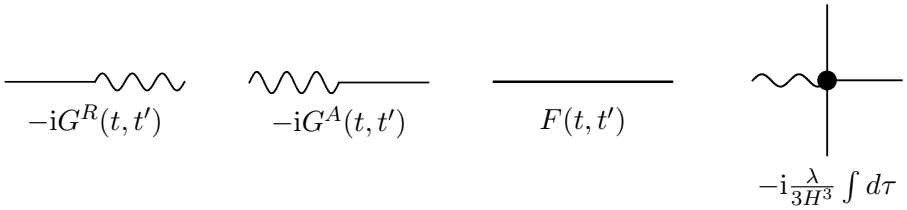

Figure 11.1: The elements of stochastic diagrams. The vertex factor is chosen for which the assembled diagrams are divided by their symmetry factor.

to this secular behaviour [120, 161, 162, 163] for large enough time in the massless limit. If the stochastic process (inflation) take place early enough, $F(t,t')$ reduces to

$$F(t,t') = \frac{3H^4}{8\pi^2 m^2}\mathrm{e}^{-\frac{m^2}{3H}|t-t'|}. \tag{11.20}$$

We discuss in further detail in chapter 14 the important massless case $m^2 = 0$. Now, we obtain a full set of Feynman rules that is presented in FIG 11.1. Thus, the diagrams contributions for the leading IR correlation can be computed perturbatively for the case where $\lambda \ll m^4/H^4$. As an example, here we calculate the contributions from Feynman diagrams up to second order that is illustrated in FIG. 11.2. The calculations are straightforward in the late time limit, which give

$$\langle\phi^2\rangle_{\mathrm{sg}} = -\lambda\frac{9H^8}{128\pi^4 m^6}\,, \tag{11.21a}$$

$$\langle\phi^2\rangle_{\mathrm{ca}} = \lambda^2\frac{27H^{12}}{2048\pi^6 m^{10}}\,, \tag{11.21b}$$

$$\langle\phi^2\rangle_{\mathrm{sgsg}} = \lambda^2\frac{27H^{12}}{2048\pi^6 m^{10}}\,, \tag{11.21c}$$

$$\langle\phi^2\rangle_{\mathrm{ss}} = \lambda^2\frac{9H^{12}}{1024\pi^6 m^{10}}\,. \tag{11.21d}$$

Summing all contributions, we obtain

$$\lim_{t\to\infty}\langle\phi(t)^2\rangle = \frac{3H^4}{8\pi^2 m^2} - \lambda\frac{9H^8}{128\pi^4 m^6} + \lambda^2\frac{9H^{12}}{256\pi^6 m^{10}}\,. \tag{11.22}$$

One may notice that this result coincides with Eq. 11.10. This coincidence implies that our diagrammatic expansion is valid at least up to two loop orders. In the next chapter, this result is also compared with the counterpart from the Amphichronous QFT method.

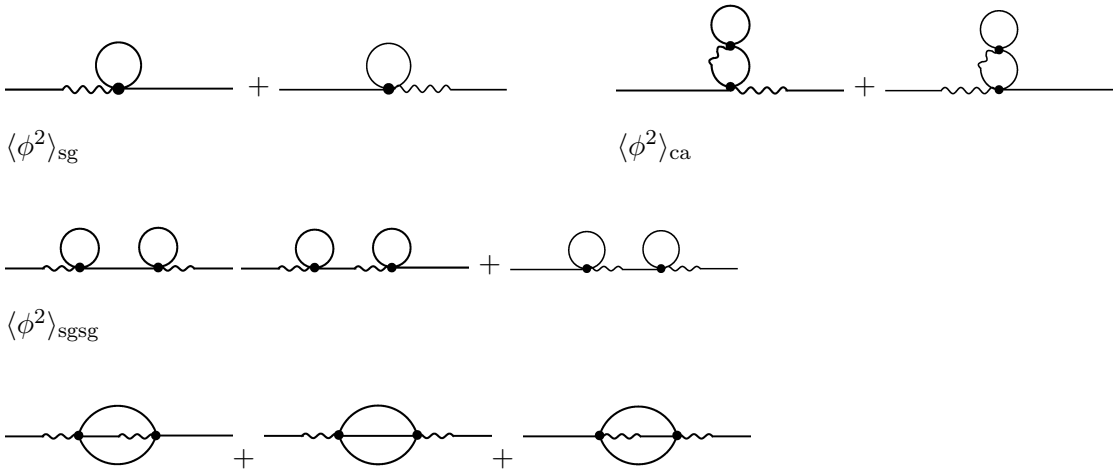

Figure 11.2: The stochastic diagrams up to two loops. Vacuum bubbles are zero by construction. Note that they are topologically identical in form to the CTP diagrams in the Keldysh basis but with the three-wiggle vertex removed. This corresponds to a semiclassical approximation. The labels refer to the topology of the diagrams: seagull, cactus, double seagull and sunset.

Chapter 12

Field theoretic approach

12.1 Basic setup

As we stated, the IR correlation can be also evaluated by an Amphichronous QFT approach. In this framework, the Amphichronous time evolves both forward and backward, and finally returns to the initial time [131, 132]. When the field corresponds to the forward (backward) branch, we denote it as ϕ_+ (ϕ_-). The free propagators are given by solving the Klein-Gordon equation

$$a^4\left(\nabla_x^2 - m^2\right)\mathrm{i}\Delta^{(0)fg}(x;x') = fg\delta^{fg}\,\mathrm{i}\delta^4(x-x')\,, \tag{12.1}$$

where $f, g = \pm$ are CTP indices and $(\nabla_x)_\mu$ is the covariant derivative with respect to x. Here, we employ the ε-prescriptions

$$\Delta x^{T^2}(x;x') = \Delta x^{++^2}(x;x') = (|\eta-\eta'| - \mathrm{i}\varepsilon)^2 - |\mathbf{x}-\mathbf{x}'|^2\,, \tag{12.2a}$$

$$\Delta x^{<^2}(x;x') = \Delta x^{+-^2}(x;x') = (\eta-\eta' + \mathrm{i}\varepsilon)^2 - |\mathbf{x}-\mathbf{x}'|^2\,, \tag{12.2b}$$

$$\Delta x^{>^2}(x;x') = \Delta x^{-+^2}(x;x') = (\eta-\eta' - \mathrm{i}\varepsilon)^2 - |\mathbf{x}-\mathbf{x}'|^2\,, \tag{12.2c}$$

$$\Delta x^{\bar{T}^2}(x;x') = \Delta x^{--^2}(x;x') = (|\eta-\eta'| + \mathrm{i}\varepsilon)^2 - |\mathbf{x}-\mathbf{x}'|^2\,, \tag{12.2d}$$

to describe the causal properties of the correlation functions. The superscripts $\pm$ are CTP indices that come from the length function (10.17). For the Amphichronous propagators, the superscript T ($\bar{T}$) denotes (anti-) time ordering, whereas the superscript $>$ ($<$) indicates that operators evaluated at the coordinate x (x') appear on the left (right) within the expression for an expectation value. In common, the propagators $\mathrm{i}\Delta^{-+}$ and $\mathrm{i}\Delta^{+-}$ are called as Wightman functions, whereas propagator $\mathrm{i}\Delta^{(0)++}$ ($\mathrm{i}\Delta^{(0)--}$) are known as (anit-)Feynman propagators. For more details on developments and cosmological applications of the Amphichronous QFT (CPT formalism), see Ref. [110, 164, 165, 166, 167, 168, 169, 170, 171].

The Klein-Gordon equation (12.1) can be expressed as a function of the length function (10.17) as

$$a^4(x)H^2\left[-4y\left(1+\frac{y}{4}\right)\frac{d^2}{dy^2} - 8\left(1+\frac{y}{2}\right)\frac{d}{dy} - \frac{m^2}{H^2}\right]\mathrm{i}\Delta^{(0)fg}(y(x;x')) = fg\delta^{fg}\mathrm{i}\delta^4(\Delta x)\,. \tag{12.3}$$

The exact solution of this equation is given by Eq. (A.1). In the IR enhanced case where $m^2 \ll H^2$, the free propagators can be approximately written as

$$\mathrm{i}\Delta^{(0)fg}(y) = \frac{H^2}{4\pi^2}\left[-\frac{1}{y^{fg}} + \frac{3H^2}{2m^2}\left(-\frac{1}{y^{fg}}\right)^{\frac{1}{3}\frac{m^2}{H^2}} + \mathcal{O}\left(y^{-2}\frac{m^2}{H^2}\right)\right]. \tag{12.4}$$

The process of approximation is shown in appendix A. We are interested in the second term in the square bracket which is IR enhanced when $m^2 \ll H^2$. With the ε-prescriptions, this term can be written as

$$\frac{3H^2}{2m^2}(-y)^{-\frac{n}{3}\frac{m^2}{H^2}} = \frac{3H^2}{2m^2}\left(1 - \mathrm{i}\frac{n}{3}\frac{m^2}{H^2}\arg(-y)\right)|y|^{-\frac{n}{3}\frac{m^2}{H^2}} + \mathcal{O}\left(\frac{m^2}{H^2}\right), \tag{12.5}$$

for the small cases where $m^2 \ll H^2$. Here, we have introduced an integer number $n \lesssim 4$ which do not change the IR properties of the free propagator, and can be considered as the powers of propagator in Feynman diagrams. Note that the power term of $|y|$ can be expanded as

$$|y|^{-\frac{n}{3}\frac{m^2}{H^2}} = 1 - \frac{n}{3}\frac{m^2}{H^2}\log|y| + \mathcal{O}\left(\left(\frac{n}{3}\frac{m^2}{H^2}\log|y|\right)^2\right). \tag{12.6}$$

This expansion indicates that all basic propagators $\mathrm{i}\Delta^{(0)++}$, $\mathrm{i}\Delta^{(0)-+}$, $\mathrm{i}\Delta^{(0)+-}$ and $\mathrm{i}\Delta^{(0)--}$ acquire a nearly constant IR-enhancement $3H^4/(8\pi^2m^2)$ for

$$|y| \ll \exp(3H^2/m^2). \tag{12.7}$$

For larger value of $|y|$, the IR-enhancement mildly decays which is crucial for regulating the vertex integrals in Feynman diagrams. Moreover, the imaginary parts of free propagators are characterized by a series of argument function of de Sitter invariant length with CTP indices that read

$$\mathrm{i}\arg(-y^{++}(x;x')) = \mathrm{i}\pi\vartheta(\Delta x^2), \tag{12.8a}$$
$$\mathrm{i}\arg(-y^{-+}(x;x')) = \mathrm{i}\pi\vartheta(\Delta x^2)\mathrm{sign}(\Delta x^0), \tag{12.8b}$$
$$\mathrm{i}\arg(-y^{+-}(x;x')) = -\mathrm{i}\pi\vartheta(\Delta x^2)\mathrm{sign}(\Delta x^0), \tag{12.8c}$$
$$\mathrm{i}\arg(-y^{--}(x;x')) = -\mathrm{i}\pi\vartheta(\Delta x^2). \tag{12.8d}$$

Until now, all the discussion works in the $\pm$ basis (or known as Wightman basis). In order to compare with the stochastic approach within statistical and advanced/retarded propagators, a transformation from the Wightman to Keldysh basis [132] is need. The transformation matrix is given by

$$U = \frac{1}{\sqrt{2}}\begin{pmatrix} 1 & 1 \\ 1 & -1 \end{pmatrix}, \tag{12.9}$$

such that the field components become

$$\begin{pmatrix} \phi \\ \psi \end{pmatrix} = U \cdot \begin{pmatrix} \phi_+ \\ \phi_- \end{pmatrix} = \frac{1}{\sqrt{2}}\begin{pmatrix} \phi_+ + \phi_- \\ \phi_+ - \phi_- \end{pmatrix}. \tag{12.10}$$

Meanwhile, the free propagators are transformed into

$$U.\begin{pmatrix} \mathrm{i}\Delta^T & \mathrm{i}\Delta^< \\ \mathrm{i}\Delta^> & \mathrm{i}\Delta^{\bar{T}} \end{pmatrix}.U^\dagger = \begin{pmatrix} \mathrm{i}\Delta^< + \mathrm{i}\Delta^> & \mathrm{i}\Delta^T - \mathrm{i}\Delta^< \\ \mathrm{i}\Delta^T - \mathrm{i}\Delta^> & 0 \end{pmatrix} \tag{12.11}$$

$$\equiv \begin{pmatrix} F(x,x') & -iG^R(x,x') \\ -iG^A(x,x') & 0 \end{pmatrix}, \tag{12.12}$$

where the retarded and advanced propagators $G^{R,A}(x,x')$ as well as $F(x,x')$ are defined in the last equality. To obtain the first equality, the CTP relation

$$\mathrm{i}\Delta^{T} + \mathrm{i}\Delta^{\bar{T}} = \mathrm{i}\Delta^{<} + \mathrm{i}\Delta^{>}\,, \tag{12.13}$$

is applied. Knowing the full expression of the free propagators in the Wightman basis, one can extract their leading order in IR enhancement, *i.e.* their leading order in H^2/m^2. Using these expressions and Eq. (12.11), it follows that, in the Keldysh basis, the free propagators can be expressed as

$$-\mathrm{i}G^{R,A}(x,x') = \mathrm{i}\Delta^{(0)R,A}(x,x') = \frac{H^2}{4\pi^2}\left(-\frac{\mathrm{i}}{2}\right)\arg y^{R,A}|y|^{-\frac{m^2}{3H^2}}\,, \tag{12.14}$$

$$F(x,x') = \mathrm{i}\Delta^{(0)>}(x,x') + \Delta^{(0)<}(x,x') = \frac{3H^4}{4\pi^2 m^2}|y|^{-\frac{m^2}{3H^2}}\,, \tag{12.15}$$

where the retarded/advanced argument function of y is given by

$$\arg y^{R}(x,x') = \arg y^{A}(x',x) = 2\pi\vartheta(\eta-\eta')\vartheta((\eta-\eta')^2 - (\mathbf{x}-\mathbf{x}')^2)\,. \tag{12.16}$$

Note that as $m \to 0$, the statistical function exhibit an IR divergence. Note also that propagators decay for large separations *i.e.* large value of y. However, as the mass of field $m \to 0$, the decay of IR fluctuation can be slow enough to break down the perturbation expansion.

For the diagrammatic expansion, the Feynman rules for the vertices are still missing. In order to obtain them, we start from the CTP effective action

$$S[\phi_+,\phi_-] = \int d^4x[\mathcal{L}(\phi_+) - \mathcal{L}(\phi_-)]\,. \tag{12.17}$$

In the Keldysh basis, it reads

$$S[\phi_+,\phi_-] = \int d^4x\ \sqrt{-g}[\frac{1}{2}(\psi\hat{\mathcal{O}}\phi + \phi\hat{\mathcal{O}}\psi) - \frac{1}{2}\frac{\lambda}{3!}(\phi^3\psi + \phi\psi^3)]\,, \tag{12.18}$$

with the kinetic operator

$$\hat{\mathcal{O}} = \partial_t^2 + 3H\partial_t - \frac{\nabla^2}{a^2} + m^2. \tag{12.19}$$

The full set of Feynman rules for the Amphichronous QFT in Keldysh basis is presented in FIG 12.1. One can notice that in comparison with the stochastic approach, there is an additional type of vertices $\phi\psi^3$, which at least connects three retarded/advanced propagators. Since the causal propagators are not IR enhanced (*cf.* Eq. (12.14)), this type of vertices leads to a smaller degree of IR enhancement than the $\phi^3\psi$ vertex. Thus, diagrams with a $\phi\psi^3$ vertex can be neglected at the leading IR order.

12.2 IR correlation up to two-loop order

With the QFT Feynman rules, one can directly compute the diagram contributions to IR correlation up to second order of λ (at coincident point) for the case of a massive field with weak interaction where $\lambda \ll m^4/H^4$ which preserves the perturbative expansions.

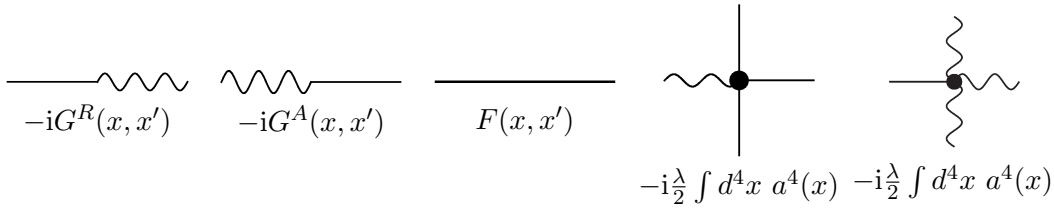

Figure 12.1: The elements of the QFT Feynman diagrams. The vertex factor is also chosen for which the assembled diagrams are divided by their symmetry factor. It is similar to Fig. 11.1 except the extra $\psi^3\phi$ vertex and the 4-dimensional vertex integral.

When ignoring diagrams with any $\phi\psi^3$ vertex, the QFT diagrams are identical to the stochastic diagrams. Therefore, FIG 11.2 also describes the QFT diagrams up to the second order. In the QFT method, each vertex integration is of the form as a typical convoluting integral in the past lightcone of the late time point. The calculation of seagull diagram is straightforward which has been shown in appendix B as an example. It is much more complicated for computing higher order diagrams contributions such as double seagull and sunset diagrams. When a vertex connects several other points (vertices), there are too many unknown parameters in the convoluting integral which make the spatial integration becomes practically impossible. However, this problem can be solved for two-loop diagrams by a Lorentzian transformation with respect to the de Sitter invariance. Note that there are only three different points (include vertices and coincident external points) in a two loop diagram. We denote them as x, x' and x_1. In the process of vertex integration on x_1, one can rotate the other two points x and x' to be coincided in space, *i.e.* $\mathbf{x} = \mathbf{x}'$, and perhaps be different in time. The non-local spatial integration therefore reduces to a local form as in the convolution integral of seagull diagram. Then, the diagram contributions to the leading IR correlation can be straightforwardly calculated in the late time limit up to two loops order, which give

$$\langle\phi^2\rangle_{\rm sg} = -\lambda\frac{9H^8}{64\pi^4m^6}\,, \tag{12.20a}$$

$$\langle\phi^2\rangle_{\rm ca} = \lambda^2\frac{27H^{12}}{1024\pi^6m^{10}}\,, \tag{12.20b}$$

$$\langle\phi^2\rangle_{\rm sgsg} = \lambda^2\frac{27H^{12}}{1024\pi^6m^{10}}\,, \tag{12.20c}$$

$$\langle\phi^2\rangle_{\rm ss} = \lambda^2\frac{9H^{12}}{512\pi^6m^{10}}\,. \tag{12.20d}$$

One would soon notice that the contribution from each diagram is identical to its counterpart from stochastic approach, except a factor of 2. To explain this problem, let us consider an arbitrary Feynman diagram with an integer number N of vertices. In this Feynman diagram, there are $2N+1$ internal and external propagator lines in total. Since every vertex comes with a retarded (or advance) propagator, the total number of statistical propagators is $N-1$. The $N+1$ statistical propagators will give a factor of 2^{N+1}

to the Feynman diagram. However, the N vertices give a factor of 2^{-N}. Thus, the field theoretical approach gives a factor of 2 enhancement for every diagram in the Keldysh basis. This enhancement comes from the scale choice in transformation (12.9). We will have more discussion on this scaling problem in the following chapter. Nonetheless, the agreement between stochastic and Amphichronous approaches at two-loop order strongly indicates that these two methods may be equivalent, at leading IR order.

Chapter 13

Equivalence between field theoretical and stochastic diagrams at leading IR order

13.1 Reduction of QFT Diagrams to the Stochastic Form

In order to find equivalence between stochastic and field theoretical approach to all loop orders, we look into the propagators (12.14) and (12.15) in the Keldysh basis of QFT. One would find that they have the same power term of de Sitter invariance length function which determines the spatial dependence of leading IR correlation. This power term can be rewritten as

$$|y|^{-\frac{m^2}{3H^2}} = \left|\frac{\eta\eta'}{(\eta-\eta')^2-(\mathbf{x}-\mathbf{x}')^2}\right|^{\frac{m^2}{3H^2}} = \left(\frac{\eta\eta'}{(\eta-\eta')^2}\right)^{\frac{m^2}{3H^2}}\left|\frac{1}{1-\delta^2}\right|^{\frac{m^2}{3H^2}}, \tag{13.1}$$

where $\delta^2 = \frac{(\mathbf{x}-\mathbf{x}')^2}{(\eta-\eta')^2}$. As we know from the convolution integral (see appendix B), integration for large time separation region (*i.e.* $|t-t'| \gg 1/H$) gives leading IR enhanced contributions of the order $\frac{H^2}{m^2}$, whereas for other regions are of the sub-leading order. Base on the approximation

$$\frac{\eta\eta'}{(\eta-\eta')^2} = \frac{\mathrm{e}^{-H|t-t'|}}{1+\mathrm{e}^{-2H|t-t'|}-2\mathrm{e}^{-H(t+t')}} \approx \mathrm{e}^{-H|t-t'|}, \tag{13.2}$$

the term in the parentheses of eq (13.1) can be written as $e^{-\frac{m^2}{3H}|t-t'|}$ in the large time separation region. since $m^2 \ll H^2$, one can expand

$$\left|\frac{1}{1-\delta^2}\right|^{\frac{m^2}{3H^2}} = 1+\mathcal{O}\left(\frac{m^2}{H^2}\right), \tag{13.3}$$

in the regimes

$$\delta^2 \ll 1-\exp(-\frac{3H^2}{m^2}) \quad \texttt{and} \quad 1+\exp(-\frac{3H^2}{m^2}) \ll \delta^2 \ll 1+\exp(\frac{3H^2}{m^2}). \tag{13.4}$$

In the region (13.4), the power term (13.1) can be approximately by

$$|y|^{-\frac{m^2}{3H^2}} = \mathrm{e}^{-\frac{m^2}{3H}|t-t'|} \times \left(1+\mathcal{O}\left(\frac{m^2}{H^2}\right)\right). \tag{13.5}$$

Thus, the field theoretical propagators (12.14) and (12.15) can be written as

$$F(x,x') = \frac{3H^4}{4\pi^2 m^2}\mathrm{e}^{-\frac{m^2}{3H}|t-t'|}, \tag{13.6}$$

and

$$G^R(x,x') = G^A(x',x) = \frac{H^2}{4\pi}\theta(t-t')\theta((\eta-\eta')^2-(\mathbf{x}-\mathbf{x}')^2)\mathrm{e}^{-\frac{m^2}{3H}(t-t')}. \quad (13.7)$$

We note that apart from a factor of 2, Eq. (13.6) is identical to the statistical propagator $F(t,t')$ in stochastic method (11.20), which is space independent. We also note that only one retarded/advanced propagator is involved in each vertex integral in the leading IR order calculation. Thus, the term $\frac{1}{4\pi}\theta((\eta-\eta')^2-(\mathbf{x}-\mathbf{x}'))$ can be absorbed into the vertex integral according to

$$-\mathrm{i}\frac{\lambda}{2}\int d^4x' a^4(x')\frac{1}{4\pi}\theta((\eta-\eta')^2-(\mathbf{x}-\mathbf{x}')) = -\mathrm{i}\frac{\lambda}{6}\int d\eta'\frac{(\eta-\eta')^3}{H^4\eta'^4} \approx -\mathrm{i}\frac{\lambda}{6H^3}\int dt'\,. \quad (13.8)$$

The latter approximation is valid since the large time separation region dominates the temporal integration, as we discussed above. Then, the retarded and advanced propagators can be effectively expressed as

$$G^R(x,x') = G^A(x',x) = \theta(t-t')H^2 e^{-\frac{m^2}{3H}(t-t')}, \quad (13.9)$$

whereas the effective vertex contribution is $-\mathrm{i}\frac{\lambda}{6H^3}\int dt'$. Now, the elements of diagrams from both methods are identical except a factor 2 in the statistical function and a factor 1/2 in the vertex coefficients. These discrepancies can be compensated by rescaling the QFT field in Keldysh basis $\phi \to \phi/\sqrt{2}$ and $\psi \to \sqrt{2}\psi$. Then, ignoring the $\psi^3\phi$ vertex, ϕ corresponds to the average field between the forward and backward time contours $\phi \to (\phi_+ + \phi_-)/2$, whereas ψ is equivalent to the auxiliary field in the stochastic approach. G^R and G^A are unaffected, whereas the statistical propagator F and the vertex $\psi\phi^3$ now coincide with the expressions from the Stochastic approach.

13.2 Contributions Close to the Light Cone and at Large Spatial Separations

We have shown that QFT Feynman diagrams are identical to the stochastic ones when the leading order approximation (13.3) is valid. However, this approximation is problematic for regions a) in the vicinity of the lightcone

$$1-\alpha\exp(-\frac{3H^2}{m^2}) < \delta^2 < 1+\alpha\exp(-\frac{3H^2}{m^2}), \quad (13.10)$$

and b) the large spacelike separation *i.e.* $\delta^2 \gg 1$,

$$\delta^2 > 1+\frac{1}{\alpha}\exp(\frac{3H^2}{m^2}), \quad (13.11)$$

where $1 \ll \alpha \ll \exp(\frac{3H^2}{m^2})$ is a constant. In order to justify the conclusion from the previous section, we have to estimate the error from these regions. For this purpose, we consider a general form of the integration of the vertex x',

$$\begin{aligned} I(\{x_i\}) &= -\mathrm{i}\frac{\lambda}{2}\int d^4x' a^4(x')\frac{H^2}{4\pi}\vartheta(\eta'-\eta_1)\vartheta((\eta'-\eta_1)^2-(\mathbf{x}'-\mathbf{x}_1)^2) \\ &\times \ |y(x',x_1)|^{-\frac{m^2}{3H^2}}|y(x',x_2)|^{-\frac{m^2}{3H^2}}|y(x',x_3)|^{-\frac{m^2}{3H^2}}|y(x',x_4)|^{-\frac{m^2}{3H^2}}\,. \quad (13.12) \end{aligned}$$

Here the vertex x' is connected with another vertex (or external point) x_1 by a causal propagator and is connected with other points by statistical propagators. The power terms can be written in the form of Eq. (13.1) with $\delta_i^2 = \frac{(\mathbf{x}_i-\mathbf{x}')^2}{(\eta_i-\eta')^2}$ where $i = 1, 2, 3, 4$. Thus the spatial integration in Eq. (13.12) take the form

$$\int d^3\mathbf{x}'\vartheta((\eta'-\eta_1)^2-(\mathbf{x}'-\mathbf{x}_1)^2)\prod_{i=1}^{4}\left|\frac{1}{\tilde{\delta}_i^2}\right|^{\epsilon} = 4\pi(\eta_1-\eta')^3\int_0^1 d|\tilde{\delta}_1|\delta_1^2\prod_{i=1}^{4}\left|\frac{1}{\tilde{\delta}_i^2}\right|^{\epsilon}, \quad (13.13)$$

where $\tilde{\delta}_i^2 = 1-\delta_i^2$ and $\epsilon = \frac{m^2}{3H^2}$. If all separations $x'-x_i$ satisfy the condition (13.4), we approximately take $\left|\frac{1}{\tilde{\delta}_i^2}\right|^{\epsilon} \approx 1$, and only the term $\frac{4\pi}{3}(\eta_1-\eta')^3$ in eq (13.13) can be passed to the temporal integration.

Now, let we consider the case where some δ^2s lies in the vicinity of lightcone (13.10). In this case, the near lightlike δ^2s can be treated as equal and denoted as δ_j^2, since the regime is extremely narrow. We use $d|\tilde{\delta}_j|$ as a variable of integration. Then, the integration in Eq. (13.13) can be written as

$$2\int_0^{\frac{1}{2}\alpha e^{-1/\epsilon}} d|\tilde{\delta}_j|\delta_j^2\left|\frac{1}{\tilde{\delta}_j}\right|^{2n\epsilon} = \left.\frac{2\tilde{\delta}_j^{3-2n\epsilon}}{3-2n\epsilon}\right|_0^{\frac{1}{2}\alpha e^{-1/\epsilon}}, \quad (13.14)$$

where $n = 1, 2, 3, 4$ is the number of nearly light-like separations. Therefore, compared to the leading IR correlation, contributions from the vicinity of lightcone are exponentially suppressed by a factor $\alpha e^{-\frac{3H^2}{m^2}}$. This suppression arises from the spatial integration due to the narrow width of the integration region.

In addition, we turn to cases of large separations that is defined by relation (13.11). First of all, we have to specify the up-limit of δ^2. Note that due to the causality, all vertices in Feynman diagrams must locate in the past-lightcone of the late time limit point x. If we set the spatial vector of x to be $\vec{x} = \vec{0}$ and the comoving time as η_0, then for any vertex x_1, the norm of its spatial vector $|\mathbf{x}_1|$ cannot be large than its comoving time $\eta_1-\eta_0$. Hence, the spatial separation between two points x_1 and x_2 must be less than or equal the sum of their comoving time, *i.e.* $(\mathbf{x}_1-\mathbf{x}_2)^2 \leq (\eta_1+\eta_2-2\eta_0)^2$ (as illustrated in FIG 13.1). Thus,the upper-bound of δ^2 is given by

$$\delta^2(x', x_i) = \frac{(\mathbf{x}'-\mathbf{x}_i)^2}{(\eta'-\eta_i)^2} \leq 1 + \frac{4\eta'\eta_i + 4\eta_o^2 - 4\eta_o(\eta'+\eta_i)}{(\eta'-\eta_i)^2}, \quad (13.15)$$

whereas the lower bound is from relation (13.11) in the form $\exp(1/\epsilon)/\alpha \leq \delta^2$. Solving this inequality, one find that η' has to be in the range (thin strip)

$$\eta_i - 2\sqrt{\alpha}\mathrm{e}^{-\frac{1}{2\epsilon}}(\eta_o-\eta_i) \leq \eta' \leq \eta_i + 2\sqrt{\alpha}\mathrm{e}^{-\frac{1}{2\epsilon}}(\eta_o-\eta_i), \quad (13.16)$$

in which the separation satisfies relation (13.11) and maintains the causality. Moreover, from inequality (13.11), the upper-bound for the power term (13.1) can be also obtained

$$|y(x,x')|^{-\epsilon} \leq \alpha^{\epsilon}e^{-1}\left(\frac{(\eta^2-\eta'^2)}{\eta\eta'}\right)^{-\epsilon}. \quad (13.17)$$

Then, the upper-bound of the convolution integral (13.12) can be estimated by replacing the power terms for large δ^2 separation with its maximal value in Eq. (13.17) and taking

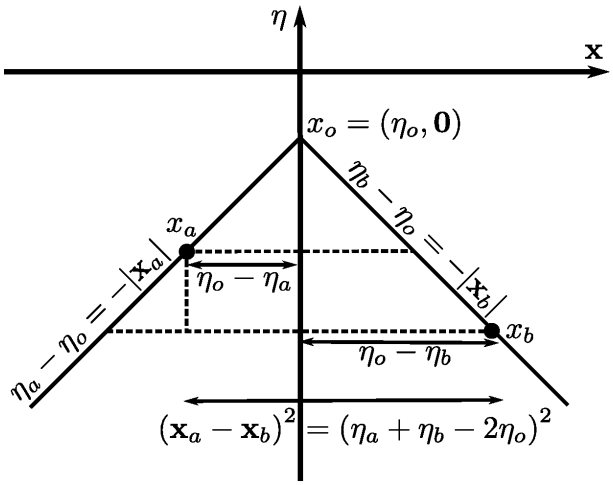

Figure 13.1: Two-dimensional sketch of the maximal spatial distance between two vertices in the late time limit leading IR correlation.

approximation (13.5) for others. Then, the integrand becomes spatially independent, and the domain of temporal integration is given by inequality (13.16) which is extremely narrow. After doing the vertex integration, the final result is proportional to $\alpha^{1+\epsilon} e^{-1-\frac{1}{\epsilon}}$, which is exponentially suppressed. Detailed calculations of this case are shown in the appendix C. In this case, the exponential suppression behavior is due to the narrow width of the domain of temporal integration.

Until now, one may worry about the mixing case where some separations lie in the vicinity of lightcone and some separations with a large value of δ^2 at the same time. However, it is not a matter. Because vertex integrals for near lightcone regions are exponential suppressed by the domain of spatial integration, whereas the integrals for large δ^2 separations are exponentially suppressed by the domain of temporal integration, the mixing of them should still exhibit an exponential suppression. Therefore, we conclude that the approximation (13.5) is applicable for leading IR calculations in the late time limit. Hence, the field theoretical approach is fully equivalent to the stochastic one at the leading IR order.

Chapter 14

Resumming the QFT in the late time limit

As we mentioned before, perturbation expansion breaks down in the small mass limit $m^2 \to 0$. In this case, a resummation on the contributions from all loop order diagrams is needed. However, this task is very challenging for the field theoretical approach, because vertex integrals in higher loop diagrams can be extremely complicated. For example, if there is a vertex connected with four other different vertices, then the corresponding spatial integration cannot be calculated out analytically. Fortunately, we know that the QFT Feynman diagrams are identical to the stochastic ones at the leading IR order. Therefore, one can find out the result of field theoretical approach by resumming the contributions from stochastic diagrams, which is much easier to do.

In order to do the resummation, we start from the functional partition function in Eq. (11.16). One can easily integrate over the auxiliary field ψ, which gives

$$\mathcal{Z} = \int D[\phi]\, \mathrm{e}^{-\frac{2\pi^2}{H^3}\int_0^T \mathrm{d}u \left(\dot{\phi}+\frac{\partial_\phi V}{3H}\right)^2} = \int D[\phi]\, \mathrm{e}^{-\frac{2\pi^2}{H^3}\int_0^T \mathrm{d}t \left(\dot{\phi}^2+2\dot{\phi}\frac{\partial_\phi V}{3H}+\left(\frac{\partial_\phi V}{3H}\right)^2\right)}, \tag{14.1}$$

where the boundaries of the integral is specified in the exponential term. Then, it can be written as

$$\mathcal{Z} = \int_{-\infty}^{+\infty} \mathrm{d}\phi_T\ \mathrm{e}^{-\frac{4\pi^2}{3H^4}V(\phi_T)} \int D[\phi_{t<T}] \mathrm{e}^{-\frac{2\pi^2}{H^3}\mathcal{S}[\phi]} \tag{14.2}$$

with

$$\mathcal{S}[\phi] = \int_0^T \mathrm{d}t \left[\dot{\phi}^2 + \left(\frac{\partial_\phi V}{3H}\right)^2\right], \tag{14.3}$$

where $\phi_T \equiv \phi(T)$ and the initial condition $\phi(0) = 0$, $V[0] = 0$ is assumed. Besides, we have split the path integral in terms of an integral over the evolving ϕ from time $0 \to T$ and a further integration over the final field at the time T. Since we are interested in the late time limit, where the field is in a static equilibrium, we can make use of the steepest descent method. At late-time, the integral dominated by the path $\phi_0(t)$ extremising the pseudo-action $\mathcal{S}$, *i.e.* $\frac{\delta\mathcal{S}}{\delta\phi}\Big|_{\phi=\phi_0}$. The latter condition is equivalent to

$$\ddot{\phi_0} - \frac{1}{9H^2}\partial_\phi V \partial_\phi^2 V\Big|_{\phi=\phi_0} = 0. \tag{14.4}$$

Moreover, since we integrate over physical configuration, the solution has to satisfy the following conditions $\phi_0(0) = 0$ and $\phi_0(T) = \phi_T$. Integrating the above equation yields

$$\dot{\phi_0}^2 - \frac{1}{9H^2}\left(\partial_\phi V|_{\phi=\phi_0}\right)^2 = E, \tag{14.5}$$

where E is an integration constant which is constrained by the boundary boundary condition $\phi_0(T) = \phi_T$. For the potential (10.15), we have $\partial_\phi V(\phi)|_{\phi=\phi_0(0)=0} = 0$. Therefore, the value of E tend to zero as $T \to \infty$. More precisely, from the boundary conditions $\phi(0) = 0$ and $\phi(T) = \phi_T$, it is easily to obtain the relation $ET \leq \phi_T/T$. Thus one finds that $ET \to 0$ at the late time $T \to \infty$. Therefore, in the late time limit, the pseudo action (14.3) can be expressed as

$$\mathcal{S}[\phi_0] = 2\int_0^T \mathrm{d}t\, \dot{\phi_0}^2 = \frac{2}{3H}\int_0^T \mathrm{d}t\, \dot{\phi_0}\, \partial_\phi V|_{\phi=\phi_0} = \frac{2}{3H} V(\phi_T)\,, \tag{14.6}$$

Here, the boundary conditions $\phi_0(0) = 0$ and $\phi_0(T) = \phi_T$ are used. Substituting Eq. (14.6) into Eq. (14.3) and relabeling $\phi_T = \varphi$, we obtain the late time partition function

$$\mathcal{Z} = \int_{-\infty}^{+\infty} \mathrm{d}\varphi\ \mathrm{e}^{-\frac{8\pi^2}{3H^4}V(\varphi)}\,, \tag{14.7}$$

which is the same to the one-point distribution function in Ref. [124]. It means that our result is in agreement with the result from the Fokker-Planck method. Note that the choice of initial conditions corresponds to the initial of the inflation at the time $t = 0$, where is no significant fluctuations. Note also that in fact, we are working on the resummation of the stochastic diagrams. Therefore, it convinces us that the diagrammatic expansion of the stochastic method is valid for all loop orders.

Conclusion

In this part, we have computed the leading IR correlation $\langle\phi(x)\phi(x)\rangle$ at coincide point both perturbatively to second order in coupling and with a non-perturbative resummation using field theoretical and stochastic approaches. As for the stochastic approach, we had a brief introduction to the Fokker-Planck equation method by Starobinsky and Yokoyama. Then, a diagrammatic expansion for the stochastic has been developed and found agreement with both Fokker-Planck equation method and the field theoretical approach. In addition, by extracting the leading IR contributions from free QFT propagators in Keldysh basis, the QFT Feynman diagrams have been proved to be identical to stochastic diagrams. Finally, we resummed the diagram contributions on the IR correlation up to all loop orders. This indicates the agreement between stochastic and field theoretical approach is generally valid. Moreover, this agreement should also be applicable to a $O(N)$ scalar field theory, where the perturbative expansion does not necessary need to be truncated. The equivalence of both methods indicates that one can calculate the leading fluctuations by stochastic method to avoid more complicated convolution integrals in the framework of QFT. However, one should note that the stochastic approach can give only the leading order IR correlation whereas the field theoretical in principle can obtain the correlation functions at every order of m^2/H^2. Therefore, the field theoretical approach provides insights into the dynamical behaviour of the scalar field on the de Sitter background. Moreover, since the field theoretical approach is based on the first principle of QFT, it also provide more understanding for the approximations in the stochastic approach. Since the scalar model can serve as a toy model for the gravitation [120], this work might be helpful to build a quantum gravity with general invariant gauge in de Sitter space.

General conclusion and perspectives

In this manuscript, we have demonstrated many aspects of primordial scalar fluctuations during inflation.

In the first part, we have investigated the level of non-Gaussianity and power spectrum of curvature perturbations for the original and supersymmetric F-term and D-term hybrid inflation models with a mild waterfall phase. We find that due to the significant contribution of entropy modes, these models cannot satisfy the CMB angular constraints on the level of non-Gaussianity and power spectrum of curvature perturbations simultaneously, in the cases where the waterfall last $N \gtrsim 60$. Here, we note that the enhancement in the level of non-Gaussianity during the epoch of reheating [172] is not taken into account. In fact, it is very challenging to apply the δN formalism on a tachyonic preheating phase. Moreover, in the case where the duration of waterfall is $1 < N \lesssim 60$, it gives a modification on the slow-roll prediction of inflation along the valley. We leave this case for future work. Finally, we remark that the observable predictions for the quantum diffusion regime [159] which is near the critical instability point have not been derived. In this regime, quantum fluctuations of both inflaton and waterfall fields dominate over the classic motions. It requires a new method (stochastic or QFT method from part III) to give the observable predictions.

In the second part, we have examined inflation models and curvaton scenarios with CMB spectral distortions. We find that only one single-field model (hybrid inflation in the valley) can give rise to an observable level of CMB distortion for the PIXIE experiment. In addition, the PIXIE experiment can detect the signal of distortions generated by multi-field inflation models with sudden turning trajectories or with mild waterfall ($20 \lesssim N \lesssim 60$) trajectories as well. For the next to next generation (PRISM-class) experiment, which is about ten times sensitive to PIXIE, the situation is improved. In principle, all models with a large value of running of spectral index can induce detectable CMB distortions to the PRISM-class experiment. One should notice that our discussion focus on the CMB distortions sourced by the dispersion of acoustic wave in the primeval plasma. There are still other sources of energy injection to the CMB photons in the epoch before prior to the recombination, such as decay/annihilation of relic particles and evaporation of primordial black holes. Therefore, even if the μ-type and intermediate i-type distortions are detected in the future, one will not be able to relate them directly to the primordial fluctuations during inflation. Moreover, in the process of our calculation, we choose some representative parameter sets in the allowed region of parameter space for every model. However, it still possible that some particular points (or fine-tuned region) in the parameter space are

not missed. A full MCMC analysis is therefore expected. Nevertheless, some additional constraints for some models are not considered, such as UCMH and PBH constraints for the hybrid inflation with a mild waterfall phase.

In the third part, we have computed quantum fluctuations of a light scalar field ($m^2 \ll H^2$) in the late time limit by stochastic and field theoretic approaches respectively. We find agreement between both approaches at the leading IR order of m^2/H^2. Note that both stochastic and field theoretic approaches are time dependent that can be used to study the time-evolution of scalar fluctuations. However, in principle, the field theoretical approaches can evaluate the fluctuation up to all orders, whereas the stochastic approach is only available for the leading IR order. The sub-leading IR order would be interesting, since it may reveal the behaviour of dispersion of fluctuations and the classic to quantum transition. Moreover, the field theoretic method can also be applied to study the interplay between UV and IR effects which may settle the controversy over adiabatic subtraction [173, 174, 175, 176]. As stated in Ref. [120], the gravity field on de Sitter background exhibits a similar IR divergence as the scalar field. Therefore, the field theoretic approach is potentially used to investigate quantum fluctuations of gravitons in a general de Sitter invariant gauge as well.

Appendix

Appendix A

Long-distance behaviour of the propagator

The well-known solution to Eq. (12.3) reads

$$\mathrm{i}\Delta^{(0)}(y) = \frac{\Gamma\left(\frac{D-1}{2}+\nu\right)\Gamma\left(\frac{D-1}{2}-\nu\right)}{(4\pi)^{\frac{D}{2}}\Gamma\left(\frac{D}{2}\right)} H^{D-2}\,{}_2F_1\left(\frac{3}{2}+\nu,\frac{3}{2}-\nu;2;1+\frac{y}{4}\right), \tag{A.1}$$

where

$$\nu = \sqrt{\left(\frac{D-1}{2}\right)^2 - \frac{m^2}{H^2}}, \tag{A.2}$$

and D is the dimension of spacetime. In this manuscript, we work in a four-dimension spacetime. However, for a generic discussion, we leave D as a parameter. In order to extract the leading behaviour for large y, we employ the transformation formula

$$\begin{aligned} &{}_2F_1\left(\frac{D-1}{2}+\nu,\frac{D-1}{2}-\nu;\frac{D}{2};1+\frac{y}{4}\right) \\ =&\frac{\left(-\frac{y}{4}\right)^{-\frac{D-1}{2}-\nu}\Gamma\left(\frac{D}{2}\right)\Gamma(-2\nu)}{\Gamma\left(\frac{D-1}{2}-\nu\right)\Gamma\left(\frac{1}{2}-\nu\right)}{}_2F_1\left(\frac{D-1}{2}+\nu,\frac{1}{2}+\nu;1+2\nu;-\frac{4}{y}\right) \\ +&\frac{\left(-\frac{y}{4}\right)^{-\frac{D-1}{2}+\nu}\Gamma\left(\frac{D}{2}\right)\Gamma(2\nu)}{\Gamma\left(\frac{D-1}{2}+\nu\right)\Gamma\left(\frac{1}{2}+\nu\right)}{}_2F_1\left(\frac{D-1}{2}-\nu,\frac{1}{2}-\nu;1-2\nu;-\frac{4}{y}\right). \end{aligned} \tag{A.3}$$

For the hypergeometric functions, we apply the series expansion

$${}_2F_1(\alpha,\beta;\gamma;z) = \frac{\Gamma(\gamma)}{\Gamma(\alpha)\Gamma(\beta)}\sum_{n=0}^{\infty}\frac{\Gamma(\alpha+n)\Gamma(\beta+n)}{\Gamma(\gamma+n)}\frac{z^n}{n!}, \tag{A.4}$$

according to their definition. For $D=4$, one obtains

$$\begin{aligned} \mathrm{i}\Delta^{(0)}(y) =& H^2\left(\frac{1}{16\pi^2}-\frac{1}{24\pi^2}\frac{m^2}{H^2}+\mathcal{O}\left(\frac{m^4}{H^2}\right)\right)\left(-\frac{y}{4}\right)^{-\frac{5}{2}+\nu} \\ &+H^2\left(\frac{3H^2}{8\pi^2m^2}-\frac{7}{24\pi^2}+\mathcal{O}\left(\frac{m^2}{H^2}\right)\right)\left(-\frac{y}{4}\right)^{-\frac{3}{2}+\nu} \\ &+H^2\mathcal{O}\left(\frac{m^2}{H^2}\right)\left(-\frac{y}{4}\right)^{-\frac{7}{2}+\nu}+\cdots. \end{aligned} \tag{A.5}$$

For arbitrary D, the higher order terms are suppressed due to a large value of y. Therefore, the leading behavior is given by

$$\mathrm{i}\Delta^{(0)}(y) = \frac{1}{2(D-1)KH^2}\left(-\frac{y}{4}\right)^{-1-\frac{m^2}{(D-1)H^2}} + \frac{1}{m^2K}\left(-\frac{y}{4}\right)^{-\frac{m^2}{(D-1)H^2}}+\cdots, \tag{A.6}$$

where

$$K = \frac{2\pi^{\frac{D+1}{2}}}{\Gamma\left(\frac{D+1}{2}\right) H^D} \,. \tag{A.7}$$

Appendix B

Seagull diagram contribution to leading IR correlation

The seagull diagram (presented in FIG 11.2) consist of one vertex and two external points. As we are interested in the IR correlation for coincide points in the late time limit. The contribution from seagull diagram can be directly given by a convolution integral, which reads

$$\langle\phi^2\rangle_{sg} = -\,\mathrm{i}\frac{\lambda}{2}\int d^4x' a^4(x')(-\mathrm{i}G^R(x,x'))(F(x,x')F(x',x')) \tag{B.1}$$

$$= -\,\frac{\lambda}{4}\left(\frac{3H^4}{4\pi^2m^2}\right)^2\left(\frac{H^2}{4\pi^2}\right)\int d^4x' a^4(x')\left|y(x;x')\right|^{-\frac{2}{3}\frac{m^2}{H^2}}\vartheta((\eta-\eta')^2-(\mathbf{x}-\mathbf{x}')^2)\vartheta(\eta'-\eta) \tag{B.2}$$

$$= -\,\frac{\lambda}{4}\left(\frac{3H^4}{4\pi^2m^2}\right)^2\left(\frac{H^2}{2\pi}\right)\int_{-\infty}^{\eta} d\eta'\frac{1}{H^4\eta'^4}\int d^3\mathbf{x}'\vartheta((\eta-\eta')^2-(\mathbf{x}-\mathbf{x}')^2) \times\left(\frac{\eta\eta'}{[(\eta-\eta')^2-(\mathbf{x}-\mathbf{x}')^2]}\right)^{\frac{2}{3}\frac{m^2}{H^2}}$$

$$= -\,\frac{\lambda}{8}\left(\frac{3H^4}{4\pi^2m^2}\right)^2\left(\frac{H^2}{2\pi}\right)\frac{4\pi}{3}\int_{-\infty}^{\eta} d\eta'\frac{(\eta\eta')^{\frac{2}{3}\frac{m^2}{H^2}}}{H^4\eta'^4}(\eta-\eta')^{3-\frac{4}{3}\frac{m^2}{H^2}}$$

$$\approx\frac{\lambda}{8}\left(\frac{3H^4}{4\pi^2m^2}\right)^2\left(\frac{2}{3H^2}\right)\int_{-\infty}^{\eta} d\eta'(-\eta')^{-1-\frac{2}{3}\frac{m^2}{H^2}}$$

$$=\frac{\lambda}{8}\left(\frac{3H^4}{4\pi^2m^2}\right)^2\left(\frac{2}{3H^2}\right)\left[\frac{(-\eta')^{-\frac{2}{3}\frac{m^2}{H^2}}}{\frac{2}{3}\frac{m^2}{H^2}}\right]_{\eta'\to-\infty}^{\eta'=\eta}$$

$$\approx -\,\lambda\frac{9H^8}{64\pi^4m^6}\,.$$

In the process of calculation, we notice that the temporal integral in the region $\eta'\sim\eta$ contributes in the sub-leading order.

Appendix C

Vertex integral for large spacelike separations

In the convoluting integration (13.12), point x' is running over the past lightcone of x_1 due to the θ functions. Let us now consider one of the other points, say x_2. According to the inequality (13.16), a large δ_2^2 corresponds to the region between the two red dashed lines in Figure C.1. In this region, the power term $y(x', x_2)^{-\epsilon}$ is bounded by (13.17), where $\epsilon = \frac{m^2}{3H^2}$. Assuming that x_3 and x_4 are out of the strip between the dashed lines, we can obtain an upper bound to the integral by replacing all the power terms with the r.h.s. of (13.17). Thus, the upper limit of the vertex integration in this strip is given by

$$
\begin{aligned}
I &\leq -\mathrm{i}\frac{\lambda}{2}\int_{\eta_2-2\eta_2\sqrt{\alpha}e^{-\frac{1}{2\epsilon}}}^{\eta_2+2\eta_2\sqrt{\alpha}e^{-\frac{1}{2\epsilon}}} d\eta' \frac{1}{\eta'^4}\int_0^{\eta_1-\eta'} dr 4\pi r^2 \alpha^\epsilon e^{-1} \\
&\quad \left(\frac{(\eta_1-\eta')^2}{\eta_1\eta'}\right)^{-\epsilon}\left(\frac{(\eta_2-\eta')^2}{\eta_2\eta'}\right)^{-\epsilon}\left(\frac{(\eta_3-\eta')^2}{\eta_3\eta'}\right)^{-\epsilon}\left(\frac{(\eta_4-\eta')^2}{\eta_4\eta'}\right)^{-\epsilon} \\
&= -\mathrm{i}\frac{\lambda}{2}\int_{\eta_2-2\eta_2\sqrt{\alpha}e^{-\frac{1}{2\epsilon}}}^{\eta_2+2\eta_2\sqrt{\alpha}e^{-\frac{1}{2\epsilon}}} d\eta' \frac{1}{\eta'^4}\frac{4\pi}{3}(\eta_1-\eta')^3 \alpha^\epsilon e^{-1} \\
&\quad \left(\frac{(\eta_1-\eta')^2}{\eta_1\eta'}\right)^{-\epsilon}\left(\frac{(\eta_2-\eta')^2}{\eta_2\eta'}\right)^{-\epsilon}\left(\frac{(\eta_3-\eta')^2}{\eta_3\eta'}\right)^{-\epsilon}\left(\frac{(\eta_4-\eta')^2}{\eta_4\eta'}\right)^{-\epsilon} \\
&\approx -\mathrm{i}\frac{\lambda}{2}\frac{4\pi}{3}\alpha^\epsilon e^{-1}\left(-\frac{3H^2}{2m^2}\right)\left(\prod_{i=1}^4\eta_i\right)^\epsilon \eta^{-4\epsilon}\Bigg|_{\eta_2-2\eta_2\sqrt{\alpha}e^{-\frac{1}{2\epsilon}}}^{\eta_2+2\eta_2\sqrt{\alpha}e^{-\frac{1}{2\epsilon}}} \\
&\propto \alpha^{1+\epsilon}e^{-1-\frac{1}{\epsilon}}. \qquad \text{(C.1)}
\end{aligned}
$$

In the temporal integration, we have used the large time separation assumption for the power terms except $(\eta_2 - \eta')$. For calculating the leading IR fluctuation in the late time limit, this assumption is valid because the invalid regions give only sub-leading contributions. Moreover, one can do similar integrations for the strip of large δ^2 around points x_3 and x_4 respectively. Even if strips for points overlap, one can still replace the power terms by their upper limit, and the exponentially suppressed behaviour will not be changed in the temporal integration. Therefore, we can conclude that the vertex integration for large δ regime is exponentially suppressed and can be safely ignored.

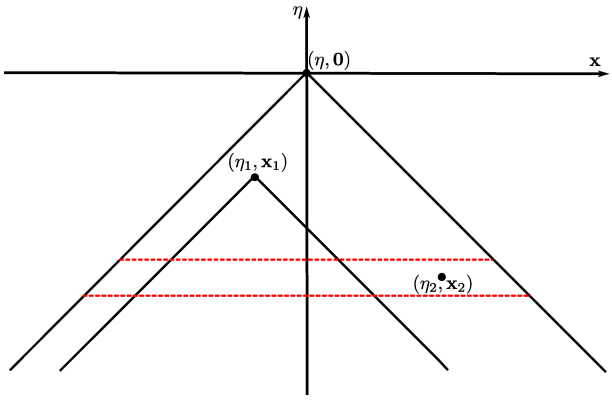

Figure C.1: Sketch for large δ^2 regime. The domain of vertex integration is the past lightcone of x_1. The large δ^2 region for $y(x', x_2)$ is the narrow stripe inside the red dashed lines.

Appendix D

Notations and conventions

Here, we briefly list the general notations and conventions used in this manuscript

$a(t)$ or $a(\eta)$	Scale factor in Robertson-Walker metric, which indicates the size of the universe.
K	A constant represented the spatial curvature. In common, we take $K = 0$.
overdot $\cdot$	Derivative with respect to the coordinate time t.
$'$	Derivative with respect to the conformal time η.
$H \equiv \dot{a}/a$	Hubble parameter.
$\mathcal{H} \equiv a'/a$	Conformal Hubble parameter.
N	Number of e-folds, also used as the e-fold time.
$d_h \approx H^{-1}$	Radius of the particle horizon, also called Hubble radius.
ϵ_n, $n = 1, 2, \cdots$	Slow roll parameters.
Ψ and Φ	Bardeen potentials (gravitational potentials).
ζ	Curvature perturbation.
$\mathcal{P}_\zeta$	Power spectrum of curvature perturbations.
n_s	Spectral index.
B_ζ	Bispectrum of curvature perturbations.
f_{NL}	Non-Gaussianity parameter.

$k_p \equiv 0.05 Mpc^{-1}$	Pivot scale for CMB angular observations.
$k_d \equiv 42 Mpc^{-1}$	Pivot scale for CMB distortion observations.
ΔI	Change in the intensity caused by CMB distortions.
$\gamma_E = 0.5772$	Euler-Mascheroni constant.
$y(x, x')$	De Sitter invariant length function.
$\langle \phi^2 \rangle$	Correlation function of coincident points.

Bibliography

[1] R. Alpher, H. Bethe, and G. Gamow, "The origin of chemical elements", Phys.Rev. **73** (1948) 803.

[2] R. A. Alpher and R. Herman, "Evolution of the Universe", Nature **162** (1948) 774.

[3] A. A. Penzias and R. W. Wilson, "A Measurement of excess antenna temperature at 4080-Mc/s", Astrophys.J. **142** (1965) 419.

[4] A. H. Guth, "The Inflationary Universe: A Possible Solution to the Horizon and Flatness Problems", Phys.Rev. **D23** (1981) 347.

[5] A. A. Starobinsky, "Spectrum of relict gravitational radiation and the early state of the universe", JETP Lett. **30** (1979) 682.

[6] A. A. Starobinsky, "A New Type of Isotropic Cosmological Models Without Singularity", Phys.Lett. **B91** (1980) 99.

[7] D. Kazanas, "Dynamics of the Universe and Spontaneous Symmetry Breaking", Astrophys.J. **241** (1980) L59.

[8] K. Sato, "First Order Phase Transition of a Vacuum and Expansion of the Universe", Mon.Not.Roy.Astron.Soc. **195** (1981) 467.

[9] S. Hawking, I. Moss, and J. Stewart, "Bubble Collisions in the Very Early Universe", Phys.Rev. **D26** (1982) 2681.

[10] A. H. Guth and E. J. Weinberg, "Could the Universe Have Recovered from a Slow First Order Phase Transition?", Nucl.Phys. **B212** (1983) 321.

[11] A. D. Linde, "A New Inflationary Universe Scenario: A Possible Solution of the Horizon, Flatness, Homogeneity, Isotropy and Primordial Monopole Problems", Phys.Lett. **B108** (1982) 389.

[12] A. Albrecht and P. J. Steinhardt, "Cosmology for Grand Unified Theories with Radiatively Induced Symmetry Breaking", Phys.Rev.Lett. **48** (1982) 1220.

[13] A. A. Starobinsky, "Dynamics of Phase Transition in the New Inflationary Universe Scenario and Generation of Perturbations", Phys.Lett. **B117** (1982) 175.

[14] A. H. Guth and S. Pi, "Fluctuations in the New Inflationary Universe", Phys.Rev.Lett. **49** (1982) 1110.

[15] S. Hawking, "The Development of Irregularities in a Single Bubble Inflationary Universe", Phys.Lett. **B115** (1982) 295.

[16] J. M. Bardeen, P. J. Steinhardt, and M. S. Turner, "Spontaneous Creation of Almost Scale - Free Density Perturbations in an Inflationary Universe", Phys.Rev. **D28** (1983) 679.

[17] R. H. Brandenberger, R. Kahn, and W. H. Press, "Cosmological Perturbations in the Early Universe", Phys.Rev. **D28** (1983) 1809.

[18] A. H. Guth and S.-Y. Pi, "The Quantum Mechanics of the Scalar Field in the New Inflationary Universe", Phys.Rev. **D32** (1985) 1899.

[19] G. Hinshaw *et al.*, "Nine-Year Wilkinson Microwave Anisotropy Probe (WMAP) Observations: Cosmological Parameter Results", Astrophys.J.Suppl. **208** (2013) 19, arXiv:1212.5226.

[20] P. Ade *et al.*, "Planck 2013 results. XXII. Constraints on inflation", arXiv:1303.5082.

[21] P. Ade *et al.*, "Detection of B-Mode Polarization at Degree Angular Scales by BICEP2", Phys.Rev.Lett. **112** (2014) 241101, arXiv:1403.3985.

[22] E. Kolb and M. Turner, *The Early Universe*, Frontiers in physics, Westview Press1994.

[23] S. Dodelson, *Modern Cosmology*, Academic Press, Academic Press2003.

[24] V. Mukhanov, *Physical foundations of cosmology*, Cambridge University Press2005.

[25] S. Weinberg, *Cosmology*, OUP Oxford2008.

[26] D. H. Lyth and A. R. Liddle, *The primordial density perturbation: Cosmology, inflation and the origin of structure*, Cambridge University Press2009.

[27] J. Martin, C. Ringeval, and V. Vennin, "Encyclopaedia Inflationaris", Phys.Dark Univ. arXiv:1303.3787.

[28] A. Riotto, "Inflation and the theory of cosmological perturbations", (2002) 317arXiv:hep-ph/0210162.

[29] P. Ade *et al.*, "Planck 2013 results. XVI. Cosmological parameters", Astron.Astrophys. arXiv:1303.5076.

[30] A. Conley *et al.*, "Supernova Constraints and Systematic Uncertainties from the First 3 Years of the Supernova Legacy Survey", Astrophys.J.Suppl. **192** (2011) 1, arXiv:1104.1443.

[31] A. G. Riess, *et al.*, "A 3Hubble Constant with the Hubble Space Telescope and Wide Field Camera 3", Astrophys.J. **730** (2011) 119, arXiv:1103.2976.

[32] N. Suzuki, *et al.*, "The Hubble Space Telescope Cluster Supernova Survey: V. Improving the Dark Energy Constraints Above z>1 and Building an Early-Type-Hosted Supernova Sample", Astrophys.J. **746** (2012) 85, arXiv:1105.3470.

[33] W. Rindler, "Visual horizons in world-models", Gen.Rel.Grav. **34** (2002) 133.

[34] J. Beringer *et al.*, "Review of Particle Physics (RPP)", Phys.Rev. **D86** (2012) 010001.

[35] I. De Mitri, "Search for GUT monopoles and massive exotic particles with MACRO", Nucl.Phys.Proc.Suppl. **95** (2001) 82.

[36] P. J. Steinhardt and N. Turok, "The Cyclic model simplified", New Astron.Rev. **49** (2005) 43, arXiv:astro-ph/0404480.

[37] A. R. Liddle, P. Parsons, and J. D. Barrow, "Formalizing the slow roll approximation in inflation", Phys.Rev. **D50** (1994) 7222, arXiv:astro-ph/9408015.

[38] R. Adam *et al.*, "Planck intermediate results. XXX. The angular power spectrum of polarized dust emission at intermediate and high Galactic latitudes", arXiv:1409.5738.

[39] T. Bunch and P. Davies, "Quantum Field Theory in de Sitter Space: Renormalization by Point Splitting", Proc.Roy.Soc.Lond. **A360** (1978) 117.

[40] D. Wands, K. A. Malik, D. H. Lyth, and A. R. Liddle, "A New approach to the evolution of cosmological perturbations on large scales", Phys.Rev. **D62** (2000) 043527, arXiv:astro-ph/0003278.

[41] A. A. Starobinsky, "Multicomponent de Sitter (Inflationary) Stages and the Generation of Perturbations", JETP Lett. **42** (1985) 152.

[42] M. Sasaki and E. D. Stewart, "A General analytic formula for the spectral index of the density perturbations produced during inflation", Prog.Theor.Phys. **95** (1996) 71, arXiv:astro-ph/9507001.

[43] D. H. Lyth, K. A. Malik, and M. Sasaki, "A General proof of the conservation of the curvature perturbation", JCAP **0505** (2005) 004, arXiv:astro-ph/0411220.

[44] N. S. Sugiyama, E. Komatsu, and T. Futamase, "The δN Formalism", Phys. Rev. **D87** (2013) 023530, arXiv:1208.1073.

[45] A. D. Linde, "Hybrid inflation", Phys.Rev. **D49** (1994) 748, arXiv:astro-ph/9307002.

[46] G. Dvali, Q. Shafi, and R. K. Schaefer, "Large scale structure and supersymmetric inflation without fine tuning", Phys.Rev.Lett. **73** (1994) 1886, arXiv:hep-ph/9406319.

[47] E. J. Copeland, *et al.*, "False vacuum inflation with Einstein gravity", Phys.Rev. **D49** (1994) 6410, arXiv:astro-ph/9401011.

[48] E. Halyo, "Hybrid inflation from supergravity D terms", Phys.Lett. **B387** (1996) 43, arXiv:hep-ph/9606423.

[49] P. Binetruy and G. Dvali, "D term inflation", Phys.Lett. **B388** (1996) 241, arXiv:hep-ph/9606342.

[50] S. Clesse, "Hybrid inflation along waterfall trajectories", Phys.Rev. **D83** (2011) 063518, arXiv:1006.4522.

[51] H. Kodama, K. Kohri, and K. Nakayama, "On the waterfall behavior in hybrid inflation", Prog.Theor.Phys. **126** (2011) 331, arXiv:1102.5612.

[52] S. Clesse and B. Garbrecht, "Slow Roll during the Waterfall Regime: The Small Coupling Window for SUSY Hybrid Inflation", Phys.Rev. **D86** (2012) 023525, arXiv:1204.3540.

[53] A. Kogut, *et al.*, "The Primordial Inflation Explorer (PIXIE): A Nulling Polarimeter for Cosmic Microwave Background Observations", JCAP **1107** (2011) 025, arXiv:1105.2044.

[54] P. Andre *et al.*, "PRISM (Polarized Radiation Imaging and Spectroscopy Mission): A White Paper on the Ultimate Polarimetric Spectro-Imaging of the Microwave and Far-Infrared Sky", arXiv:1306.2259.

[55] P. Andr *et al.*, "PRISM (Polarized Radiation Imaging and Spectroscopy Mission): An Extended White Paper", JCAP **1402** (2014) 006, arXiv:1310.1554.

[56] A. A. Starobinsky and J. Yokoyama, "Equilibrium state of a selfinteracting scalar field in the De Sitter background", Phys.Rev. **D50** (1994) 6357, arXiv:astro-ph/9407016.

[57] R. Kallosh and A. D. Linde, "P term, D term and F term inflation", JCAP **0310** (2003) 008, arXiv:hep-th/0306058.

[58] B. Garbrecht, C. Pallis, and A. Pilaftsis, "Anatomy of F(D)-Term Hybrid Inflation", JHEP **0612** (2006) 038, arXiv:hep-ph/0605264.

[59] B. Clauwens and R. Jeannerot, "D-term inflation after spontaneous symmetry breaking", JCAP **0803** (2008) 016, arXiv:0709.2112.

[60] P. Binetruy, G. Dvali, R. Kallosh, and A. Van Proeyen, "Fayet-Iliopoulos terms in supergravity and cosmology", Class.Quant.Grav. **21** (2004) 3137, arXiv:hep-th/0402046.

[61] R. Jeannerot, "Inflation in supersymmetric unified theories", Phys.Rev. **D56** (1997) 6205, arXiv:hep-ph/9706391.

[62] R. Jeannerot, S. Khalil, G. Lazarides, and Q. Shafi, "Inflation and monopoles in supersymmetric SU(4)C x SU(2)(L) x SU(2)(R)", JHEP **0010** (2000) 012, arXiv:hep-ph/0002151.

[63] T. Fukuyama, N. Okada, and T. Osaka, "Realistic Hybrid Inflation in 5D Orbifold SO(10) GUT", JCAP **0809** (2008) 024, arXiv:0806.4626.

[64] R. A. Battye, B. Garbrecht, and A. Moss, "Constraints on Supersymmetric Models of Hybrid Inflation", JCAP **0609** (2006) 007, arXiv:astro-ph/0607339.

[65] R. Battye, B. Garbrecht, and A. Moss, "Tight constraints on F- and D-term hybrid inflation scenarios", Phys.Rev. **D81** (2010) 123512, arXiv:1001.0769.

[66] P. Ade *et al.*, "Planck 2013 results. XXV. Searches for cosmic strings and other topological defects", arXiv:1303.5085.

[67] L. Kofman, A. D. Linde, and A. A. Starobinsky, "Towards the theory of reheating after inflation", Phys.Rev. **D56** (1997) 3258, arXiv:hep-ph/9704452.

[68] J. Garcia-Bellido and A. D. Linde, "Preheating in hybrid inflation", Phys.Rev. **D57** (1998) 6075, arXiv:hep-ph/9711360.

[69] G. N. Felder, *et al.*, "Dynamics of symmetry breaking and tachyonic preheating", Phys.Rev.Lett. **87** (2001) 011601, arXiv:hep-ph/0012142.

[70] G. N. Felder, L. Kofman, and A. D. Linde, "Tachyonic instability and dynamics of spontaneous symmetry breaking", Phys.Rev. **D64** (2001) 123517, arXiv:hep-th/0106179.

[71] E. J. Copeland, S. Pascoli, and A. Rajantie, "Dynamics of tachyonic preheating after hybrid inflation", Phys.Rev. **D65** (2002) 103517, arXiv:hep-ph/0202031.

[72] V. N. Senoguz and Q. Shafi, "Reheat temperature in supersymmetric hybrid inflation models", Phys.Rev. **D71** (2005) 043514, arXiv:hep-ph/0412102.

[73] C. Gordon, D. Wands, B. A. Bassett, and R. Maartens, "Adiabatic and entropy perturbations from inflation", Phys.Rev. **D63** (2001) 023506, arXiv:astro-ph/0009131.

[74] D. H. Lyth and Y. Rodriguez, "The Inflationary prediction for primordial non-Gaussianity", Phys.Rev.Lett. **95** (2005) 121302, arXiv:astro-ph/0504045.

[75] E. Komatsu and D. N. Spergel, "Acoustic signatures in the primary microwave background bispectrum", Phys.Rev. **D63** (2001) 063002, arXiv:astro-ph/0005036.

[76] J. M. Maldacena, "Non-Gaussian features of primordial fluctuations in single field inflationary models", JHEP **0305** (2003) 013, arXiv:astro-ph/0210603.

[77] C. Ringeval, "The exact numerical treatment of inflationary models", Lect.Notes Phys. **738** (2008) 243, arXiv:astro-ph/0703486.

[78] P. Ade *et al.*, "Planck 2013 results. XV. CMB power spectra and likelihood", Astron.Astrophys. **571** (2014) A15, arXiv:1303.5075.

[79] S. Das, *et al.*, "The Atacama Cosmology Telescope: temperature and gravitational lensing power spectrum measurements from three seasons of data", JCAP **1404** (2014) 014, arXiv:1301.1037.

[80] K. Story, *et al.*, "A Measurement of the Cosmic Microwave Background Damping Tail from the 2500-square-degree SPT-SZ survey", Astrophys.J. **779** (2013) 86, arXiv:1210.7231.

[81] S. Furlanetto, *et al.*, "Cosmology from the Highly-Redshifted 21 cm Line", arXiv:0902.3259.

[82] J. R. Pritchard and A. Loeb, "Constraining the unexplored period between the dark ages and reionization with observations of the global 21 cm signal", Phys.Rev. **D82** (2010) 023006, arXiv:1005.4057.

[83] J. R. Pritchard and A. Loeb, "21-cm cosmology", Rept.Prog.Phys. **75** (2012) 086901, arXiv:1109.6012.

[84] S. Clesse, *et al.*, "Background reionization history from omniscopes", Phys.Rev. **D86** (2012) 123506, arXiv:1208.4277.

[85] J. Chluba and R. Sunyaev, "The evolution of CMB spectral distortions in the early Universe", Mon.Not.Roy.Astron.Soc. **419** (2012) 1294, arXiv:1109.6552.

[86] R. A. Sunyaev and R. Khatri, "Unavoidable CMB spectral features and blackbody photosphere of our Universe", Int.J.Mod.Phys. **D22** (2013) 1330014, arXiv:1302.6553.

[87] J. Chluba, "Distinguishing different scenarios of early energy release with spectral distortions of the cosmic microwave background", Mon.Not.Roy.Astron.Soc. **436** (2013) 2232, arXiv:1304.6121.

[88] R. Khatri and R. A. Sunyaev, "Beyond y and μ: the shape of the CMB spectral distortions in the intermediate epoch, $1.5 \times 10^4 < z < 2 \times 10^5$", JCAP **1209** (2012) 016, arXiv:1207.6654.

[89] R. Khatri and R. A. Sunyaev, "Forecasts for CMB μ and i-type spectral distortion constraints on the primordial power spectrum on scales $8 \lesssim k \lesssim 10^4 Mpc^{-1}$ with the future Pixie-like experiments", JCAP **1306** (2013) 026, arXiv:1303.7212.

[90] J. Chluba, A. L. Erickcek, and I. Ben-Dayan, "Probing the inflaton: Small-scale power spectrum constraints from measurements of the CMB energy spectrum", Astrophys.J. **758** (2012) 76, arXiv:1203.2681.

[91] J. Chluba and D. Grin, "CMB spectral distortions from small-scale isocurvature fluctuations", Mon.Not.Roy.Astron.Soc. **434** (2013) 1619, arXiv:1304.4596.

[92] R. Khatri, R. A. Sunyaev, and J. Chluba, "Mixing of blackbodies: entropy production and dissipation of sound waves in the early Universe", Astron.Astrophys. **543** (2012) A136, arXiv:1205.2871.

[93] J. Chluba, R. Khatri, and R. A. Sunyaev, "CMB at 2x2 order: The dissipation of primordial acoustic waves and the observable part of the associated energy release", Mon.Not.Roy.Astron.Soc. **425** (2012) 1129, arXiv:1202.0057.

[94] J. Chluba, "Green's function of the cosmological thermalization problem", Mon.Not.Roy.Astron.Soc. **434** (2013) 352, arXiv:1304.6120.

[95] Y. B. Zeldovich and R. A. Sunyaev, "The Interaction of Matter and Radiation in a Hot-Model Universe", Astrophys.Space Sci. **4** (1969) 301.

[96] J. Chluba and D. Jeong, "Teasing bits of information out of the CMB energy spectrum", arXiv:1306.5751.

[97] E. D. Stewart and D. H. Lyth, "A More accurate analytic calculation of the spectrum of cosmological perturbations produced during inflation", Phys.Lett. **B302** (1993) 171, arXiv:gr-qc/9302019.

[98] R. Allahverdi, K. Enqvist, J. Garcia-Bellido, and A. Mazumdar, "Gauge invariant MSSM inflaton", Phys.Rev.Lett. **97** (2006) 191304, arXiv:hep-ph/0605035.

[99] D. H. Lyth, "MSSM inflation", JCAP **0704** (2007) 006, arXiv:hep-ph/0605283.

[100] S. Hotchkiss, A. Mazumdar, and S. Nadathur, "Inflection point inflation: WMAP constraints and a solution to the fine-tuning problem", JCAP **1106** (2011) 002, arXiv:1101.6046.

[101] E. D. Stewart, "Flattening the inflaton's potential with quantum corrections", Phys.Lett. **B391** (1997) 34, arXiv:hep-ph/9606241.

[102] E. D. Stewart, "Flattening the inflaton's potential with quantum corrections. 2.", Phys.Rev. **D56** (1997) 2019, arXiv:hep-ph/9703232.

[103] L. Covi, D. H. Lyth, and L. Roszkowski, "Observational constraints on an inflation model with a running mass", Phys.Rev. **D60** (1999) 023509, arXiv:hep-ph/9809310.

[104] L. Covi and D. H. Lyth, "Running mass models of inflation, and their observational constraints", Phys.Rev. **D59** (1999) 063515, arXiv:hep-ph/9809562.

[105] L. Covi, D. H. Lyth, A. Melchiorri, and C. J. Odman, "The Running-mass inflation model and WMAP", Phys.Rev. **D70** (2004) 123521, arXiv:astro-ph/0408129.

[106] X. Chen and Y. Wang, "Quasi-Single Field Inflation and Non-Gaussianities", JCAP **1004** (2010) 027, arXiv:0911.3380.

[107] S. Pi and M. Sasaki, "Curvature Perturbation Spectrum in Two-field Inflation with a Turning Trajectory", JCAP **1210** (2012) 051, arXiv:1205.0161.

[108] X. Gao, D. Langlois, and S. Mizuno, "Oscillatory features in the curvature power spectrum after a sudden turn of the inflationary trajectory", JCAP **1310** (2013) 023, arXiv:1306.5680.

[109] T. Noumi and M. Yamaguchi, "Primordial spectra from sudden turning trajectory", JCAP **1312** (2013) 038, arXiv:1307.7110.

[110] S. Weinberg, "Quantum contributions to cosmological correlations", Phys.Rev. **D72** (2005) 043514, arXiv:hep-th/0506236.

[111] C. Cheung, *et al.*, "The Effective Field Theory of Inflation", JHEP **0803** (2008) 014, arXiv:0709.0293.

[112] A. Achucarro, *et al.*, "Mass hierarchies and non-decoupling in multi-scalar field dynamics", Phys.Rev. **D84** (2011) 043502, arXiv:1005.3848.

[113] A. Achucarro, *et al.*, "Heavy fields, reduced speeds of sound and decoupling during inflation", Phys.Rev. **D86** (2012) 121301, arXiv:1205.0710.

[114] X. Gao, D. Langlois, and S. Mizuno, "Influence of heavy modes on perturbations in multiple field inflation", JCAP **1210** (2012) 040, arXiv:1205.5275.

[115] M. Park and L. Sorbo, "Sudden variations in the speed of sound during inflation: features in the power spectrum and bispectrum", Phys.Rev. **D85** (2012) 083520, arXiv:1201.2903.

[116] D. H. Lyth, "Non-gaussianity and cosmic uncertainty in curvaton-type models", JCAP **0606** (2006) 015, arXiv:astro-ph/0602285.

[117] T. Bringmann, P. Scott, and Y. Akrami, "Improved constraints on the primordial power spectrum at small scales from ultracompact minihalos", Phys.Rev. **D85** (2012) 125027, arXiv:1110.2484.

[118] A. S. Josan, A. M. Green, and K. A. Malik, "Generalised constraints on the curvature perturbation from primordial black holes", Phys.Rev. **D79** (2009) 103520, arXiv:0903.3184.

[119] K. W. Masui and U.-L. Pen, "Primordial gravity wave fossils and their use in testing inflation", Phys.Rev.Lett. **105** (2010) 161302, arXiv:1006.4181.

[120] N. Tsamis and R. Woodard, "The Physical basis for infrared divergences in inflationary quantum gravity", Class.Quant.Grav. **11** (1994) 2969.

[121] B. Allen, "Vacuum States in de Sitter Space", Phys.Rev. **D32** (1985) 3136.

[122] B. Allen and A. Folacci, "The Massless Minimally Coupled Scalar Field in De Sitter Space", Phys.Rev. **D35** (1987) 3771.

[123] A. A. Starobinsky, "STOCHASTIC DE SITTER (INFLATIONARY) STAGE IN THE EARLY UNIVERSE", Lect.Notes Phys. **246** (1986) 107.

[124] A. A. Starobinsky and J. Yokoyama, "Equilibrium state of a selfinteracting scalar field in the De Sitter background", Phys.Rev. **D50** (1994) 6357, arXiv:astro-ph/9407016.

[125] A. Rajaraman, "On the proper treatment of massless fields in Euclidean de Sitter space", Phys.Rev. **D82** (2010) 123522, arXiv:1008.1271.

[126] M. Beneke and P. Moch, "On dynamical mass generation in Euclidean de Sitter space", Phys.Rev. **D87** (2013) 064018, arXiv:1212.3058.

[127] A. Higuchi, D. Marolf, and I. A. Morrison, "On the Equivalence between Euclidean and In-In Formalisms in de Sitter QFT", Phys.Rev. **D83** (2011) 084029, arXiv:1012.3415.

[128] S. Hollands, "Correlators, Feynman diagrams, and quantum no-hair in deSitter spacetime", Commun.Math.Phys. **319** (2013) 1, arXiv:1010.5367.

[129] D. Marolf and I. A. Morrison, "The IR stability of de Sitter QFT: results at all orders", Phys.Rev. **D84** (2011) 044040, arXiv:1010.5327.

[130] S. Hollands, "Massless interacting quantum fields in deSitter spacetime", Annales Henri Poincare **13** (2012) 1039, arXiv:1105.1996.

[131] J. S. Schwinger, "Brownian motion of a quantum oscillator", J.Math.Phys. **2** (1961) 407.

[132] L. Keldysh, "Diagram technique for nonequilibrium processes", Zh.Eksp.Teor.Fiz. **47** (1964) 1515.

[133] V. Onemli and R. Woodard, "Superacceleration from massless, minimally coupled phi**4", Class.Quant.Grav. **19** (2002) 4607, arXiv:gr-qc/0204065.

[134] V. Onemli and R. Woodard, "Quantum effects can render w < -1 on cosmological scales", Phys.Rev. **D70** (2004) 107301, arXiv:gr-qc/0406098.

[135] T. Brunier, V. Onemli, and R. Woodard, "Two loop scalar self-mass during inflation", Class.Quant.Grav. **22** (2005) 59, arXiv:gr-qc/0408080.

[136] E. Kahya and V. Onemli, "Quantum Stability of a w < -1 Phase of Cosmic Acceleration", Phys.Rev. **D76** (2007) 043512, arXiv:gr-qc/0612026.

[137] B. Garbrecht and G. Rigopoulos, "Self Regulation of Infrared Correlations for Massless Scalar Fields during Inflation", Phys.Rev. **D84** (2011) 063516, arXiv:1105.0418.

[138] F. Gautier and J. Serreau, "Infrared dynamics in de Sitter space from Schwinger-Dyson equations", Phys.Lett. **B727** (2013) 541, arXiv:1305.5705.

[139] T. Tanaka and Y. Urakawa, "Loops in inflationary correlation functions", Class.Quant.Grav. **30** (2013) 233001, arXiv:1306.4461.

[140] M. Herranen, T. Markkanen, and A. Tranberg, "Quantum corrections to scalar field dynamics in a slow-roll space-time", JHEP **1405** (2014) 026, arXiv:1311.5532.

[141] T. Arai, "Nonperturbative Infrared Effects for Light Scalar Fields in de Sitter Space", Class.Quant.Grav. **29** (2012) 215014, arXiv:1111.6754.

[142] T. Arai, "Renormalization of the 2PI Hartree-Fock approximation on de Sitter background in the broken phase", Phys.Rev. **D86** (2012) 104064, arXiv:1204.0476.

[143] D. L. Lopez Nacir, F. D. Mazzitelli, and L. G. Trombetta, "Hartree approximation in curved spacetimes revisited: The effective potential in de Sitter spacetime", Phys.Rev. **D89** (2014) 024006, arXiv:1309.0864.

[144] A. Riotto and M. S. Sloth, "On Resumming Inflationary Perturbations beyond One-loop", JCAP **0804** (2008) 030, arXiv:0801.1845.

[145] J. Serreau, "Effective potential for quantum scalar fields on a de Sitter geometry", Phys.Rev.Lett. **107** (2011) 191103, arXiv:1105.4539.

[146] T. Prokopec, "Symmetry breaking and the Goldstone theorem in de Sitter space", JCAP **1212** (2012) 023, arXiv:1110.3187.

[147] D. Boyanovsky, "Spontaneous symmetry breaking in inflationary cosmology: on the fate of Goldstone Bosons", Phys.Rev. **D86** (2012) 023509, arXiv:1205.3761.

[148] J. Serreau and R. Parentani, "Nonperturbative resummation of de Sitter infrared logarithms in the large-N limit", Phys.Rev. **D87** (2013) 085012, arXiv:1302.3262.

[149] D. Boyanovsky, "Condensates and quasiparticles in inflationary cosmology: mass generation and decay widths", Phys.Rev. **D85** (2012) 123525, arXiv:1203.3903.

[150] C. Burgess, L. Leblond, R. Holman, and S. Shandera, "Super-Hubble de Sitter Fluctuations and the Dynamical RG", JCAP **1003** (2010) 033, arXiv:0912.1608.

[151] A. Youssef and D. Kreimer, "Resummation of infrared logarithms in de Sitter space via Dyson-Schwinger equations: the ladder-rainbow approximation", Phys.Rev. **D89** (2014) 124021, arXiv:1301.3205.

[152] M. Spradlin, A. Strominger, and A. Volovich, "Les Houches lectures on de Sitter space", (2001) 423arXiv:hep-th/0110007.

[153] N. Tsamis and R. Woodard, "The Structure of perturbative quantum gravity on a De Sitter background", Commun.Math.Phys. **162** (1994) 217.

[154] A. H. Guth and S.-Y. Pi, "The Quantum Mechanics of the Scalar Field in the New Inflationary Universe", Phys.Rev. **D32** (1985) 1899.

[155] D. Campo and R. Parentani, "Space-time correlations in inflationary spectra: A Wave-packet analysis", Phys.Rev. **D70** (2004) 105020, arXiv:gr-qc/0312055.

[156] J. Martin and M. Musso, "Solving stochastic inflation for arbitrary potentials", Phys.Rev. **D73** (2006) 043516, arXiv:hep-th/0511214.

[157] T. Prokopec, N. Tsamis, and R. Woodard, "Stochastic Inflationary Scalar Electrodynamics", Annals Phys. **323** (2008) 1324, arXiv:0707.0847.

[158] K. Enqvist, D. G. Figueroa, and G. Rigopoulos, "Fluctuations along supersymmetric flat directions during Inflation", JCAP **1201** (2012) 053, arXiv:1109.3024.

[159] J. Martin and V. Vennin, "Stochastic Effects in Hybrid Inflation", Phys.Rev. **D85** (2012) 043525, arXiv:1110.2070.

[160] G. Rigopoulos, "Fluctuation-dissipation and equilibrium for scalar fields in de Sitter", arXiv:1305.0229.

[161] A. Vilenkin and L. Ford, "Gravitational Effects upon Cosmological Phase Transitions", Phys.Rev. **D26** (1982) 1231.

[162] A. D. Linde, "Scalar Field Fluctuations in Expanding Universe and the New Inflationary Universe Scenario", Phys.Lett. **B116** (1982) 335.

[163] A. Vilenkin, "Quantum Fluctuations in the New Inflationary Universe", Nucl.Phys. **B226** (1983) 527.

[164] R. Jordan, "Effective Field Equations for Expectation Values", Phys.Rev. **D33** (1986) 444.

[165] A. Kamenev and A. Levchenko, "Keldysh technique and nonlinear sigma-model: Basic principles and applications", arXiv:0901.3586.

[166] A. Altland and B. Simons, "Condensed matter field theory", Cambridge University Press .

[167] T. Prokopec, O. Tornkvist, and R. P. Woodard, "Photon mass from inflation", Phys.Rev.Lett. **89** (2002) 101301, arXiv:astro-ph/0205331.

[168] T. Prokopec and E. Puchwein, "Photon mass generation during inflation: de Sitter invariant case", JCAP **0404** (2004) 007, arXiv:astro-ph/0312274.

[169] D. Seery, "One-loop corrections to a scalar field during inflation", JCAP **0711** (2007) 025, arXiv:0707.3377.

[170] D. Seery, "One-loop corrections to the curvature perturbation from inflation", JCAP **0802** (2008) 006, arXiv:0707.3378.

[171] D. Seery, "Infrared effects in inflationary correlation functions", Class.Quant.Grav. **27** (2010) 124005, arXiv:1005.1649.

[172] G. Leung, E. R. Tarrant, C. T. Byrnes, and E. J. Copeland, "Reheating, Multi-field Inflation and the Fate of the Primordial Observables", JCAP **1209** (2012) 008, arXiv:1206.5196.

[173] L. Parker, "Amplitude of Perturbations from Inflation", arXiv:hep-th/0702216.

[174] R. Durrer, G. Marozzi, and M. Rinaldi, "On Adiabatic Renormalization of Inflationary Perturbations", Phys.Rev. **D80** (2009) 065024, arXiv:0906.4772.

[175] G. Marozzi, M. Rinaldi, and R. Durrer, "On infrared and ultraviolet divergences of cosmological perturbations", Phys.Rev. **D83** (2011) 105017, arXiv:1102.2206.

[176] I. Agullo, J. Navarro-Salas, G. J. Olmo, and L. Parker, "Remarks on the renormalization of primordial cosmological perturbations", Phys.Rev. **D84** (2011) 107304, arXiv:1108.0949.

Acknowledgments:

I would like to express my special appreciation and thanks to my advisor Prof. Dr. Björn Garbrecht for encouraging my research and for allowing me to grow as a research scientist. I would also like to thank Dr. Sébastien Clesse, Dr. Gerasimos Rigopoulos, and Dr. Florian Gautier for the great collaborating experiences during these past three years.

In addition, a thank you to Prof. Martin Beneke, and Prof. Yvonne Y. Y. Wong who teach me respectively the quantum field theory in curved space and cosmological perturbation theory, which are very useful for the researches in this thesis and in the future. I thank Dr. Stefan Recksiegel for support in all kinds of computer related issues.

Then, I would like to thank all the colleagues and friends of T31 and T70 groups, in particular, Dr. Marco Drewes and Dr. Yuming Wang, for their friendly help in all kind of issues.

I also like to express my gratitude towards the China Scholarship Council for their financial support.

Moreover, I am grateful to Prof. Ying Jiang, Prof. Shao-feng Wu, and Prof. Xian-hui Ge. Their advice and support on both research as well as on my career have been priceless.

Finally, A special thanks to my family. Words cannot express how grateful I am to my parents for their never-ending support during my studies.